POLITECNICO DI TORINO
Repository ISTITUZIONALE

Modeling and experimental characterization of belt drive systems in micro-hybrid vehicles

Original
Modeling and experimental characterization of belt drive systems in micro-hybrid vehicles / DI NAPOLI, Maria. - (2018 Oct 18). [10.6092/polito/porto/2715955]

Availability:
This version is available at: 11583/2715955 since: 2018-10-29T21:10:25Z

Publisher:
Politecnico di Torino

Published
DOI:10.6092/polito/porto/2715955

Terms of use:
Altro tipo di accesso

This article is made available under terms and conditions as specified in the corresponding bibliographic description in the repository

Publisher copyright

(Article begins on next page)

04 May 2023

ScuDo

Scuola di Dottorato ~ Doctoral School

WHAT YOU ARE, TAKES YOU FAR

Doctoral Dissertation

Doctoral Program in Mechanical Engineering (30^{th}cycle)

Modeling and Experimental Characterization of Belt Drive Systems in Micro-Hybrid Vehicles

By

Maria di Napoli

******

Supervisor(s):

Prof. A.Tonoli, Supervisor

Doctoral Examination Committee:

Prof. L. Goglio, PhD Course Coordinator, Politecnico di Torino

Prof. L. Manin, Referee, Institut National des Sciences Appliquées Lyon

Prof. R.G. Parker, Referee, Virginia Polytechnic Institute and State University

Prof. N. Amati, Politecnico di Torino

Prof. M. Avalle, University of Genova

Prof. S. Zucca, Politecnico di Torino

Politecnico di Torino

2018

Declaration

I hereby declare that, the contents and organization of this dissertation constitute my own original work and does not compromise in any way the rights of third parties, including those relating to the security of personal data.

Maria di Napoli
2018

* This dissertation is presented in partial fulfillment of the requirements for **Ph.D. degree** in the Graduate School of Politecnico di Torino (ScuDo).

To my parents,
to my sister Ester,
to my Love,
... and to my little me.
We did it.

A James e a Giacomo,
siete sempre con me.

À ma petite Siham,
mon grand orgueil.

Acknowledgements

At the end of this journey, it is compulsory for me to thank Professors Andrea Tonoli and Nicola Amati for their teaching and precious guidance. I also want to thank Professor Wen-bin Shangguan, from the South China University of Technology, who hosted me in Guangzhou together with his team and made me feel welcome as if I was not 5000km away from home.
My gratitude goes to Professors Lionel Manin and Robert Parker whose corrections and suggestions were an important contribution to my thesis and helped me to better present and give credit to my research activity.
A special and warm thought goes to my colleagues at the Mechatronics Laboratory of Politecnico di Torino who shared with me these years of work and learning, especially Renato, Sanjar, Lester and Fabrizio who were valuable guides both from a technical and a professional point of view.
Eventually, from the bottom of my heart I want to thank my fabulous family, my parents Dario and Margarita and my sister Ester. Their priceless support, advice and love accompanied me all the way through my work, my education and my life. It is impossible for me to think how and where I would be right now without you. You're my most valuable gift.

Abstract

Belt Drive Systems (BDS) constitute the traditional automotive mechanism used to power the main internal accessories (such as the alternator, water pump and air conditioning pump) taking power from the engine's crankshaft rotational motion. BDS usually work in the severe ambient conditions of the engine compartment and are subject to highly dynamic excitations coming from the crankshaft harmonics. The substitution of the traditional alternator with an electric machine, namely Belt Starter Generator (BSG), is the most promising micro-hybrid technology towards a quick and effective satisfaction of the current regulations of fuel consumption and pollutant emissions reduction. The use of a BSG leads to increased stresses in the already complex front end accessory drive. As a matter of fact, a BSG is an electrical machine able to work both as motor and as generator and defines two distinct functioning modes of the drive, namely motor and alternator modes. The relative alternation of tight and slack spans profoundly changes the functionality of the overall drive and affects its transmissions capability and efficiency, furthermore resulting in NVH (noise vibration harshness) effects that need to be carefully addressed. Traditional automatic tensioners acting on the slack span of the alternator mode application are not capable of facing the irregular stresses of a BSG-based BDS which requires the use of a tensioning device capable of keeping the belt tension inside a safe range and of preventing slippage during all the operating conditions of the drive. With this goal many solutions are currently being investigated, such as the cooperation of two tensioners one for each span, active tensioners, double arm tensioners or hydraulic tensioners. The critical issues due to the involvement of BSG in BDS require a deep study focused on the tension conditions of the belt and its influence on the overall efficiency of the system.

The aim of the research described in this thesis is to obtain a defined modelling approach of belt drive systems for micro-hybrid vehicles and to validate it through extensive experimental analysis.

To obtain a reliable testing environment, a dedicated full-electric test rig was designed and realized. The test rig presented in this work is capable of assuring the repeatability and accuracy of the measurements leaving aside the uncertainties deriving from the irregularities of the ICE behaviour that usually affect the experimental activities conducted on front engine accessory drives.
After providing both the modelling and testing environment as assets for the analysis, several experimental activities are carried out with the goal of assessing the dynamic behaviour of belt drive systems and their efficiency, comparing the performances of different tensioning solutions, understanding the behaviour in static and dynamic conditions of a traditional automatic tensioner and one example of an omega twin arm tensioner, which is the tensioning solution most explored by the manufacturers at present.
The ultimate goal of gaining a complete understanding of belt drive systems in the special case of micro-hybrid vehicles is eventually fulfilled by an experimental validation of the static and dynamic models proposed.

Contents

List of Figures

List of Tables

Nomenclature

Roman Symbols

b	belt width
C	Torque
c	belt extension modulus or longitudinal stiffness, tension per unit strain
D	pulley diameter
d	damping
EI	belt bending stiffness
F	Force
G	belt carcass shear modulus
H	rubber layer thickness
h	belt thickness
J	inertia
K	tensioner spring stiffness
k	belt radial stiffness
L	total belt length
l	belt span length
L_i	tensioner arm length

M	Bending Moment
m	mass
P	Power
p	pressure
Q	Experimentally determined constant
R	radius
S	belt section area
s	belt slip
T	belt tension
t	time
v	longitudinal speed
W	energy loss per unit length
w	belt wedge-in or wedge-out of pulleys
x	belt compression

Greek Symbols

α	wrap angle of the belt around a pulley
β	wedge angle of the belt or the pulley
χ	fictitious
Δ	variation - gradient
δ	differential symbol
ε	strain
η	transmission efficiency
γ	shear deformation

γ_i force angle

ι angular displacement of the tensioner spring

κ belt torque factor as defined by [5]

λ coefficient of traction

μ friction coefficient

ν pulley rib angle

ω angular speed

ϕ sliding (ϕ_s) or adhesion (ϕ_a) arc symbol

π greek pi, constant

Ψ belt dissipation coefficient

ρ radius of curvature

ρ_{lt} mass per unit length of the belt

σ belt shear stresses

τ transmission ratio between the driving pulley and the driven pulleys

θ angular displacement

ξ belt damping factor

ζ belt coefficient of recovery

Subscripts

$i = 1, 2...n$ general subscript to indicate a pulley or a belt span in an n-pulleys belt drive system. The elements of the transmission are numbered according to the belt drive systems convention

0 Indicates the initial condition of the system

a adhesion arc

b belt

be	bending effects
c	centrifugal effects
com	(belt)compression or compliance
cr	creep
dr	generic driving pulley
dv	generic driven pulley
f	flank
h	(belt) hysteresis
k	dynamic friction coefficient
lt	(belt) loading
p	pulley
r	radius
S	slack span
s	sliding arc
st	static friction coefficient
T	tight span
t	belt tensioner
tr	transmittable (torque)
w	wedge-in and wedge-out of pulleys
z	z-axis

Chapter 1

Introduction

1.1 Motivation

The automotive industry is nowadays facing increasingly strict demands for fuel consumption and pollutant emissions reduction. Recently, European Union (EU) regulations have set penalties for car manufacturers of 95 euros per each gCO_2/km exceeding the emission limits for each sold vehicle that will start from 2019. As a result, the attention on electric and hybrid solutions for passenger and commercial cars has constantly grown over the years and traction and accessories electrification is a research topic widely discussed in recent literature.
The electrification of the powertrain – namely hybridization – is considered the most viable solution to quickly achieve the challenging emission targets within the shortest possible time. The latest trend is the development of micro-hybrid technologies that support the Internal Combustion Engine (ICE) in different operating conditions [1]. A micro-hybrid is a system where an electric machine able to work both as generator and motor is used to perform functions such as automatic ICE stop-start, launch assist, regenerative braking, and other features [2]. Two fundamental concepts for a combined starter-generator machine have been developed [3]: the Integrated Starter Generator (ISG) that is placed directly onto the crankshaft between the engine and the clutch and which replaces the flywheel, and the Belt Driven Starter Generator (BDSG or BSG) that replaces the alternator in the conventional Front End Accessory Drive (FEAD). While the ISG solution requires a completely revised housing, the BSG replaces the conventional alternator with a low impact

on the engine compartment layout, [1]. Despite such low impact, the installation of a BSG in a FEAD has its own drawbacks due to the complexity of the system where it is inserted. In traditional engine setups the FEADs are Belt Drive Systems (BDS) in charge of power transmission from the crankshaft to the accessories. They are complex and critical dynamic mechanisms, involving contact mechanics and vibration phenomena. FEAD are subject to highly dynamic excitations coming from the crankshaft irregularities. This harmonic excitation together with the inertia of the accessories (mainly the alternator in traditional configurations) and high loading conditions of the BDS, leads to vibrations of the belt and high tension fluctuations that can cause slippage and noise. Speed and torque losses inevitably hamper the performance of a belt drive system. They affect the transmission efficiency and induce vibrations and noise. Several dedicated components have been designed by manufacturers to overcome vibration and noise issues in automotive FEAD. Belts, crankshaft ([4, 5]) and alternator ([6, 7]) pulleys and belt tensioners have faced progressive modifications over the years in order to optimize the different components that define the rotational and longitudinal motions taking place in the front end accessory drive. Belt tensioners are used to minimize power losses while controlling the belt tension.
The critical issues due to the involvement of BSG in BDS and the need for identifying the best operating strategy require a deep study focused on the tension conditions of the belt and its influence on the overall efficiency and on the dynamic behaviour of the system.

1.2 Aim of the Work

The aim of the research described in this thesis is to obtain a defined modelling approach of belt drive systems for micro-hybrid vehicles and to validate it through extensive experimental analysis.
To obtain a reliable testing environment, a dedicated full-electric test rig was designed and realized. The test rig presented in this work is capable of assuring the repeatability and accuracy of the measurements leaving aside the uncertainties deriving from the irregularities of the ICE behaviour that usually affect the experimental activities conducted on front engine accessory drives.
After providing both the modelling and testing environment as assets for the analysis,

several experimental activities are carried out with the goal of assessing the dynamic behaviour of belt drive systems and their efficiency, comparing the performances of different tensioning solutions, understanding the behaviour in static and dynamic conditions of a traditional automatic tensioner and one example of an omega twin arm tensioner, which is the tensioning solution most explored by the manufacturers at present.
The ultimate goal of gaining a complete understanding of belt drive systems in the special case of micro-hybrid vehicles is eventually fulfilled by an experimental validation of the static and dynamic models proposed.

1.3 Thesis Outline

This thesis is divided into eight chapters:

- **Chapter 1** briefly motivates and delimits the present work. It eventually provides an outline of the thesis.
- **Chapter 2** is an overview on the functionalities of belt drive systems for micro-hybrid vehicles based both on literature and patents review. An insight on the different tensioning solutions for BSG-based BDS is given.
- **Chapter 3** and **Chapter 4** provide the state of the art about the power losses and the dynamic analysis of belt drive systems. An effort is done in highlighting the concepts needed for the case of engine front end accessory drives.
- **Chapter 5** contains the modelling activity that the author carried out, related to power losses, static and dynamic behaviour of BDS layouts.
- **Chapter 6** is focused on the test rig used for the experimental activities.
- **Chapter 7** describes the experimental results obtained and the consequent modelling validation.
- **Chapter 8** discusses the obtained results, states the conclusions and indicates possible future developments.

Chapter 2

Belt Drive Systems for Micro-Hybrids

When substituting the alternator with a Belt Starter Generator (BSG) the FEAD will be characterized by two different operating modes: generator mode or motor mode. The *generator mode* is used to replicate the function of a traditional alternator that collects the power from the belt to charge the vehicle battery. Furthermore, it enables the regenerative braking function. The *motor mode* is exploited during the electric boost, where the BSG assists the ICE for fast accelerations. Moreover, this mode is also used for the start and stop function, through which the cranking of the ICE is performed eliminating the need for a separate starter electric machine.

In Fig. 2.1, a BSG-equipped BDS is shown. It highlights the two belt spans that experience the alternation of tension when changing the operating condition of the BSG, which can provide positive or negative torque to the system. For positive torques the system is in motor mode and the tight span is the one highlighted in blue in Fig. 2.1; while for negative torques the tight span is the one in red and corresponds to the generator mode. The irregular stresses acting on the belt require the use of a tensioner whose features are extended to the operating conditions inherent to the use of a belt starter generator (BSG) instead of the traditional alternator. Each span needs to use a custom tensioning mechanism, indicated in Fig. 2.1 as the pulleys AT1 and AT2. Several belt tensioner solutions have been proposed by the manufacturers to overcome BSG-equipped BDS critical issues.

In this chapter an overview about the tensioning solutions for BSG-based BDS is provided. A general classification is built based on the characteristics of the belt

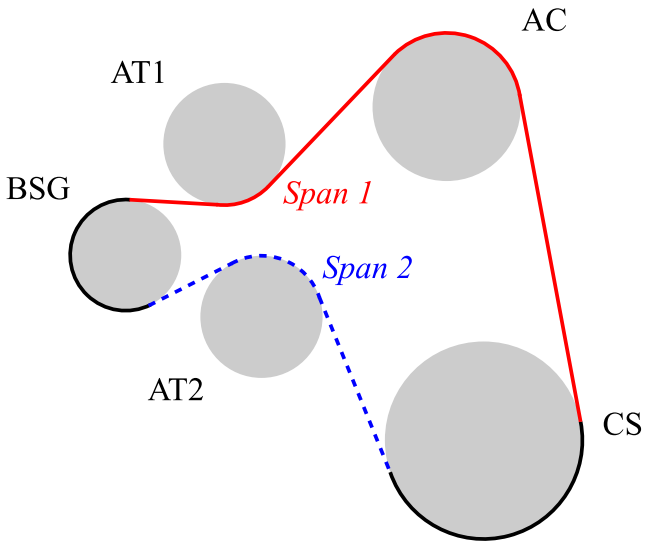

Fig. 2.1 BDS layout mounting a BSG. The two belt spans are alternately tight and slack according to the operating mode of the BSG and need the intervention of a dedicated tensioner to maintain the belt tension inside a reasonable operating range.

tensioners proposed by the main manufacturers. In the last section a particular focus is given to the twin-arm tensioners category. Despite its popularity, the twin-arm tensioner has been addressed almost exclusively by patents. The number of research papers on this topic is still exiguous. The very few available research works regarding this device cover exclusively design and numerical simulation aspects, [8], [9] and no experimental results can be found assessing the performances of belt tensioners designed to operate in a BSG-equipped BDS. The excursus on twin-arm tensioners provided in this section serves as background motivating the attention given to this type of belt tensioners in the present work.

2.1 Belt Tensioners

To control the tension in all the operating conditions of a BDS mounting a BSG a traditional automatic tensioner is not sufficient. Many different solutions have been adopted by different producers including passive and active solutions, one and two pulley tensioners, linear and rotative tensioners. According to their characteristics it is possible to provide a classification of the existing tensioning solutions for BDS mounting a BSG. A scheme of the classification described below is shown in Fig. 2.2.

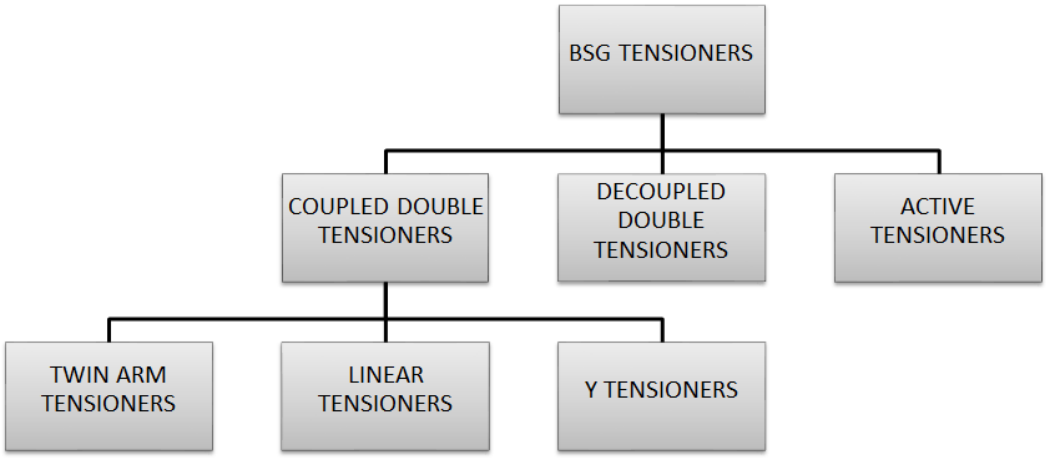

Fig. 2.2 Classification of tensioning solutions for BSG Systems

The first classification can be done between active tensioners and passive double tensioners. Active tensioners consist of one single pulley tensioner whose position is changed by means of an actuation to adapt to the operating condition of the belt drive system. An example of this solution is given by Dayco Europe S.r.l., in [10]. The passive double tensioners are characterized by two tensioner pulleys whose operation can be independent or linked one to the other. An example of decoupled double tensioners is given by the PSA Peugeot Citroen tensioning solution in [11]. The coupling between the two tensioner pulleys can be realized following different geometric patterns. The existing solutions allows to identify linear tensioners, Y or V tensioners and rotary twin arm tensioners. An example of linear tensioner is given by The Gates Corporation in [12]. The Gates Corporation provides also a Y tensioner, presented in [13]. The (rotary) twin arm tensioner topology is the most used and investigated by important BDS component manufacturers, such as Dayco Europe S.r.l. [14], General Motors Corporation [15], The Gates Corporation [16], Litens Automotive Partnership [17, 18], Mubea Muhr und Bender KG [19, 20] and Schaeffler Technologies [21].

The Dayco Europe S.r.l. active tensioner is indicated with (a) in Fig.2.3. It is characterized by a rotary electric motor which moves the arm tensioner by means of a planetary gear. Both the rotary motor and the planetary gear are protected inside the tensioner body with a compact configuration. The tensioner is meant to be mounted on the slack span of a BDS in BSG alternator mode. The position of the tensioner pulley is controlled by an electronic control unit at motor mode actuation. The

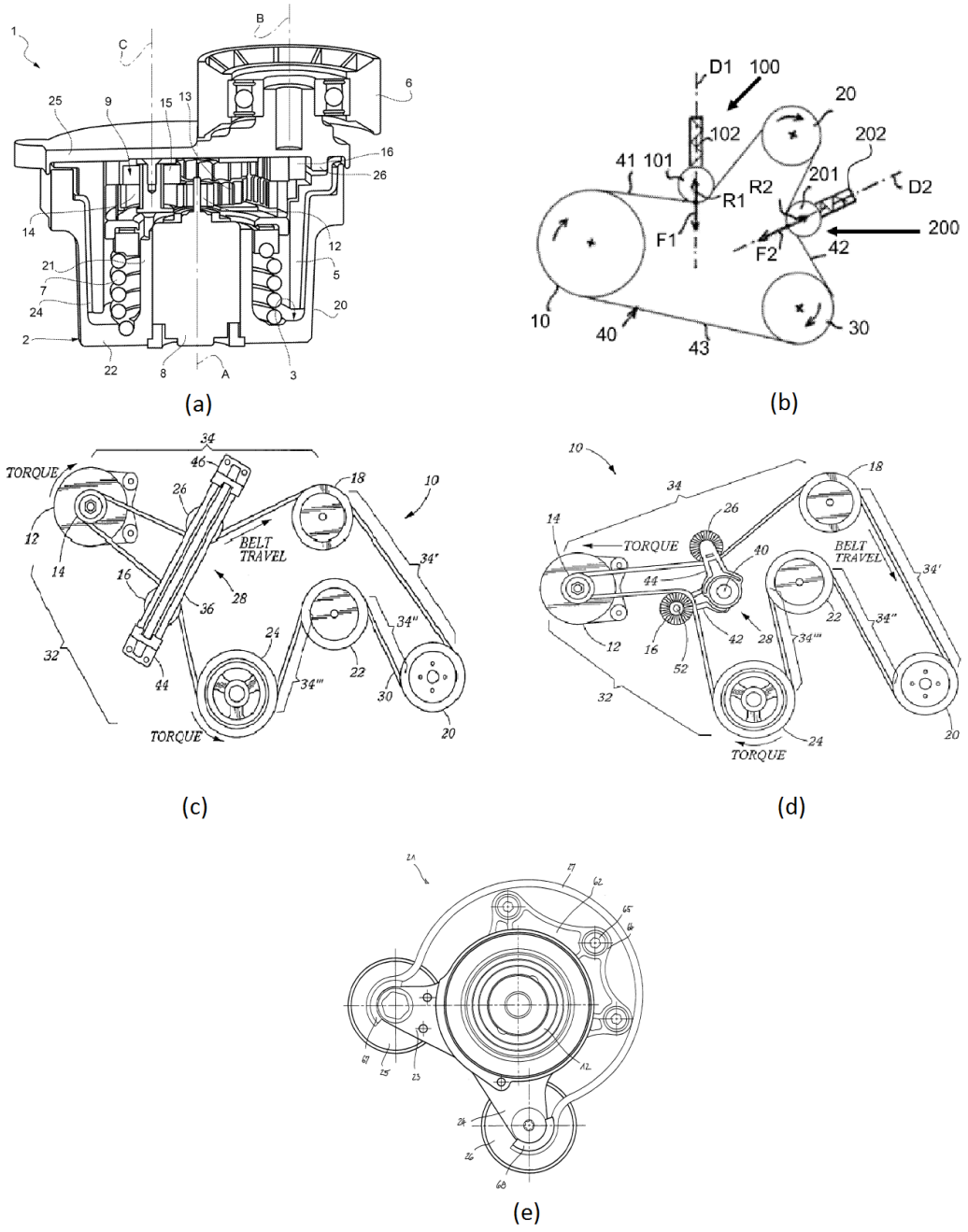

Fig. 2.3 Different tensioning solutions for BSG Systems: (a) Active Tensioner by Dayco Europe S.r.l., image taken from [10]; (b) Double Tensioner by PSA Peugeot Citroen, [11]; (c) Linear Tensioner by The Gates Corporation, [12]; (d) Y Tensioner by The Gates Corporation; (e) Rotative twin arm tensioner by Mubea Muhr und Bender KG[19].

presence of an electronic interface for the actuation represents the main drawback of active tensioners.
The PSA Peugeot Citroen decoupled double tensioner is indicated with (b) in Fig.2.3. Two independent automatic tensioners operate on the two belt spans adjacent to the BSG and alternating being slack and tight. The advantage of using two independent belt tensioner that are not mechanically connected one to the other is the possibility of designing their characteristics independently. Position, spring preload, damping, action angle can be chosen for each tensioner to optimize its functioning.
The Gates Corporation linear tensioner is indicated with (c) in Fig.2.3. It is a linear movement tensioner with a mechanical damping mechanism with asymmetrical damping properties. The two pulleys are rotably mounted on two separate carriers which have a sliding relation with a common track with two degrees freedom of movement.
The Gates Corporation Y tensioner is indicated with (d) in Fig.2.3. The device features two tensioner pulleys attached to two tensioner arms rotating around a common pivot. The movements of the two tensioner arms are asymmetrically biased by means of a resilient member, i.e. a steel torsion spring, which is indirectly connected to the first tensioner arm, via an interposed damper shoe, and directly to the second tensioner arm.
In Fig.2.3 an example of rotary tensioner is provided by means of the Mubea Muhr und Bender KG twin arm tensioner. This type of tensioning solution is further discussed in the following section.

2.1.1 Coupled Tensioners Functionality

In order to compare the different tensioners' geometries and their functionality it is useful to consider a simple figure of merit, namely the differential angle. The differential angle Φ_δ is the angle between the tensioner pulley's hubload, derived by the tension exerted by the belt on the pulley contact angle, and the tensioner arm direction. The differential angle is shown in Fig.2.4.
As described in [7], the differential angle shall be comprised in an interval $0 < \Phi_\delta < \pi$ to allow a correct functioning of the tensioner and it should be lower then $\frac{\pi}{2}$ for an optimal functioning. Referring to Fig. 2.3, in the cases (a) and (b), where the tensioners act in an independent and decoupled manner, the tensioners can be placed in the drive in order to obtain the most favourable differential angle. In the case of

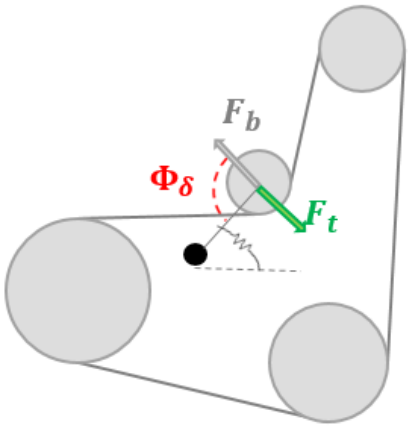

Fig. 2.4 The differential angle Φ_δ is defined as the angle between the tensioner pulley's hubload, derived by the tension exerted by the belt on the pulley contact angle, and the tensioner arm direction. F_b is the hubload exerted by the belt on the tensioner pulley axis; F_t is the tensioner force, perpendicular to the tensioner arm.

the coupled double tensioners, the two tensioner arms' movements are constrained to follow a certain defined path. The hubloads on the two tensioner pulleys always lie on the bisector of the pulleys' wrap angles, while the tensioner arms directions will be determined by the tensioner's displacement. The resulting differential angles on the two tensioner arms will result therefore to be beneficial or not to the drive behaviour for both BSG alternator and motor modes.

In the case of a linear tensioner, as shown in case (1) of Fig. 2.5, the tensioner arm and its action are always oriented longitudinally on the line joining the two tensioner pulleys. This leads to a situation where most of the time hubload and tensioner arm axis lie on the same direction having a differential angle close to π.

Likewise, in the case of a V-tensioner, as shown in case (2) of Fig. 2.5, the possibility of reaching a situation where $\Phi_\delta = \pi$ is very high. The movement around the common pivot placed in the inner part of the drive leads the two tensioner arms to be aligned with the pulley hubload in an alternate matter, whether the BSG is operating in alternator or motor mode.

Ultimately, in the case of a rotary twin arm tensioner, as shown in case (3) of Fig. 2.5, the tensioner arms movements keep the differential angle always lower then π and around $\frac{\pi}{2}$, that's to say the optimal position. This characteristic motivates the wide diffusion among manufacturers of the rotary tensioning solution for BSG-based BDS together with its constructive simplicity and passive feature.

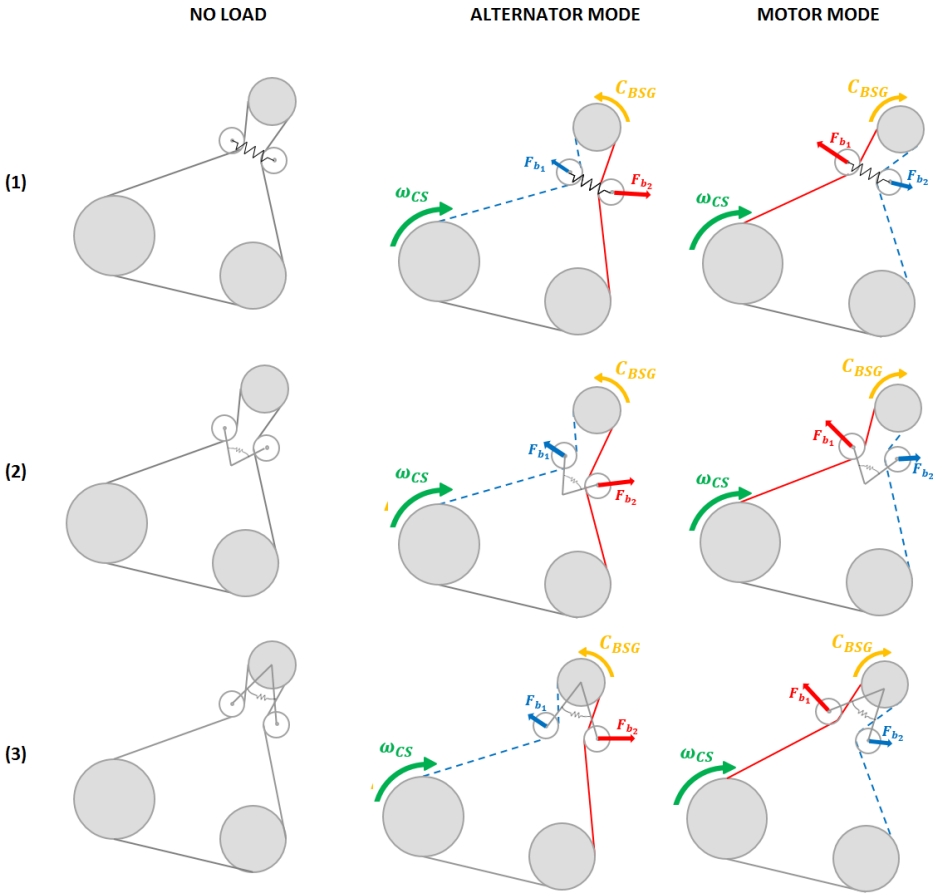

Fig. 2.5 Comparison of the different coupled double tensioners in BSG alternator and motor modes: (1) linear tensioner, (2) V-tensioner, (3) rotary twin arm tensioner. The belt slack span is indicated with a blue dashed line; the belt tight span is indicated with a red continuous line. ω_{CS} is the rotary speed imposed to the system by the crankshaft CS; C_{BSG} is the torque load of the BSG in a counter-clockwise direction in alternator mode and clockwise direction in motor mode; F_{b_1} and F_{b_1} are the hubloads exerted by the belt on the left and right tensioner pulleys, respectively.

2.1.2 Rotary Twin Arm Tensioners

In the following a major focus is addressed to the different rotary tensioning solutions that were proposed by the different manufacturers and which represent the strongest trend in the field of BSG-based BDS. In Fig.2.6 different rotary tensioner can be compared. Two main groups of rotary tensioners can be identified, referred to as omega or alpha tensioners depending on the relative positioning of the two tensioner pulleys around the BSG pulley and on the position of their rotational pivot that can be identified in a common axis or not. In both cases a common angular motion around a central axis characterizes the rotary tensioners, which can be coincident to the BSG pulley or not and can be the only movement of the tensioner or be accompanied by an additional rotative motion for one of the two tensioner pulleys involved. The rotary twin arm tensioners are classified in 4 groups based on the functional scheme that can be used to describe their functioning. On each row of Fig. 2.6 a simple sketch of the corresponding kinematic layout is shown. The rotary pivots are highlighted with a red dot.

Image (a) in Fig. 2.6 represents a two arm tensioner solution proposed by Dayco Europe S.r.l. with a patent of 2004 [14]. The main goal of the presented design was to have a compact, reliable and efficient solution. Referring to image (a) of 2.6 the belt tensioner is characterised by a fixed tubular supporting portion where two arms are fitted to rotate about a common hinge axis. An elastic device for forcing the arms towards each other having a torsionally elastic elongated member extends through the tubular supporting portion, coaxially with the hinge axis and has the respective opposite end portions projecting outwards of the tubular supporting portion with respective end caps. One of the two end portions is fitted directly with one of the arms, and houses one end, connected integrally to the other cap, of the other arm as described in [14]. This tensioner is characterized by two arms with a common pivot, so it is part of the omega tensioners category.

The design presented in image (b) of Fig. 2.6 represents a tensioner by General Motors Corporation, dated back to 1988 [15]. It is characterised by a tensioner embodiment incorporated in the BSG housing, referred to as "stargen". The stargen is mounted to the vehicle in such a way that the housing can pivot about the shaft axis and roll inside a short arc defined between generating and cranking mode limit positions, defined by stop pins. The two tensioner arms hinged on the housing are then alternatively engaged or disabled to operate as a belt tensioner or a fixed idler

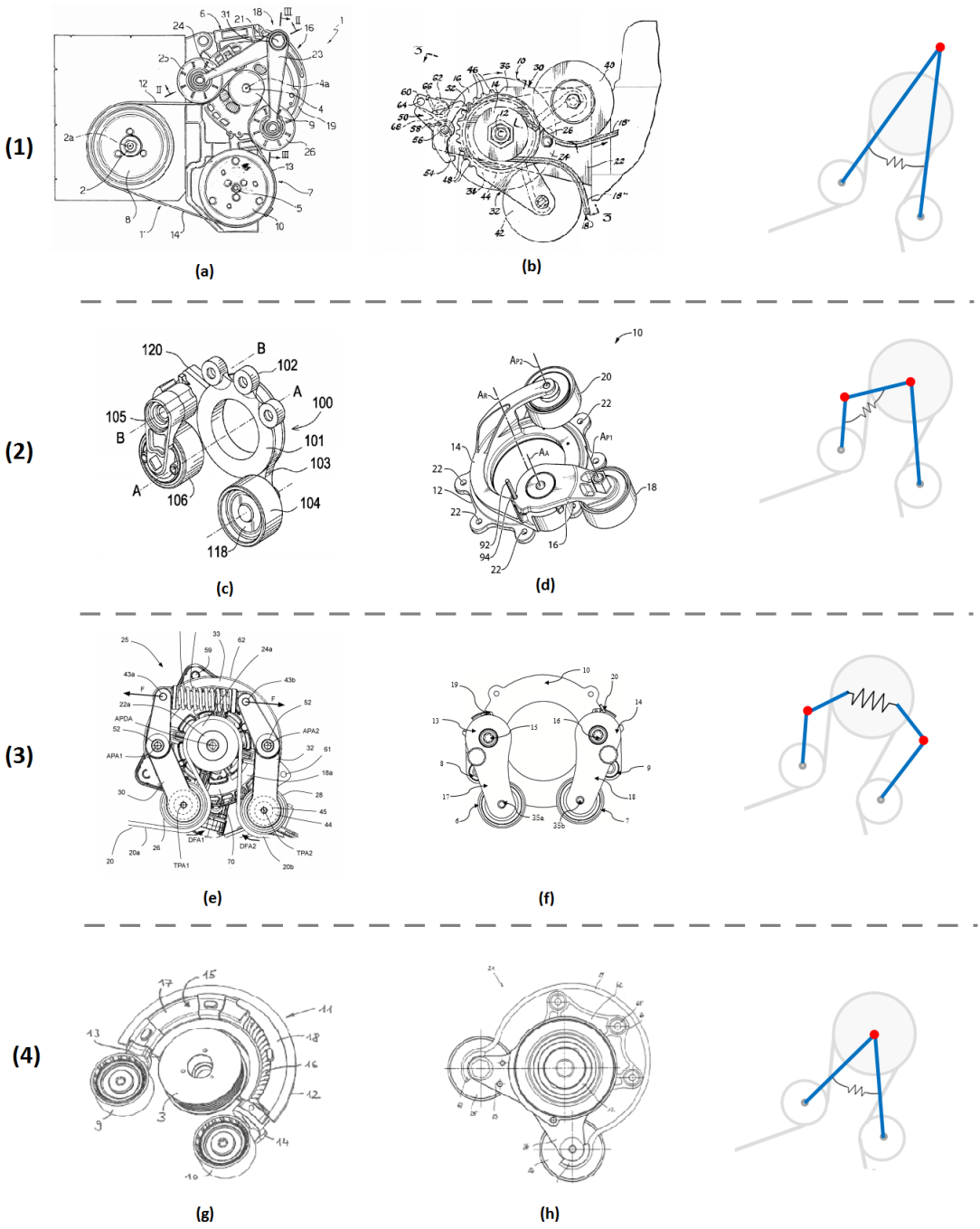

Fig. 2.6 Twin arm tensioners of different manufacturers: (a) Dayco Europe S.r.l [14]; (b) General Motors Corporation [15]; (c) The Gates Corporation [16]; (d) Litens Automotive Partnership [17]; (e) Litens Automotive Partnership [18]; (f) Ningbo Fengmao Far-East Rubber Co.,Ltd; (g) Schaeffler Technologies [21]; (h) Mubea Muhr und Bender KG [19, 20]. The corresponding tensioner functional schemes are drawn per each row (1-4).

pulley accordingly to the present operating condition. A tension spring hooked between the two tensioner arms continually swings them toward one another about the stargen shaft axis, [15]. This is again an omega type tensioner.
Cases (a) and (b) of Fig. 2.6 can be described by the functional scheme number (1) where a unique pivot (in red) is placed over the BSG axis and outside the drive. The two lever arms rotate around such pivot and are constrained by the action of a spring that connects them.
The invention in (c) of Fig. 2.6 was proposed by The Gates Corporation in 2015, [16]. It consists of an orbital tensioner, having a carrier engaged with a base and revolvable about a first axis, a pivot arm mounted to the carrier, the pivot arm pivotable about a second axis and the second axis orbitally movable about the first axis. The tensioner comprises a spring engaged between the carrier and the pivot arm, and a damping mechanism frictionally engaged between the carrier and the base to damp a carrier movement, [16]. This solution represents an alpha tensioner, due to the position of the second axis that constitutes the pivot of the second tensioner arm.
The goal of the invention of the Litens Automotive Partnership drawn in (d) of Fig. 2.6 is to have a belt tensioner that allows to have low belt tensions and hub loads on the pulleys of the system, without causing a negative impact on the fuel economy and component life ([17]). The proposed solution is a tensioner that includes a ring rotatably supported by a base mounted on a motive device, such as a belt alternator starter (BAS or BSG). The ring is rotatable around its axis and supports a tensioner pulley, biased towards one span of the belt drive system, and a tensioner arm which is pivotally mounted on the ring itself and supports a second tensioner pulley, which is biased towards a second belt span. Seemingly to the Gates Corporation tensioner described above, this tensioner is an alpha tensioner where a common rotative motion characterises the two pulley, one of which has an additional angular movement around another pivot.
The functional scheme number (2) of Fig. 2.6 describes cases (c) and (d). A common rotative motion characterizes both the tensioner arms. This motion is not dominated by the action of a spring but it is influenced only by the action of a friction torque, applied by a plastic or metallic bushing, or a cone spring. The top of one of the two tensioner arms accommodates a pulley and the other one serves as pivot for an additional arm that moves around such axis governed by the action of a spring.
The two inventions in (e) and (f) of Fig. 2.6 can be indicated as decoupled rotary tensioners. This definition implies that the angular movement of the two tensioner

pulleys is somehow decoupled between the two. An additional degree of freedom is provided to the pulleys that react to the changes of the operating conditions of the system independently one to the other. The corresponding functional scheme is shown in (3). Two tensioner arms rotate around two separated pivots according to belt tension states and according to the action of a spring connecting the two arms.
Invention (e) of Fig. 2.6 was proposed by the Litens Automotive Partnership in [18]. The proposed tensioner includes a base that is mountable to a frame of a BSG, two tensioner arms and an arm biasing member. Both the tensioner arms are allowed to move along two selected paths over a range of tension from 100N to a high tension equal to the yield strength of the belt. The positions of the two tensioner arms and the allowed paths are designed so that for any tensions combination in any operating condition the two tensioner pulleys remain sufficiently spaced apart from one another.
In image (f) of Fig. 2.6 the design proposed by Ningbo Fengmao Far-East Rubber Co. Ltd is shown. The tensioning device proposed comprises two tensioner arms mounted on a common ring. Both the tensioner arms have a stopper that defines the maximum displacement allowed. When in contact with the stopper, the tensioner pulley acts as a fix robust idler which is able to manage the tight span of the transmission facing high tension loads.
The main goal of the tensioner proposed in image (g) of Fig. 2.6 by Schaeffler Technologies was to have a reduced component complexity. For this reason the solution eliminates the need for a fastening of the housing which is mounted on the drive shaft by means of a roller bearing which ensures a durable and low-friction mounting of the tensioning device while providing a low damping during the oscillating pivot motion of the tensioner housing. This characteristic allows the tensioner to be not only suitable for the tensioning of traction mechanism drives with quasi-statically alternating tight and slack spans, but also to serve for a dynamic decoupling of the generator from the rotational irregularities of the internal combustion engine. The tensioner comprises two tensioner arms with two tensioner pulleys and a spring means that generates the tensioning force between the two tensioner arms.
Image (h) of Fig. 2.6 shows a tensioning solution proposed by Mubea Muhr und Bender KG in [19, 20]. The objective of the invention is to provide a tensioner which has a simple design, with a short overall length, resulting in a compact device that is easy to mount and to remove from the belt transmission. The tensioner comprises a housing with two tensioning arms which are pivotable around a common axis and

supported relative to one another by means of a spring. The housing is contact-free relative to the driving machine, the BSG, in an annular region surrounding the drive-shaft of the driving belt pulley.The operations of mounting and removing the belt tensioning device can take place independently of the mounting of the remaining parts of the belt drive. The pivot axis of the tensioning arms is arranged inside the outer diameter of the driving belt pulley and can be more particularly arranged coaxially relative to the driving axis of the BSG pulley.
The kinematics of cases (g) and (h) is depicted in row (4) of Fig. 2.6. It will be object of study of the next chapters of this thesis and it will be analysed in detail both from a functional and a performances point of view.

2.2 Chapter Conclusions and Remarks

The critical issues of BSG-based BDS were addressed in this chapter. The importance of this topic was highlighted through an excursus on the technological solutions provided so far by the main manufacturers of BDS components. The twin-arm tensioner strategy resulted to be the most interesting and investigated. It was possible to retrieve many informations from patents but the literature review on the topic resulted poor and incomplete. This finding motivates the interest that was put in the investigation and characterization of these devices and systems in the studies described in this thesis.

Chapter 3

State of the Art: Efficiency of Belt Drive Systems

The motion of a belt around the n-pulleys of a serpentine belt drive system is composed by periodical engaging, wrapping, stretching, slipping and disengaging instants. The characteristics of the belt motion affect the efficiency of the power transmission in terms of speed and torque losses depending onto the geometric and material characteristics of the transmission system. The belt can be a flat belt, a V- or V-ribbed belt, and it can change in length, width, thickness and material, having different damping and stiffness coefficients. The pulleys can have different radii, they can be grooved or not, and being characterized by different wedge or groove angles. The overall belt drive system can be composed of an arbitrary number of pulleys, placed at variable distances one from the other, obtaining different free span lengths and wrap angles onto the pulleys.

Over the last 50 years a lot was done by researchers to provide analytical formulations of the numerous loss mechanisms affecting belt drive systems and to define geometrical specifications for optimal power transmission and losses minimization. The focus of this chapter is the identification of the theoretical concepts needed for a complete understanding of the system object of study. The following paragraphs will deal with the classification of power losses occurring in belt drive systems, the application of analytical formulations to the case of V-ribbed belts and to serpentine power transmissions composed by n-pulleys.

A particular effort is addressed to the development of a uniform formulation of power losses due to the pulley-belt contact mechanics, that aims at summarizing the

different concepts arisen from a deep literature research activity. Additionally the general overview on the losses contributions that affect all kinds of belts (flat, V- and V-ribbed belts) highlights the influence of each loss phenomenon on the particular case of V-ribbed belts which are the ones used for automotive applications.

3.1 Power Losses Classification

There are many approaches that the authors have adopted in the attempt of proposing a clear and complete classification of the loss mechanisms affecting belt drive systems. However, decoupling the different phenomena can lead to inadequate and misleading concepts due to the deep relationship present among the several loss triggers and the related outcomes. It is therefore important to have an overall sight of the system and its phenomenology.
In a mechanical system the power (P) is defined as the product of torque (C) and rotational speed (ω) for rotational mechanics or force (F) and longitudinal speed (v) for linear mechanics. In the case of the dynamics that describe the motion of a BDS the following equation is to be considered:

$$P = C\omega \tag{3.1}$$

Through a simple manipulation of eq. (3.1), by differentiating and then dividing by the power, it is possible to show how the variation of power of the system is given by the summation of torque and speed variations:

$$\frac{dP}{P} = \frac{dC}{C} + \frac{d\omega}{\omega} \tag{3.2}$$

For a belt drive system, where the input and output powers are related to a driver pulley (dr) and driven pulley (dv), respectively, which are characterised by a transmission ratio τ, there holds:

$$\begin{aligned} \frac{dC}{C} &= \frac{C_{dr} - C_{dv}/\tau}{C_{dr}} \\ \frac{d\omega}{\omega} &= \frac{\omega_{dr} - \omega_{dv}\tau}{\omega_{dr}} \end{aligned} \tag{3.3}$$

When dealing with power losses, it is therefore correct to refer separately to the contribution of torque and speed losses that, due to the geometry of the system, depend also onto the transmission ratio existing between the considered driving and driven pulleys, see (3.3). The analysis hereby carried out was first proposed by [22]. The speed loss as defined in equation (3.3) is frequently called slip loss, and indicated as s.

A different approach for highlighting the parallel influence of torque and speed losses on power losses goes through the definition of efficiency. The efficiency η of the system is the ratio between output and input powers, measured on the driven (dv) and the driving (dr) pulley respectively. Defining the speed loss as in (3.3), it is possible to express efficiency as the product of two factors, one related to the speed loss and the other related to the ratio between the output and input torques:

$$\eta = \frac{P_{dv}}{P_{dr}} = \frac{C_{dv}\omega_{dv}}{C_{dr}\omega_{dr}} = \kappa(1-s) \tag{3.4}$$

This approach was used by [23], who expressed the torque factor as $\kappa = \nu\xi$, where ν is a proportional factor defined by the driving parameters and ξ is the damping factor of the belt, defining it as a property of the geometry of the driving system and of the material of the belt.

After a first general overview about the factors defining the power loss, it is important to have a close look on the geometry of the power transmission interface which is given by the pulley-belt contact and the free spans paths.

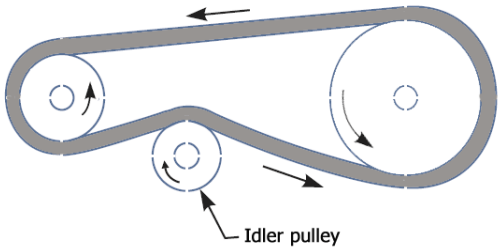

Fig. 3.1 Generic Belt Drive System Layout

As can be seen in Fig. 3.1, when the belt enters in contact with the pulley, it is bent around the pulley's circumference and it is compressed towards its surface according to the loading conditions of the belt itself. After covering the contact surface of the pulley the belt continues its motion in the free span where it is stretched towards the

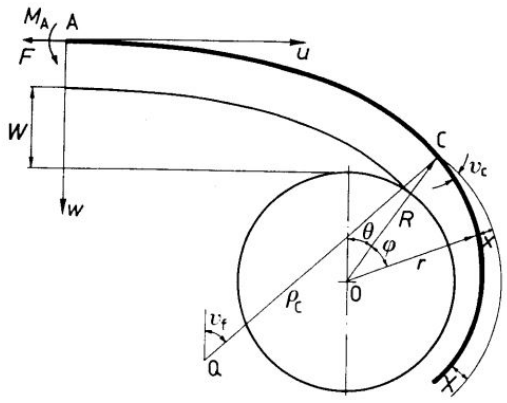

Fig. 3.2 Arching of the belt in the inlet zone [25].

next pulley of the transmission layout. After the free span, the belt is wrapped again around another pulley and compressed against its surface. During its motion around the driving system, the belt faces therefore a periodic motion of cyclic tension and compression deformation. The belt acceleration will have both a centrifugal and a stretching component due to its alternating motion as described by [24].
The behavior of the belt during its motion is severely affected by its material characteristics, especially its flexural rigidity and radial compressibility when wrapping around the pulleys and its longitudinal strain stiffness when pulled between two adjacent pulleys, and by the characteristics of the contact where the friction coefficient will let it adhere or slip over the pulleys.
When entering the pulleys, the belt draws a "transient" angle where the contact is not yet fully realized and which depends on the curvature of the free span of the belt due to its tension condition and elastic properties. In fig. 3.2 can be seen the arching of the belt and the consequent lack of contact angle [25].
Several authors worked into the attempt of categorizing the power losses resulting from the transmission phenomenology described above. Most of the classification is to be attributed to Professor Gerbert, whose abundant scientific contribution was produced along a period of over 20 years. At first, [26] distinguished the losses of V-belts due to external friction, that characterizes the sliding between belt and pulley, from those related to internal friction, linked to the hysteretical behaviour of the belt. In the same work, an additional differentiation was done for the calculation of external friction losses into two different operating conditions: the engaging and disengaging regions of the pulleys were treated differently from the power transmission

region, where the belt is working in the groove of the pulley at a certain distance from the entry and exit regions, where the influence of transverse force and radius of curvature can be neglected. Similarly, the hysteresis of the belt was divided into its bending, loading and compression components, which arise when the belt is bent on the pulley, is loaded and stretched by the force of the power transmission and compressed over the pulley surface.
In later publications [27, 28], Gerbert focused on the identification of the different mechanisms contributing to speed loss to more or less extent. He mainly identified four loss factors:

- Belt extension in its longitudinal direction, described by the classical creep theory and depending on the strain stiffness along the belt.
- Rubber compliance in the radial direction, which is function of the main cross sectional data of the belt and the material properties of the belt.
- Shear deflection, which depends on the shear modulus of the rubber part of the belt.
- Seating and unseating effects, given by the flexural rigidity, or bending stiffness, of the belt and the operating conditions of the belt in terms of tension.

The rubber compliance phenomenology was introduced at first by Childs and Cowburn [29] who attributed to it the reduction in efficiency of V-belts which do not match their pulley grooves. The radial compliance was indicated by a different behavior of the belt when entering the driving and the driven pulleys: due to a different pressure distribution the belt seats at a smaller radius at the entry to the driven then to the driving pulley. It is therefore possible to define a radial displacement of the tension cord determined by the tensile forces compressing the belt carcass towards the pulley groove.The analytical formulation of radial compliance effects can be read in Paragraph 3.2.1.
Focusing on the possibility of realizing the transmission with different types of belt, Gerbert [28] showed how all the loss factors of his theory can be treated in a unified way, made exception for the shear deflection for which a proper fictitious thickness needs to be adopted. As a matter of fact, the belt type defines a particular shear deflection pattern into the cross section of the belt.
Along his work [27], Gerbert divided the arc of contact into four regions, see Fig. 3.3, where the different loss mechanisms take place:

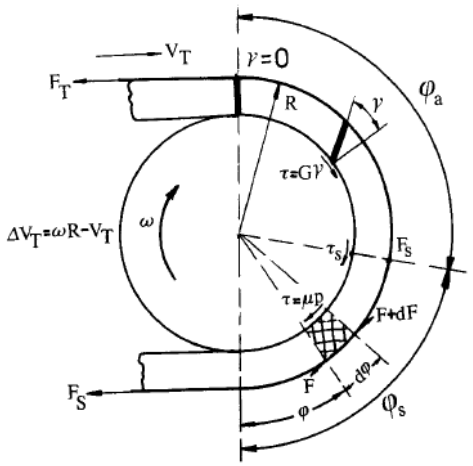

Fig. 3.3 Regions of the arc of contact in a driving pulley [27].

- Inlet angle, characterized by seating phenomena
- Adhesion arc, mainly dominated shear deflection with some influences of radial compliance
- Sliding arc, described creep and radial compliance
- Outlet angle, where unseating phenomena occur

The analytical formulation proposed by Gerbert can be found in Paragraph 3.2.1.
The general classification of speed losses proposed by Gerbert obtained good agreement among the authors who used it as basis for their further evaluations.
Childs highlighted the influence of the radial compliance also on torque losses by formulating his approximate sliding torque loss theory [30]. He also underlined how the warping and shearing of the belt carcass is responsible for torque loss in entry and exit regions of the belt-pulley contact, while it results in speed loss in the remainder of the contact arc as claimed by Gerbert. Childs identified the sources of torque loss into two main components: hysteresis losses, occurring when the belt is bent on and off a pulley; and sliding losses, that happen when the belt is wedged into and pulled out of its groove at entry to and exit from a pulley. This classification is the same proposed before by Gervas and Pronin in [31].
In his summary of losses mechanisms, Chen [22] proposed again Gerbert's classification for what concerns speed losses and indicated as torque losses sources:

- Bending hysteresis
- Wedge-in and wedge-out
- Radial (sliding) motion
- Compression

In recent years, most of the authors chose to experimentally analyse power losses considering overall torque and speed losses, without using any further specific classification [32], [33], [34]. [35] grouped the power losses contributors into hysteresis and frictional losses occurring at the entrance and exit regions of the pulleys due to the engagement/disengagement of the belt.

3.2 Pulley-Belt Contact Mechanics

Belt drive systems operate by friction between a belt and the surface of a pulley. The power transmission happens in terms of speed and torque transmission and all the possible power losses contributions that can determine an efficiency decrement are function of the tension state of the belt, the pressure distribution of the belt on the pulley arc of contact and/or the geometry and operating conditions of the systems. The basic formula describing the power transmission in a belt drive system is given by the Euler (or Euler-Eytelwein) model that was stated in 1762 in [36]:

$$\frac{T_T}{T_S} = e^{\mu\alpha} \tag{3.5}$$

Equation (3.5) defines the relationship between the tensions T_T and T_S at the two end points of a belt wrapped around a pulley at the tight and slack span respectively, depending of the friction coefficient μ and the wrap angle α, when they are at the limit point before gross slip. The formulation relays on two fundamental hypotheses:

- The belt is flexible and extensible
- The belt is thin enough to neglect shear and bending stresses

Equation (3.5) is commonly known as creep theory, where the name "creep" comes from the fact that frictional forces cause a change in belt tension, thereby causing the elastic belt to extend and contract. This action results in relative motion between the belt and the pulley surfaces which is termed elastic creep [37].
Taking into account the elastic deformation of the belt over the contact angle, the Reynolds model (1847), then Reynolds-Grashof model (1883), highlights the different behaviour of the belt over the adhesion and the sliding arcs, [38, 39].

$$T_T - mv^2 = (T_S - mv^2)e^{\mu\phi_s} \tag{3.6}$$

In eq. (3.6) the belt mass per length unit m, the tangential belt speed v and the sliding arc ϕ_s are taken into account to define the relationship between the belt tensions on the tight span T_T and on the slack span T_S. According to Reynolds [40], the tension is high at the entrance to a driver pulley, it is low at its exit, and slipping occurs in its exit region where the belt contracts. Also, the tension is low at the entrance to a driven pulley, the tension is high at its exit, and slipping occurs in its exit region. A further development of this theory was performed by Swift in 1928, [41].
In [37], Alciatore and Traver extended the creep theory to the case of multipulley configurations. The compatibility condition on the belt length results:

$$\sum_{i=1}^{n} l_i T_i = LT_0 \tag{3.7}$$

In eq. (3.7) l_i and T_i are the span lengths and tensions, L is the total belt length and T_0 is the initial preset tension of the system. In this formulation, Alciatore and Traver approximated the span length to extend between wrap angle bisectors, as shown in Fig.3.4.

When extending the theory with the inclusion of both bending and centrifugal effects the condition is modified in:

$$\sum_{i=1}^{n} l_i T_i = L(T_S + T_c) - \sum_{i=1}^{n} T_{bei} R_i \alpha_i \tag{3.8}$$

where T_S is again the tension on the slack span, $T_c = Q_c(\frac{v}{1000})^2$ (Q_c is an experimentally determined constant reported for SAE standard belt sections, v is the belt longitudinal speed) and $T_{bei} = \frac{Q_{be}}{D}$ (Q_c is an experimentally determined constant reported for the SAE standard belt sections, D is the pulley diameter) represent the

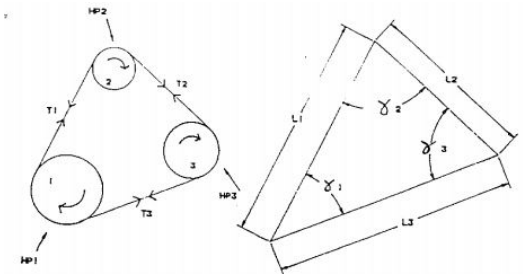

Fig. 3.4 Three pulley system with the span length approximation adopted by Alciatore and Traver [37].

increase in tension due to centrifugal and bending effects, respectively, R_i and α_i are the pulleys' radii and wrap angles.
The theory described so far perfectly applied to the leather or woven cloth flat and elastic belts as pointed out by Alciatore and Traver in [37]. With the introduction of different applications and new belt forms and materials, the creep theory became inadequate to describe the mechanics of certain belt types, such as those V-belts that contained steel reinforcement strands which were for all practical purposes inextensible [37]. A new theory was proposed by Firbank in 1970 [42] that took into account also the shear deflection of the belt over the adhesion arc. In this case the assumptions that were taken into account are the following:

- Within the arc of contact the fiber is inextensible and with negligible bending stiffness.
- The elastic properties of the belt envelope is linear and the shear deformation is constant through the belt thickness.
- The belt adheres to the pulley surface starting from the first contact point.
- The dynamic friction coefficients between belt and pulley have a constant value μ_k and the static coefficient has a limit value μ_{st}.
- The inertial effects of the belt can be neglected.

With this assumption both the adhesion (ϕ_a) and the sliding (ϕ_s) arc result active arcs of the transmission, where a tension variation (ΔT) takes places. Considering a driving pulley (dr), Firbank assumes that the tension varies according to the creep

theory along the sliding arc, resulting in a tension variation equal to:

$$\Delta T = T_2(e^{\mu_k \phi_s} - 1) \tag{3.9}$$

Along the adhesion arc, the tension variation results equal to the mean shear force per unit length multiplied to the arc length:

$$\Delta T = \frac{\alpha - \phi_s}{2} T_2 e^{\mu_k \phi_s} \mu_{st} \tag{3.10}$$

The equations of the difference and the ratio between tensions T_T and T_S resulting from equations (3.9), (3.10) are the following:

$$T_T - T_S = T_T \left[(e^{\mu_k \phi} - 1) + \frac{\pi - \phi}{2} \mu_{st} e^{\mu_k \phi} \right] \tag{3.11}$$

$$\frac{T_T}{T_S} = e^{\mu_k \phi} \left[1 + \frac{\pi - \phi}{2} \mu_{st} \right] \tag{3.12}$$

In [37], the extension of the shear theory to a multipulley configuration needed a new compatibility relation due to the assumption that length changes are considered to be negligible as the belt is assumed to be "inextensible". In order to obtain a compatibility condition for the shear theory in a multipulley configuration, the shear deformations in the belt envelope need to be considered and for the belt to return to its original condition upon completion of a cycle, the algebraic sum of the shear deformations γ must equate to zero:

$$\sum_{i=1}^{n} \gamma_i = 0 \tag{3.13}$$

The angle γ can be expressed as the ratio of the average shear stress in the arc f adhesion and the modulus of rigidity G of the envelope material, according to Firbank's belt model. The resulting equations are:

$$\gamma = \frac{1}{Gb} \left[\frac{\mu_s}{D} T_2 \exp^{(\mu_k \alpha)} \right] \tag{3.14}$$

for a driving pulley, and:

$$\gamma = \frac{1}{Gb} \left[\frac{\mu_s}{D} \frac{T_1}{\exp^{(\mu_k \alpha)}} \right] \tag{3.15}$$

for a driven pulley, where b is the belt width.
The previous formulations represent the basis for the understanding of the pulley-belt contact mechanics. Other formulations were proposed in literature ([43], [44], [45]) and a thorough description is provided by [46].
Several studies can be found in literature ([47], [46], [48]) providing an assessment of such equations and an experimental evaluation of the tension state of the belt over the pulley surface. In [49], Lubarda focused on the analysis and determination of the force variation in the belt before the state impending slip is reached throughout the contact region.
In [50] the shear theory was extended to dynamic conditions, where the motion of the pulley, or the belt, or both of them is given by a small amplitude vibration about the mean value. The proposed model was based on the following assumptions aimed at reducing the model complexity without neglecting any of the important effects affecting the considered dynamics:

- Within the arc of contact the fiber is inextensible and with negligible bending stiffness.
- The effect of bending are neglected.
- The effect of the centrifugal forces on the belt is neglected.
- The forces are transmitted from the fiber to the pulley by means of the shear in the belt envelope, made of elastomeric material.
- The belt is flat and is not compressible in the radial direction.
- The elastic properties of the belt envelope are linear and the shear deformation is constant through the belt thickness.
- The belt thickness h is assumed to be small compared to the wrap radius R of the tension member.
- The contact ends where the fiber reaches the final point the arc of contact.
- No shear deformation exists in the rubber layer at the inlet of the arc of contact.

In [50], Tonoli et al. defined the shear deflection on a belt of thickness h wrapped around a pulley of radius R as function of the difference between the angular dis-

placement of the pulley θ and the angular displacement of the fibers ϕ:

$$\gamma = \frac{R}{h}(\theta - \phi) \tag{3.16}$$

In [50] the case where only the pulley angular velocity has an harmonic component ($\omega_p = \omega_{p0} + \delta\omega_p \cos \omega t$), while the belt has a constant angular velocity ($\omega_b = \omega_{b0} = constant$), is considered. Going through some geometrical consideration, where the sliding arc is small in comparison to the adhesion arc ($\phi_s << \phi_a$), the shear deflection can be expressed as function of the time t and of the angular displacement of the fibers ϕ:

$$\gamma(t,\phi) = \frac{R}{h}\left\{ s\phi + \frac{\delta\omega_p}{\omega}\left[\sin \omega t - \sin \omega \left(t - \frac{\phi}{2\omega_{b0}} \right) \right] \right\} \tag{3.17}$$

Where s is the sliding factor, or slip, and takes into account the contributions of the mean speeds. In the case of a driving pulley it results $\omega_{p0} > \omega_{b0}$ and $s = \frac{\omega_{p0}}{\omega_{b0}} - 1$, while for a driven pulley we have $\omega_{b0} > \omega_{p0}$ and $s = \frac{\omega_{b0}}{\omega_{p0}} - 1$.
The assumption that the shear deformation is constant through the belt thickness and the belt material is elastic allowed to compute the torque $C(t)$ about the axis of the pulley as integral of the shear stresses σ on the arc of contact α. If the assumption of small thickness h of the belt envelope relative to radius R and a belt width of b are taken into account:

$$C(t) = R^2 b \int_0^{\alpha} \sigma(t,\phi) d\phi = R^2 b \left(\int_0^{\phi_a} G\gamma(t,\phi) d\phi + \int_{\phi_a}^{\alpha} \sigma(t,\phi) d\phi \right) \tag{3.18}$$

The first integral($0 < \phi < \phi_a$) represents the contribution due to the adhesion arc into account, the second ($\phi_a < \phi < \alpha$) that of the slip arc. Using such formulation [50] showed the possibility of representing the effects of the shear deformation of the rotational dynamics of the transmission and shear interaction between the pulley and the belt in terms of a series of a viscous damper and a spring. Further details on the implications of this model on the dynamics of the system are provided in Chapter 5.

3.2.1 Flat Belts, V- and V-ribbed Belts

At present, the automotive field employs V-ribbed belts predominantly. Such belts offer a compromise between the features of their predecessors, namely flat and V-belts. They guarantee flexibility and high power capacity [56]. In addition, the

features of these belts allow them to draw serpentine layouts around a high number of pulleys, thus avoiding the use of more than one belt. These belts have also improved reliability and fatigue life, while reducing wear, noise and vibrations. Serpentine V-ribbed belts can operate in both forward and backward directions and interact with ribbed or smooth pulleys.

The literature provided the manufacturers with precise guidelines to follow for the design of highly efficient V-ribbed belts, [57], [56], [58]. [58] studied thoroughly how the belt load is shared between the rib flanks and the rib roots. Such load distribution causes wear of the belt changing its shape differently in three separate regions. The results of such studies lead to precise indications on the geometry design required to decrease the power losses due to wear and to maintain constant the traction capacity of the belt.

Due to their geometric characteristics, flat belts, V and V-ribbed belts and their tension states can be described by adopting different formulations. Della Pietra et al. [47] showed how the Grashof model results adequate for the description of flat belts, while it is better to adopt the Firbank formulation when referring to V-belts. V-belts have indeed a higher thickness where a shear deflection can happen more easily and can have a higher impact over the tension state of the belt.

In the case of automotive front-end accessory drives (FEAD), the adoption of low profile multiribbed belts is compelled by the combination of the requirements of flexibility, that are typical of flat belts, and that of high power capacity that characterizes the V-belts. Furthermore, multiribbed belt devices satisfy the stringent requisites of low noise and vibration levels, fatigue life and reliability, as pointed out by [50]. This type of belt, allows to draw complicated serpentine layouts by transmitting high power amounts thus avoiding to use more then one belt.

Modern V- and V-ribbed belts used in automotive applications as well as in conveyor belts are built up of several functional layers. The load is carried by a flexible member made of high stiffness fibers or steel cords (tension member). It is bounded by a protection layer on the top to avoid mechanical damages and by a rubber or viscoelastic layer in the bottom (belt envelope). This layer provides the required shock absorption and the frictional qualities to grip the rigid pulley. Moreover it transmits the load from the pulley surface to the tension member. Compared to V-belts, the higher flexibility of V-ribbed belts leads to a maximization of the power capacity and a minimization of the wear [56].

In [56], Hansson discussed the aspects that need to be taken in consideration for

the design of a V-ribbed belt drive for maximum power transmission and service life. Hansson highlights the influence of the variation of the belt wedge angle on the pressure distribution and the importance of obtaining a uniform pressure distribution to maximize the torque and power capacity of the transmission. The pressure distribution changes with the pulley diameters: at the same belt tension, the radial pressure is lower on a pulley with large diameter and higher in a smaller pulley. Due to the higher stiffness of the pulley compared to the belt, in the contact zone the belt is deformed into the geometry of the pulley and pressure peaks result into belt wear while the material accumulates in the bottom of the groove. According to Yu et al. [58], the rib shape changes in three regions owing to wear: at the top of the rib, a shoulder develops; at the root of the rib, debris piles up; in between, the rib wears without change of slope. Considering a drive consisting of pulleys with different pitch radii, the belt results most worn at the smallest pulley owing to the highest pressure and most slip. In [56] the dependency of the drive's torque capacity from pressure distribution is eventually shown as follows:

$$C_{tr} = 2n \int_0^{\alpha} \frac{\mu p(r,\alpha) r^2}{\cos \beta_b(r)} dr d\alpha \tag{3.19}$$

In eq. (3.19), the transmittable torque C_{tr} is expressed as function of the number of pulleys n, the friction coefficient μ, the pressure $p(r,\alpha)$, the radius r, the cosine of the belt wedge angle β_b integrated over the wrap angle α. The belt wedge angle β_b is different from the pulley wedge angle β_p and can be described through a linear relationship of the pulley curvature, $\beta_b = \beta_{b,0} - \frac{k(r)}{R}$.
In their work, Yu et al. [58], studied experimentally how the load is shared between the rib flanks and the rib roots and then focused on the reduction in traction capacity of the belt due to increase root loading as wear progressed. [58] eventually suggests an improved V-ribbed belt section design, with a new rib shape, arrangements of materials and changed manufacturing tolerances between the belt rib groove and the pulley rib tip shape.
From a modelling point of view, a V-ribbed belt can be considered as the composition of a number of V-belts equal to the ribs' number mounted on the top of a unique flat belt. According to their characteristics and the transmission configurations, appropriate choices need to be done for what concerns the speed and torque losses effects adapt to describe them.

3.2.2 Speed Losses

The analytical formulation of speed losses needs to be conducted to Gerbert's work, [27, 28], with some specifications from Childs, [29, 30]. The formulation takes into account four main contributions and is at first given for flat belts and then extended to the case of V- and V-ribbed belts.
As a first step, the belt creep is defined as the difference between the tangential velocities at the slack (v_S) and tight (v_T) sides arisen because of the increasing tension [27]. For a driven pulley it is defined:

$$v_T = v_S(1 + s_{cr}) \tag{3.20}$$

where the slip for belt creep, s_{cr}, is defined as

$$s_{cr} = \frac{\Delta\omega}{\omega_{dv}} = \frac{T_T - T_S}{c} \tag{3.21}$$

In eq. (3.21), the coefficient c represents the belt extension modulus or longitudinal stiffness, tension per unit strain. The belt tensions of the tight and slack spans are linked one to the other through eq. (3.5), (3.6) or (3.9, 3.10) as described in the previous section. Instead of the complete wrap angle α, the sole sliding arc ϕ_s is taken into account.
Considering a radial load $F = T_T/R$ pressing the belt against the pulley in its seating region, it is possible to express the speed losses due to the rubber compliance depending on its geometric characteristics and material properties [27]. The resulting speeds on the slack and the tight spans can be expressed as function of the compression $x = \frac{1}{k}F$, where k indicates the belt radial stiffness, and lead to an update of the slip formulation, corresponding to an additional decrease in the output speed:

$$v_s = (R - x_s)\omega_{dv} \tag{3.22}$$

$$v_T = (R - x_T)\omega_{dr} \tag{3.23}$$

$$s_{rc} = \frac{\Delta\omega}{\omega_{dr}} = \frac{T_T - T_S}{c} + \frac{T_T - T_S}{kR^2} \tag{3.24}$$

In [29], Childs and Cowburn highlighted how the influence of the radial compliance $g = \frac{1}{k}$ on the losses is dominant and how the misfit of a belt in a pulley groove causes larger losses over the full range of practical working tensions. The radial compliance

g is also indicated as cause of additional torque losses in [29]. This will be further described in the next section.
Referring to the slip in case of rubber compliance, s_{rc} in eq. (3.24), it is possible to obtain a non-dimensional formulation considering the coefficient of traction λ, the relative stiffness c_* and the non dimensional speed reduction $\Delta\omega_*$, as described in the following:

$$\lambda = \frac{T_T - T_S}{T_T + T_S} \tag{3.25}$$

$$c_* = \frac{c}{kR^2} \tag{3.26}$$

$$\Delta\omega_* = \frac{c}{T_T + T_S}\frac{\Delta\omega}{\omega_{dr}} = (1 + c_*)\lambda \tag{3.27}$$

Equation (3.24) is a linear relationship between the non dimensional speed reduction $\Delta\omega_*$ and the coefficient of traction λ.
The description of the speed reduction can be further updated considering the shear deflection effect on both the driving and the driven pulleys, Δv_{T*} and Δv_{S*} respectively. The complete formulation is given by:

$$\Delta\omega_* = (1 + c_*)\lambda + \Delta v_{T*} + \Delta v_{S*} \tag{3.28}$$

where:

$$\Delta v_{T*} = \frac{T_S}{T_T + T_S}\frac{T_a/T_s - 1}{\cosh(G_*\phi_a) - 1} \tag{3.29}$$

$$\Delta v_{S*} = \frac{T_a}{T_T + T_S}\frac{T_S/T_a - 1}{\cosh(G_*\phi_a) - 1} \tag{3.30}$$

In eqs. (3.29) and (3.30), F_a is the belt tension on the adhesion arc of the pulley ϕ_a, and $G_* = \frac{GBR^2}{cH}$ is a non dimensional shear modulus, where B is the belt width and H is the rubber layer thickness.
Differently from Gerbert, Childs and Cowburn did not introduce the shear effects as an additional speed loss but they indicated such effects as a modification of the belt strain stiffness c in certain load conditions [30]. In the formulation suggested in [30], the speed losses at low torques, when the so-called active arc is smaller then the total arc of contact, are indicated as:

$$\frac{\Delta\omega}{\omega} = \left(\frac{1}{c} + \frac{g}{R^2}\right)(T_T - T_S) \tag{3.31}$$

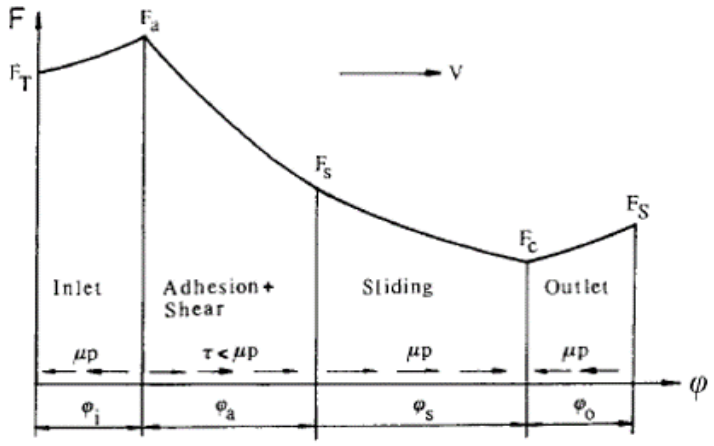

Fig. 3.5 Tension variation over a driving pulley [27].

which is the same as (3.24) where the radial compliance is $g = 1/k$.
For speed losses above the critical torque and increased active arcs, the speed loss is indicated as proportional to the arc of contact, the belt geometry and the shear modulus of the rubber layer:

$$\frac{\Delta\omega}{\omega} = \frac{T_T - T_S}{c\sinh^2\left(AR\frac{\alpha}{2}\right)} \tag{3.32}$$

where $A = \frac{Gb}{ch}$, with G belt carcass shear modulus, b carcass width, h carcass thickness, c belt extension modulus.
Childs and Cowburn formulation highlighted how the speed losses increase with smaller radii ($\propto \frac{1}{R^2}$) and with smaller contact arcs ($\propto \frac{1}{\alpha}$).
Taking into account the change of the radius of curvature that takes place into seating and unseating regions, it is possible to update the formulation of the adhesion and sliding arcs, ϕ_a and ϕ_s, used in (3.28). As a matter of fact, including the inlet and outlet arcs in the analysis, four different zones of the arc of contact can be identified where the tension ratio varies differently. The inlet and outlet zones are defined by the true points of contacts C_s and C_u which depend on the bending stiffness of the belt. An additional rotational speed function of the actual radius of curvature ρ is introduced as follows:

$$\dot{\theta} = \left(1 - \frac{R}{\rho}\right)\omega \tag{3.33}$$

and causes an additional belt speed, namely the bending velocity, $\Delta v_b = H\dot{\theta}$, where H is the rubber layer thickness.
In Fig 3.5 an example is depicted taking into account the tension variation over a driver pulley. The angles considered are the same as shown in Fig. 3.3. In this case the following equations hold:

$$\phi_s = \alpha - \phi_a - \phi_i - \phi_o \tag{3.34}$$

$$\phi_i = \phi_{Ai}\left[1 - \sqrt{\frac{R/H}{1-R/\rho_{Ci}}\frac{\Delta v_T}{v}}\right] \tag{3.35}$$

$$\phi_i = \phi_{Ao}\left[1 - \sqrt{\frac{R/H}{1-R/\rho_{Co}}\left(\frac{\Delta v_T}{v} + \frac{\Delta v_S}{v}\right)}\right] \tag{3.36}$$

As shown in Fig. 3.3, in eqs. (3.35) and (3.36) A is the point where $\Delta v_b = 0$. The radius ρ_{Ci} indicates the radius of curvature at point C in the inlet zone and the radius ρ_{Co} indicates the radius of curvature at point C in the outlet zone as previously shown in Fig. 3.2.
The introduction of the inlet and outlet arcs lead to modified solutions for the Euler's equation (3.5) and its evolutions, (3.6) or (3.9,3.10), by considering three additional belt tensions (F_a adhesion, F_s sliding, F_c contact tensions) aside from the tight and slack span tensions. The following cases of the Euler's formula arise for a driving pulley:

- In the inlet zone, $T_T/T_a = e^{-\mu\phi_i}$
- In the adhesion zone, $T_a/T_s = \kappa_{as}(\phi_i)$
- In the sliding zone, $T_s/T_c = e^{\mu\phi_s}$
- In the outlet zone, $T_c/T_S = e^{-\mu\phi_o}$

In the inlet and the outlet zones the direction of the frictional forces in the seating and unseating regions results counterdirected to those in the adhesion and sliding zones for a driving pulley, while they will be equal when considering a driven pulley.

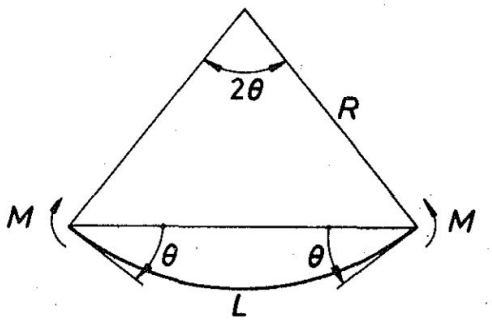

Fig. 3.6 Test rig for bending losses [26].

3.2.3 Torque Losses

Torque losses in a belt transmission are directly linked to the hysteretic behaviour of the belt material. An analytical formulation for this type of losses results less immediate then in the case of speed losses and less attempts can be found in literature which mainly proposes experimental approaches to define the single contributions. Only in the last years, some major work has been carried on towards an analytical and homogeneous formulation [35, 51–53].
In his work [26], Gerbert focused on the hysteresis losses in a V-belt. He expressed the loss contributions for bending, loading and compression as the corresponding energy loss for belt length multiplied by the belt speed. In his study, he then measured experimentally the energy losses separately.
To determine the bending losses he used a test rig to measure the relation between the bending moment M and the deflection angle θ. Fig 3.6 depicts the principle used in the test rig where bending moments are applied in the ends of a piece of belt of length $L = 100$mm.The belt is bent from an intially straight line ($\theta = 0$) to a certain angle θ and then bent back to $\theta = 0$. As shown in Fig. 3.7 the area between the curves represents the energy loss for the belt length $L = 100$mm. The energy loss per unit length, W_{be}, is defined as:

$$W_{be} = \frac{2}{l} \int_0^{\theta} (M_{load} - M_{unload}) d\theta \tag{3.37}$$

When the belt is bent on and stretched off the pulley the power loss is:

$$P_{hbe} = W_{be} v \tag{3.38}$$

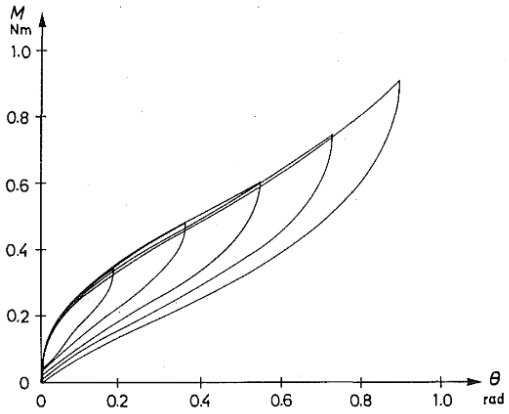

Fig. 3.7 Bending moment as function of deflection angle [26].

Resulting in the total bending torque loss due to hysteresis for one pulley while the radius of curvature is calculated from $R = l/2\theta$:

$$C_{hbe} = W_{be}R \tag{3.39}$$

Gerbert determined the hysteresis losses resulting from belt loading with the longitudinal spring constant of a V-belt (l=616 mm) which he loaded and unloaded in a tensile testing machine. The energy loss for the belt length L is represented by the area between the loading and unloading curve. The calculated energy loss per unit length is $W_l = 0,045\text{Nm/m}$. To the fact that the belt force increases at the driven pulley and decreases at the driving pulley the length per unit time is loaded and unloaded which gives the power loss due to belt loading for the whole belt drive:

$$P_{hl} = W_l v \tag{3.40}$$

For each single pulley the torque loss can be obtained as follows:

$$C_{hl} = W_l \frac{R}{2} \tag{3.41}$$

To identify the hysteresis losses due to compression of the belt into the pulley groove Gerbert used a piece of V-belt ($l = 48\text{mm}$) which he compressed between two wedge formed steel plates. To prevent sliding the plates were covered by emery cloth. Similar to Fig. 3.7 the relation of the compressive force F_z and the change in belt

width Δb could be plotted. The area between the loading and unloading curve represents the energy loss for the belt length l. When the belt enters the pulley it is compressed and when it exits the pulley it is unloaded. This gives the power loss due to belt compression:

$$P_{hcom} = W_{com} v \tag{3.42}$$

The torque compression loss for each pulley is:

$$C_{hcom} = W_{com} R \tag{3.43}$$

Childs and Cowburn [30] proposed an empirical expression for the torque loss due to radial sliding ΔT_s between the belt and the pulley. This formulation was provided while experimentally characterizing the rubber compliance speed losses and relied on the introduction of a dimensionless belt deformation parameter $(gEI/R^4)^{1/2}$, where g is the rubber compliance of the belt and EI is the belt bending stiffness. Focusing of the loss comparison due to smaller radii, the authors showed that for a range of belts for which the friction coefficient μ varied little, it holds:

$$\Delta C_s = (0.0075 \pm 0.05)\{(T_T + T_S)R\}(gEI/R^4)^{1/2} \tag{3.44}$$

Such formulation is an evolution of Gerbert's expression for μ up to 0.4, given by [26]:

$$\Delta C_s = \mu (T_T + T_S) R \left(0.01 + 0.0033 \ln \frac{10^5 EI}{R^4 k_1} \right) \tag{3.45}$$

where k_1 is again inversely proportional to the radial compliance g but also depends on other belt and pulley parameters. In eqs. (3.44) and (3.45), F_T and F_S are the belt tension on the tight and slack span respectively, R is the pulley radii which are equal. In his literature review about torque losses for rubber CVTs [22], Chen cited Childs and Cowburn [30] when dealing with losses in radial sliding. He then proposed Gervas expression for bending hysteresis [54]. Gervas introduced the torque loss in a V-belt drive due to belt flexure, or bending, ΔM_{be} as function of a coefficient of recovery in tension by means of an empirical formulation.

$$\Delta C_{be} = \frac{2 \sum_i^n (1 - v_f) E_f I v}{75} \sum_i^n \frac{1}{4R^2} \tag{3.46}$$

For what concerns the torque loss due to the belt wedge-in and wedge-out of pulleys, Chen referred to the formulation suggested by [55]. Such formulation makes use of two influence factors for the driving and driven pulleys, k_{dr} and k_{dv} respectively.

$$\Delta C_w = T_T R_{dv} k_{dv} \left(\frac{1}{c^2} - k_{dr}^2 \right) - \frac{T_{dr} R_{dv}}{R_{dr}} (1 - k_{dv} k_{dr}) \tag{3.47}$$

The last contribution that Chen considered in his study was the loss due to transverse compression, adopting Gervas and Pronin's formulation, [31].

$$\Delta C_{com} = \frac{(1-\zeta)(T_T - T_c)^2 bv}{2E_{com} D^2 h} \left(\frac{\cos \beta/2}{\tan \beta/2 + \mu} \right)^2 \tag{3.48}$$

In eq. (3.48), ζ and E_{com} are the coefficient of recovery and the Young's modulus in compression, respectively; b and h are the width and thickness of the belt; T_c is the belt tension generated from the centrifugal force; v and β are the speed and wedge angle of the belt and μ is the coefficient of friction, D the pulley diameter.
In 2014 [35], Bertini et al. gave an analytical formulation of the hysteresis losses of a rubber V-belt continuously variable transmission (CVT), composed by a driving and a driven pulleys. The work focused on the definition of the strain history of the belt and related the power losses in the longitudinal and transverse direction to the identified strain cycles.

Figure 3.8 shows the longitudinal strain history of the belt at distance y from the neutral axis while it performs a complete revolution, as described by Bertini et al. The path designed by the belt around the two pulleys and the free spans is subdivided in sections where the belt tension, the belt characteristics and the system geometry define the different strain conditions. The path starts with the segment A-A' and its tension T_1, then the belt enters the driving pulley (A'-B) which leads to an increase of the belt strains due to winding over the pulley. While the belt travels through the pulley groove the belt tension decreases to a value nearby the exit of the pulley which includes the tension of the slack end T_0 and the tension due to winding over the pulley (C). After the belt exits the pulley groove in point (D) the belt tension is equal to the tension T_0 (D-D') of the slack end. The belt enters then the driven pulley which leads to a sudden increase of tension due to winding over the pulley radius (E). Due to frictional sliding the belt tension increases over the driven pulley to tension which is the sum of tension T_1 and the tension due to winding over the pulley (F). While the belt leaves the driven pulley (A) the belt tension is equal to the tension of

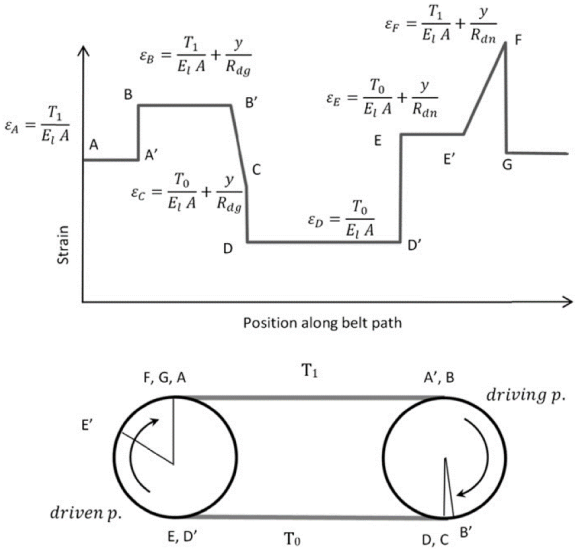

Fig. 3.8 Strain history of the belt a distance y from the neutral axis [35].

the tight end T_1.

The total torque losses as defined by [35] are divided into losses due to longitudinal and lateral deformation. The sum of the two losses equates the total power loss due to hysteresis:

$$P_h = P_{h,\parallel} + P_{h,\perp} \tag{3.49}$$

$$P_{h,\parallel} = \Psi E_\parallel bv \left\{ \frac{T_1 - T_0}{E_l S} \left[\frac{T_1 - T_0}{E_\parallel S} h + \frac{h_{sup}^2 + h_{inf}^2}{\min(R_{dr} R_{dv})} \right] + \frac{h_{sup}^3 - h_{inf}^3}{3} \left(\frac{1}{R_{dr}^2} + \frac{1}{R_{dv}^2} \right) \right\} \tag{3.50}$$

$$P_{h,\perp} = 2\Psi \frac{c^{-1/d}}{d+1} \left[\left(\frac{T_{1n}}{2\tan(\frac{\alpha}{2} + \phi_R)} \right)^{\frac{d+1}{d}} \left(\frac{1}{R_{dr}^{\frac{d+1}{d}}} + \frac{1}{R_{dv}^{\frac{d+1}{d}}} \right) \right] v \tag{3.51}$$

In equations (3.50) and (3.51), Ψ is a dissipation coefficient representing a sort of internal damping that was estimated by comparison with experimental data, $E_\parallel$ is the belt longitudinal elastic modulus, S is the cross section area, b and v are the average belt width and the average belt speed, $h = h_{sup} - h_{inf}$ is the total belt thickness given by the difference between the coordinates of the upper and lower surfaces of the belt cross section with respect to the neutral axis, with R_{dg} and R_{dn} are indicated the radii of the driving and driven pulleys, C is the elasticity coefficient of the belt,T_{1n} is the belt net tension, $\frac{\alpha}{2}$ represents the half angle of the pulley, and $\phi_R = \arctan(f_R)$ where f_R is the radial component of friction.

According to [35], the losses due to longitudinal hysteresis result proportional to the belt speed, the second power of the torque and to the third power of the belt thickness (inertia moment of the cross section). Inversely proportional are the losses to the second power of the pulley radii. The second contribution to hysteresis losses due to lateral deformation of the belt material conveys the losses caused by the lateral deformation which arise from the motion of the belt mate-rial into the pulley groove. The power losses are proportional to the belt speed and non-linearly related to the maximum belt tension, to the inverse of the pulleys radii, to the inverse of the friction coefficient and to the inverse lateral elasticity coefficient C.
[51–53] represent the latest work on the modelling of power losses in belt drive system. The case of front end accessory drives was taken into account for heavy duty trucks. A software was developed for the assessment of the power losses and the different loss contributions to the belt hysteretic behaviour. This work represents an analytical representation of the experimental studies that were performed by Gerbert as the different contributions to the power loss are expressed as energy loss per unit length multiplied by the belt speed.

$$P_{loss} = W_h S R \omega \tag{3.52}$$

$$W_h = \pi E'' \varepsilon_a^2 \tag{3.53}$$

In equations (3.52) W_h represents the energy loss per volume (J/m^3), S is the belt section area and $v = R\omega$ is the belt speed. The energy loss per volume expressed by eq. (3.53) corresponds to the area of the hysteresis loop in a stress strain diagram, see Fig. 3.9, and depends on the strain amplitude ε_a and on the elastic loss modulus E'', which can be expressed as a linear function of the strain amplitude itself. According to [51–53] for different types of hysteresis power losses, the loss contribution can be calculated by finding the proper strain amplitude ε_a.

$$\varepsilon_{abe} = \frac{|(R \mp x)\gamma - R\gamma|}{E\gamma} = \frac{x}{R} \tag{3.54}$$

$$\varepsilon_{al} = \frac{\Delta T}{E'S} = \frac{T_T - T_S}{E'S} \tag{3.55}$$

$$\varepsilon_{afcom} = \frac{p_z}{c}; \varepsilon_{arcom_{in}} = \frac{p_v}{k}; \varepsilon_{arcom_{out}} = \frac{p_v}{k_{Ht}} \tag{3.56}$$

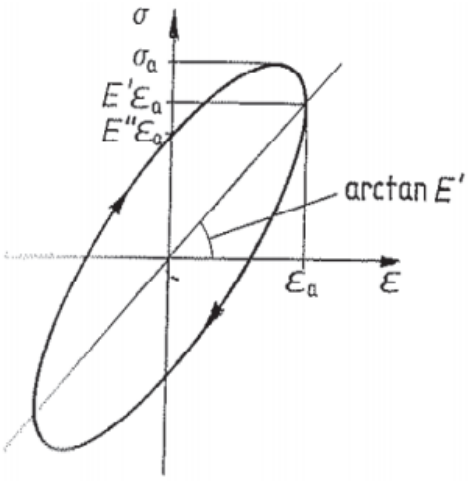

Fig. 3.9 Hysteresis loop in a stress strain diagram [51].

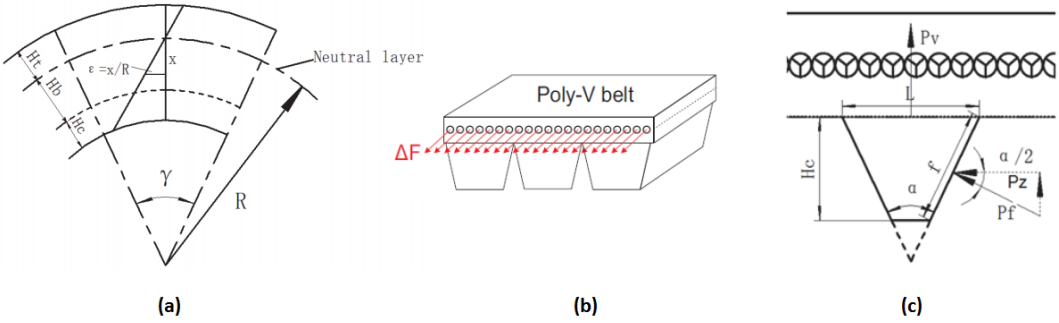

Fig. 3.10 Scheme of different contributions to the hysteresis losses [53].

In eq. (3.54), (3.55), (3.56) the expression for the strain amplitude for bending losses (ε_{ab}), for stretching or loading losses (ε_{al}) and for flank and radial compression losses (ε_{afc}, ε_{arc_i}) are shown. The characteristics of each hysteresis loss contribution are highlighted in Fig. 3.10. The strain due to belt bending around the pulley at a distance x from the cord layer (indicated as the neutral layer) depends on the pulley radius R. In eq. (3.54) γ is the angle , and the $\pm$ sign refers to the different portions of the belt, being $R-x$ for the ribs and central layer, or $R+x$ for the top layer. The strain due to the belt loading (or stretching) is directed in the longitudinal direction of the belt and depends on the belt characteristics, through the belt storage modulus in the longitudinal direction E' and the belt cross section S, and on the tension difference $\Delta F = F_T - F_S$ existing between the tight F_T and the slack F_S spans. The

compression losses are due to the flank pressure P_f exerted by the belt on the pulley ribs and are directed horizontally through the component p_z on the belt rib or radially with p_v. In (3.56) c is the rib axial stiffness, corresponding to the rubber stiffness E', k is the belt radial stiffness that needs to be considered when the belt-pulley contact is realized on the ribs side and k_{Ht} is the radial stiffness of the top layer, which defines the belt behavior for contacts on the back side.
According to Gerbert [28], the formulation of creep, radial compliance and seating and unseating effects is homogeneous for flat, V- and V-ribbed belts. These effects can ultimately be neglected for V-ribbed belts thanks to their technological development that provided them with high longitudinal stiffness and low bending stiffness, [56, 58, 53]. In the case of the shear deflection a further development of the theory expressed in eq. (3.28) needs to be considered. The shear contribution in eq. (3.28) depends on the parameter $G_* = \frac{GBR^2}{ch}$ where the belt thickness h plays a major role. A fictitious thickness H_χ needs to be considered to make a distinction among the possible belt types:

- For flat belts the belt thickness is constant in the axial direction so it results $H_\chi = h$, where h is defined as the distance from the cord layer to the pulley surface
- For V-belts the friction is transferred to the cord layer from the sides of the V-belt resulting in both a radial and an axial contribution to the shear deflection. It results $H_\chi = H\frac{1+g_\xi \xi^2}{g_C}$, where H is defined as the distance from the cord layer to the bottom of the belt, g_ξ=0.659 and $g_C = 1.2$ are shear deflection factors and $0 < \xi < 1$ indicates the utilized fraction of friction
- For V-ribbed belts, a composition of the flat and V-belts formulations is to be considered: $H_\chi = \left(h + \frac{H}{g_G}\right)(1 + g_\xi \xi^2)$

3.3 Experimental Characterization of Efficiency

Summarizing the literature research performed and described above, some indications can be provided about the qualitative behaviour that can be expected from a belt drive system in terms of power losses and transmission efficiency.
The effect of torque and speed losses acquire more relevance according to the load

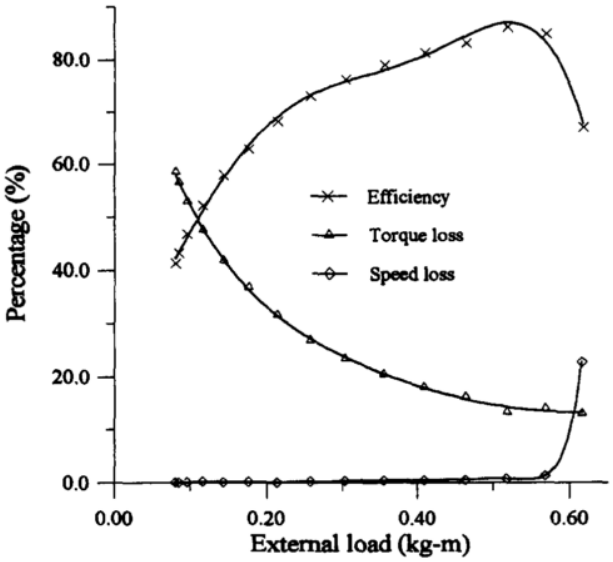

Fig. 3.11 General behaviour of speed losses, torque losses and efficiency in a rubber belt CVT at 2400rpm [22].

conditions of the transmission. For low loads, the speed losses constitute less then the 3% of the losses and can be neglected, while the torque losses predominate and the efficiency trend retraces the percentage torque loss [29, 30]. For what concerns speed losses in automotive FEADs, the belt creep, the rubber compliance and the seating and unseating effects can be neglected in a good approximation level. The speed loss in low load conditions can be attributed to shear losses and can affect the rotational dynamics of the transmission. When the load state overcomes the maximum and optimum transmittable torque value and the adhesion limits in terms of slipping angle are reached, the speed loss becomes predominant bringing the belt in a gross slip condition and limiting the power that can be successfully transmitted [29, 30]. For high loads the torque losses become negligible and the efficiency trend is defined by the percentage speed loss behaviour. In this case the simple belt creep formulation for the slip is sufficient to describe the overall speed loss without considering any other loss contribution. This phenomenological analysis can be seen in Fig. 3.11. Fig. 3.11 refers to a rubber belt CVT transmission which involves two pulleys with continuously variable radii characterized by the same loss sources of a standard two-pulley belt transmission [22]. The behaviour shown in Fig. 3.11 was experimentally confirmed by Manin et al. in [59] where a comparative analysis

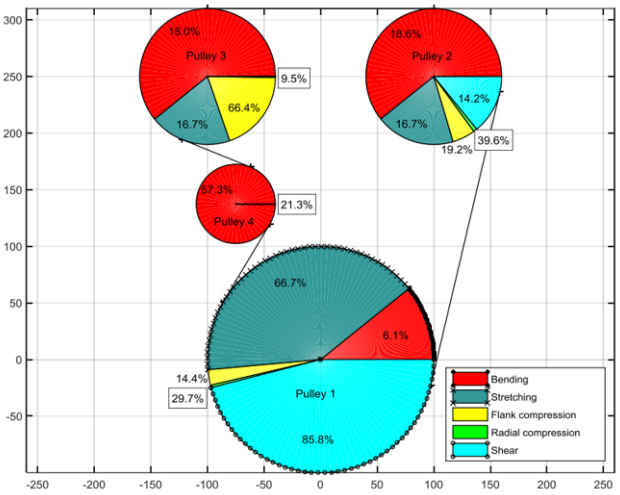

Fig. 3.12 Identification of the influence of the different power losses contributions due to hysteresis phenomena [53]

was done between six different belts considering the influence of friction coefficient and longitudinal stiffness on the efficiency for different operating conditions with variable setting tension, transmitted torque and rotation speed. The study showed how the efficiency at low torque, before gross slip occurs, does not depend on the belt pretension wile the slip limit torque increases with the initial setting tension. This result is shown in Fig. 3.13 on the left and is the same that was showed by Childs and Cowburn in [30] as Fig. 3.13 highlights.

The different contributions to the torque losses depend on the variables of the system. For increasing speeds, the bending losses will increase as they depend on the bending frequency of the belt around the pulleys. At the same time, an additional pulley will lead to an increase of bending losses for the transmission. The increase of torque load provided by the alternator or the other auxiliaries of the transmission will determine a higher tension difference between tight and slack spans leading to an increase in stretching losses. At the same time a higher tension difference will determine an increase of the pressure exerted by the belt on the pulleys and therefore an increase in compression losses. However due to the advanced design of the surface of V-ribbed belts compression losses represent the smaller contribute to the overall power losses. An example of this analysis was provided by Silva et al. in [53] as shown in Fig. 3.12. Balta experimentally investigated the influences of different operating conditions both on torque losses [34] and on speed losses

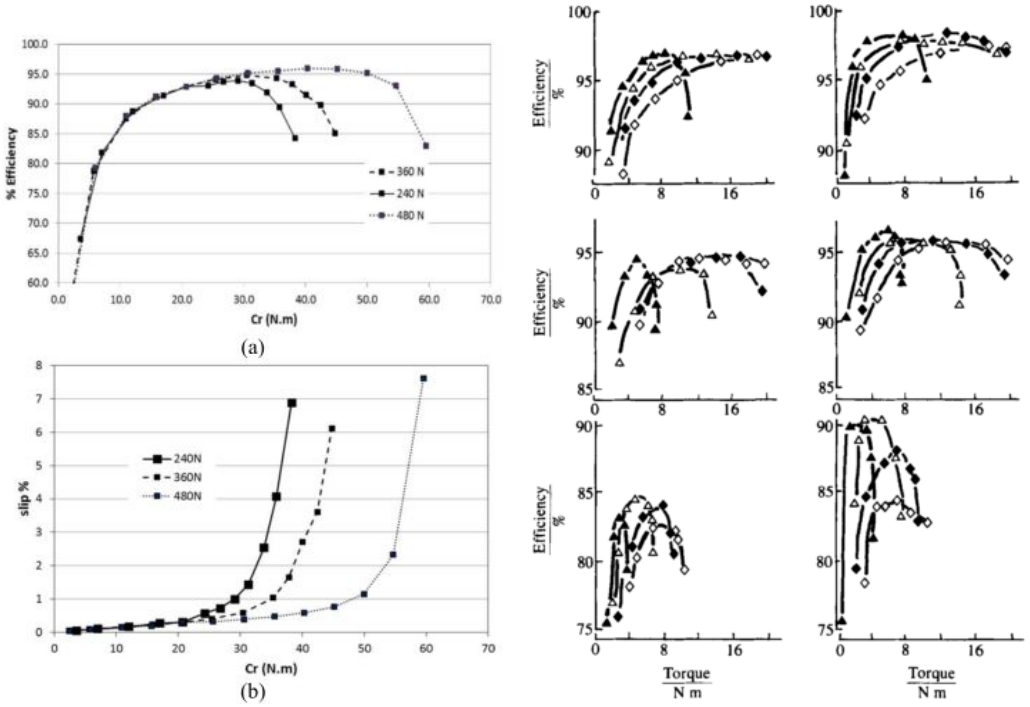

Fig. 3.13 Influence of the belt preload on the efficiency, on the left [59] and on the right [30].

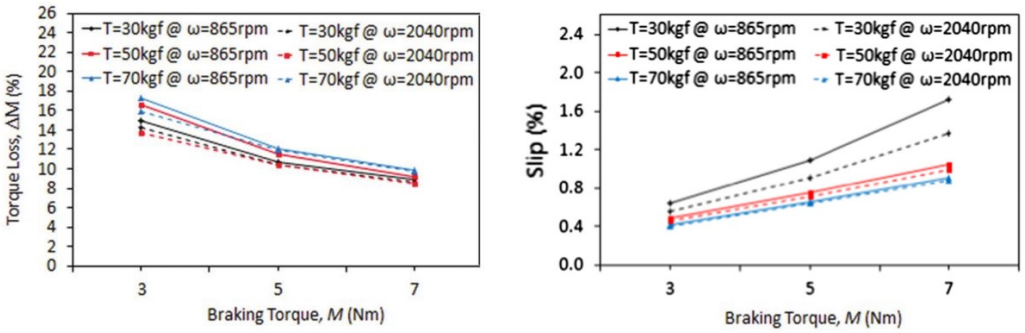

Fig. 3.14 Influence of braking torque on torque loss [34] and speed loss [33].

[33]. For what concerns the torque losses, [34] investigated the effects of the pulley diameter and speed, the belt length, pre-tension and material, and the braking torque on the torque losses in V-ribbed belt drives using a 2 equal sized pulleys test rig. From the study conducted, that included also a statistical analysis with the RSM and ANOVA methods, the factors that resulted to have the highest effect on the percentage torque losses were the braking torque and the pulley diameter, while the factors with the least effect were the pulley speed and the belt pretension. [34] showed experimentally the decrease of the percentage torque loss for increasing braking torque values, as shown in Fig. 3.14. As a matter of fact, the absolute torque loss slightly increases with increasing braking torque due to the fact that the higher difference between the belt tensions on the slight and tight spans exacerbates the hysteresis effect associated with longitudinal stretching and contraction of the belt. However, this effect does not increase as much as the braking torque and as a result the percentage torque loss shows a decreasing trend with increasing braking torque. In [33] the same parametric analysis is performed for what concerns the transmission speed losses. The experimental analysis showed how the belt slip increases with smaller pulleys' radii, lower belt pretension and higher braking torque. The case of increasing braking torque is shown in Fig. 3.14. The slip results instead almost constant for increasing pulley speeds.
All the works that focused on the experimental characterization of the efficiency on a BDS and that were cited in this section took into consideration the case of a 2 equal sized pulley transmission. No experimental investigation on multipulley systems was found in literature.

3.4 Chapter Conclusions and Remarks

In this chapter an extensive literature overview is provided concerning the power losses of belt drive systems. The main contributions are identified and described both qualitatively and analytically, showing their impact on the overall efficiency of the transmission. A big effort was done to identify the main aspects that define the specific case of an automotive front end accessory drive which is a multipulley system mounting a V-ribbed belt.
The considerations that resulted from the research lead to two main conclusions. On one side, the choice of taking into account the shear deformation when modelling the

dynamic behaviour of a BDS was motivated. As a matter of fact, the characteristics of high longitudinal stiffness and low bending stiffness of a V-ribbed belt allow to neglect the speed losses due to the creep, radial compliance and seating and unseating effects. Additionally, the hysteresis losses of the belt have time constants not comparable with the rotational dynamics of the system so they cannot be introduced in a dynamic model. On the other side, a complete understanding of speed and torque losses allowed to show the possible trends of the efficiency for different operating conditions and for different system parameters. This preliminary study constitutes the basis of the experimental investigation on the transmission efficiency that will be performed in the present work, that will compare the performances of multipulley automotive BDS for traditional and micro-hybrid configurations.

Chapter 4

State of the Art: Dynamics of Belt Drive Systems

The dynamics of belt drive system have been abundantly investigated by the authors over the years. Two main types of system vibrations exist in belt drive systems: (1) rotational vibrations of pulleys with the belt spans serving as coupling springs and (2) transverse and axial vibrations in the various belt spans, [60]. Additionally, the dynamics of the belt tensioners around their pivots need to be taken in account for what concerns automotive engine front end accessory drives.

In most of the studies about both belt and pulleys dynamics of belt drive systems neither the shear nor the creep between belt and pulleys, that were described in the previous chapter, are taken into account. Only few attempts have been done in this direction. In this chapter an overview of the dynamics analysis of belt drive systems is shown. The belt and the pulleys dynamics, the coupling of the two and the dynamics of automotive belt tensioners are described in the following.

In [61] and [62], Abrate and Zhang offered a complete literature review on this topics, tracing the guidelines that will be followed hereby. The author suggests the interested reader to refer to such literature reviews for a thorough understanding of the topic. This chapter represents the basis for the dynamic analysis of automotive belt drive systems performed in this thesis and for the assumptions that were done for the dynamic models that were used for simulation and that will be described in the next chapter.

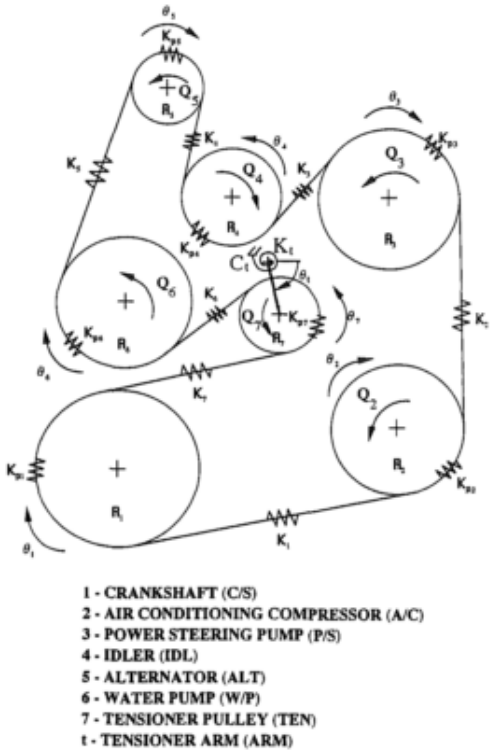

Fig. 4.1 Dynamic Model of an Automotive Serpentine Belt Accessory Drive System [67].

4.1 Pulleys Dynamics

The state of the art of the literature referring to the analysis of the dynamic rotational response of belt transmission drive systems is dense and structured. A well established theory and system definition were developed at the end of the 20th century. Gasper and Hawker at first studied the rotational vibrations of the pulleys in the analysis of free and forced responses without considering the effect of belt tensioners on either the equilibrium state or the dynamic response [63, 64]. Subsequently, in [65–68] the equations of motion of automotive belt drive systems have been developed considering the geometric characteristics of the serpentine drive, the belt spans as coupling springs and the tensioner's effect. The coupling between the transverse motion of the belt and that of the tensioner was the focus of Ulsoy et al. in [69] that highlighted the belt tension fluctuations that can be induced by the tensioner motion.
In Fig. 4.1 a typical automotive serpentine belt accessory drive system is shown as viewed from the front of the engine in [67]. The conventional notation of BDS is

used where the crankshaft pulley is indicated as pulley number 1 and all the other pulleys and the belt spans are subsequently enumerated in a counter-clockwise order. The crankshaft pulley rotates clockwise and is connected through a single belt to accessory pulleys, driven through the "inside" ribbed side on the belt, and to tensioner and idler pulleys on the smooth "back-side" of the belt where no power transfer happens. In Fig. 4.1, according to the conventional notation of BDS the angular coordinates θ_i, $(i = 1,2,...,7)$ define the rotation of each pulley. Positive rotations are consistent with the direction of belt travel when the crankshaft rotates in the clockwise direction. The angular coordinate θ_t defines the tensioner arm angle. The quantities, R_i and C_i, $(i = 1,2,...,7)$ describe the radii and applied external torques for each pulley. Tensioner arm stiffness and damping parameters are represented by K and d_t, respectively. The stiffnesses of the belt for each free span and arc of contact are prescribed by the linear spring constants K_j and K_{pi} $(i = 1,2,...,7)$, respectively. Assuming that the belt stretches in a quasi-static manner, the stiffness values are determined by dividing the tensile modulus by the length of each belt portion. The length of the free spans and contact arcs are calculated knowing the position and radius of each pulley and the pivot of the tensioner arm.
According to Hwang [67], some simple assumptions can be made to model the rotational response of all the pulleys induced by belt stretching when the system is moved by the driving pulley:

- The belt does not slip on the pulleys.
- The belt is uniform, perfectly flexible, and stretches in a quasi-static manner.
- Lateral belt response decouples from longitudinal belt response.
- The crankshaft motion and any torque inputs from accessories are prescribed (either zero or determined from experiments).
- The tensioner executes small motions about some steady-state position. Moreover the tensioner mechanism is designed to be dissipative and is the dominant source of dissipation. The dissipation is assumed to be linear viscous damping, and dissipation in the belt and fixed pulleys is assumed to be negligible small.

Under these assumptions, the equations of motions for a fixed center pulley of inertia J_i result as:

$$J_i\ddot{\theta}_i = R_i(T_{i-1} - T_i) - C_i, i = 2,3,...6 \tag{4.1}$$

where the bearing damping coefficient d_i can be additionally taken into account obtaining:

$$J_i\ddot{\theta}_i + d_i\dot{\theta}_i = R_i(T_{i-1} - T_i) - C_i, i = 2,3,...6 \tag{4.2}$$

The angular velocity of the tensioner arm can be calculated as:

$$J_t\ddot{\theta}_t + d_t\dot{\theta}_t + K_t(\theta_t - \theta_0) = M_t \tag{4.3}$$

where M_t corresponds to the resultant moment applied at the tensioner arm around the pivot caused by the tensions of the two adjacent belt spans, which is highly dependant on the layout of the FEAD. As highlighted by [67, 70], it is also possible to take into account the effect of the gravity g on the tensioner arm using $M_G = m_{eff}L_{eff}g\cos\theta_t$, where m_{eff} is the total mass of the tensioner arm and pulley, L_{eff} is the distance between the pivot and the mass center of tensioner arm and pulley.
M_t can be expressed as function of the layout geometry by referring to the angles on contact between belt spans and pulleys (as was done in [67, 70]) or to the corresponding tangent points, as was suggested by Feng et al. in [71]. The formulation proposed in [71] allows the highest generalization in the formulation of the tensioner arms equation of motion and can be used to model multiple-automatic tensioner systems.
In Fig. 4.2, the rotational modes for the case of engine idle ($477.5rpm$) are illustrated as it was shown in [67]. The solid curves depict the equilibrium configuration, and the dashed curves depict the relative pulley and tensioner vibration amplitudes. The fundamental mode involves in-phase rotations of all pulleys and the tensioner arm. The second, third, and fourth modes involve significant rotations of the tensioner arm, and the phases of rotations for the pulleys are no longer uniform. This analysis can be used to identify those modes, and hence critical excitation frequencies, which may induce significant vibration of the tensioner arm.

4.2 Belt Dynamics and Belt-Pulleys Interface

As has been seen so far, traditionally the rotational vibrations analysis of Belt Drive Systems includes the belt spans influence only as coupling axial springs that determine the tension variation over the spans. In the last twenty years the model of belt drive systems were further developed and improved in order to take into account

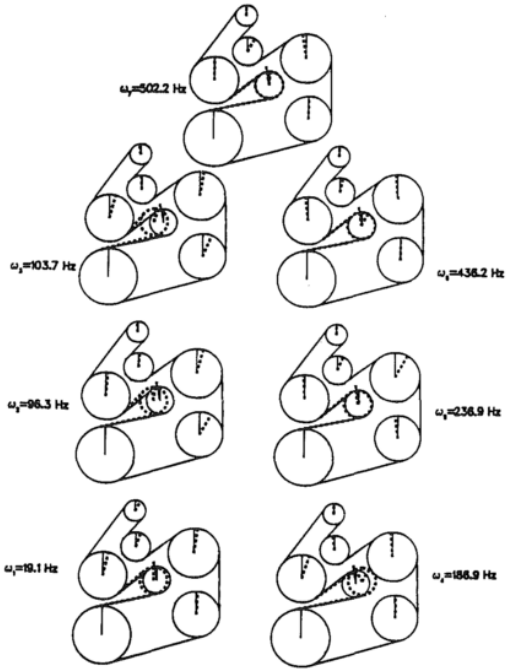

Fig. 4.2 Rotational modes for engine idle, [67].

the influences of the transverse vibrations of the belts on the rotational dynamics and those of the contact interface mechanics between belt and pulleys. This section addresses to the description of the different approaches that were proposed by the authors, considering lumped parameters, hybrid, or finite element models.

4.2.1 Lumped Parameters Models

Tonoli et al. chose to focus on the modelling of the belt-pulley contact with a lumped parameters approach in [50]. The aim of the study was the investigation of the effects of the shear deflection on the rotational dynamics of automotive belt drive systems, that was performed by expanding the Firbank's shear theory to the case of vibrating systems. This approach highlights the study on a particular effect by keeping the model the simplest possible from other points of view and allowing a fast and effective calculation.
An insight on this theory was provided in Chapter 2 and will be expanded in the

following so no further details are provided hereby.

4.2.2 Hybrid Models

In order to take into account the influence ot the transverse vibrations of the belt on the rotational motion of the pulleys, the authors resorted to the theory of continuum systems. The lumped parameters model of the pulleys system was integrated with a model of the belt in the form of a moving string or a moving beam resulting in a hybrid continuous/discrete system which is able to better capture the different characteristics of the motion.
The main issue with an approach based on the theory of the continuum systems is that it requires solving equations depending on the boundary conditions and often need iteration loops for determining the eigensolutions. This can lead to high computation times in the case of the complex serpentine layouts that are usually used in automotive applications.

Moving strings

Theory of the moving strings ([72–77]) describing the transverse dynamics of the belt was adopted in [60, 67, 78–80] to study the dynamic response of serpentine belt drives and to investigate the coupling between the flexural motion of the belt and the rotational vibration of the pulleys by means of non linear and linearised models to predict the free and forced vibrations.
This theory is based on the results of a research branch that has been very active starting from the 19th century. The topic of the transverse dynamics has been studied since the time when leather or woven flat belts were used for the power transmission in industrial plants and in machines for agriculture. In 1897, Skutch addressed the problem of small lateral oscillations of an undamped string which travels under constant tension and at constant speed and calculated the natural frequencies of the system by superimposition of two waves moving in opposite directions [72]. Later on, Archibald and Emslie [73] considered the same problem but derived the equations using a variational approach.
The approach proposed by [72] and [73] was not suitable to discuss the behaviour of

a string under a sinusoidally alternating influence or to include the effect of damping. Sack ([74]) analysed the dynamic behaviour of transverse standing waves for travelling strings and compared it with the one of clamped strings, highlighting the main difference being in the introduction of a phase propagation velocity v'. For what concerns the shape of the envelope, the position of the nodes and the variation of amplitude, the behaviour of travelling and clamped strings were shown to be the same. Sack's theory on the dynamics of axially moving continua was supported and expanded in several works during the subsequent years, [75–77, 81–85]).

Moving beams

The representation of a belt through the moving strings theory was not able to capture the effects of the belt bending stiffness on the natural frequencies and the contribution of the bending torque on the belt-pulley contact. Modelling the belt as a moving beam shows that transverse vibration of every span is linearly coupled with the rotations of the two adjacent pulleys at its ends, [86, 87]. Parker and Kong highlighted the influence of the bending stiffness on the power efficiency of the transmission by affecting the belt departure points from the pulleys and consequently the corresponding wrap angles, span lengths and tension distribution that resulted to be not uniform differently from what was assumed through a moving strings modelling approach [88]. Fig. 4.3 shows the influence of the variation of the belt bending stiffness on the wrap angles and on the maximum transmittable torque on the smallest pulley. The developed model was then used in [89] to represent a real automotive front end accessory drive including the effects of a belt tensioner. The work showed how the belt bending stiffness influences the variation of the belt tensioner orientation angle in different operating conditions of the transmission, affecting the tensioner's effective functioning and the system's overall power efficiency.

4.2.3 Finite Element Models

The Finite Elements (FE) approach already introduced in ([90–93]) may be an alternative to the above mentioned methods. Leamy and Wasfy in [90, 91] attempted to include a belt-pulley contact model into their rotational dynamic study developing

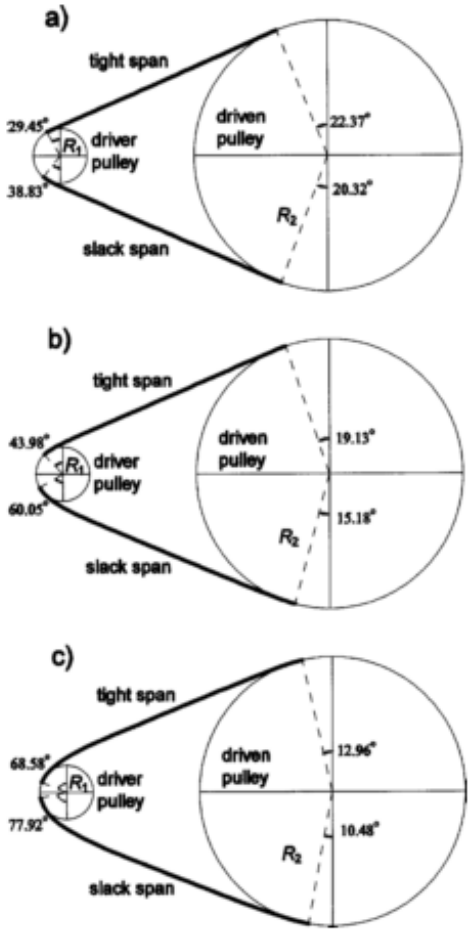

Fig. 4.3 Influence of belt bending stiffness on transmission efficiency. [88].

a finite element model of the belt drive system including a belt pulley frictional model.

The expressed goal of Leamy and Wasfy's work in [90] was to bridge the gap between the belt-drive mechanics studies and the serpentine belt-drive dynamic response studies. The proposed model features standard truss elements to represent the belt, while the pulleys are modelled as rotating circular constraints, for which the driver pulley's angular velocity is prescribed. The frictional contact between the pulleys and the belt is modelled using a penalty formulation with frictional contact governed by Coulomb-like tri-linear friction law. As it is shown in Fig. 4.4, by an appropriate choice of a friction profile parameter v_s , such a tri-linear friction law can be made to satisfactorily approach a Coulomb friction law. The finite element

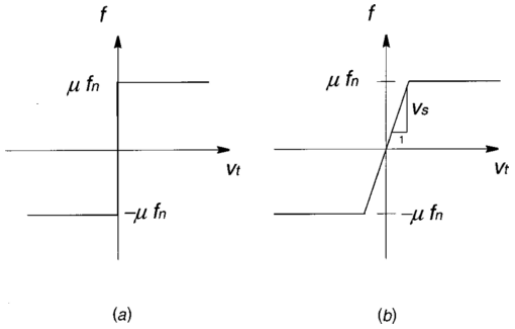

Fig. 4.4 Friction laws:(a) Coulomb law, (b) tri-linear creep-rate dependent law. Here,f denotes the friction force per unit length and f_n denotes the normal force per unit length between two contacting bodies, v_t denotes the tangential velocity difference, and μ denotes the Coulomb friction coefficient [67].

solution was eventually validated by comparison with an exact analytical dynamic solution of a two-pulley belt-drive developed by Leamy and Wasfy in "Analysis of Belt-Drive Mechanics Using a Creep-Rate Dependent Friction Law". An excellent agreement was found for what concerns the normal and tangential force distributions between the belt and the pulleys, the driven-pulley angular velocity and the belt span tensions.

4.2.4 Multibody Models

The multibody approach was proposed for the representation of belt drive systems by Lin et al. in [94]. The model was developed with the software ADAMS and it included a representation of the belt discretized in lumped rigid elements with inertia properties connected to each other by pure elastic joints with axial and bending stiffness. They both could translate at a certain speed U.
A multibody approach was followed also by Cepon et al. for the model developed in [95]. The model used the absolute nodal coordinate formulation (ANCF) and formulated the belt pulley contact forces as a linear complementary problem (LCP) which incorporated the discontinuous Coulomb friction law. The methodology for the parameters identification was additionally presented for what concerns both the belt characteristics ([96]) and the contact behaviour ([97]). The same model was eventually validated in [98].
The multibody approach allows to easily cope with complex layouts at the cost

of being strictly linked to time domain simulations so that the frequency domain analysis can be performed only indirectly on the obtained time-domain data. This is time consuming and in many cases non sustainable.
An example of multibody modelling approach is also provided by the commercial software SimDrive 3D, by the German company Contecs, that is specialized in power transmission systems. Such software provides analysis in both time and frequency domain and performs analysis of belt flapping, slippage and power losses. A particular attention is given to the belt parameters identification and to belt lifetime prediction.

4.3 Chapter Conclusions and Remarks

This Chapter provided an overview about the different modelling approaches that can be used to represent belt drive systems. Each approach has different advantages and characteristics depending on which aspects of the transmission are meant to be highlighted and which working conditions are object of study. In the context of the present thesis two modelling approaches were used to represent the dynamic behaviour of one of the BDS layouts that were experimentally investigated. A custom lumped parameters model was built by the author and then validated by means of comparison with both the dynamic model obtained with the commercial software SimDrive and the experimental measurements obtained on a dedicated test rig.

Chapter 5

System Modelling

In this Chapter the modelling activity that the author carried out is described. Both the static and dynamic behaviour of belt drive systems are addressed.
The static behaviour of two BSG-based BDS layouts is studied by means of an analytical model. The case of an omega twin arm tensioner and an alpha twin arm tensioner have been addressed and compared.
For what concerns the dynamic analysis, a MATLAB-Simulink® tool was developed for the modelling of different front end accessory drives. Its characteristics are presented in this Chapter, starting from the assumptions that support the modelling and the overall architecture of the model. The single subsystems are described individually and then assembled to show the complete model of a traditional automatic tensioner BDS layout. Additionally,the same layout is modelled by means of a commercial multi-body 3D software in order to compare the simulation results on the two models.
In the following chapters, a comparison between simulation results and experimental measurements will be shown considering each modelling solution proposed hereby. This process will lead to a validation of the modelling approach presented in this Chapter.

5.1 Static Model of a Twin Arm Tensioner

An omega twin arm tensioner is a passive device composed by two pulleys connected by a torsional spring and rotating around a pivot that is coaxial relative to the BSG

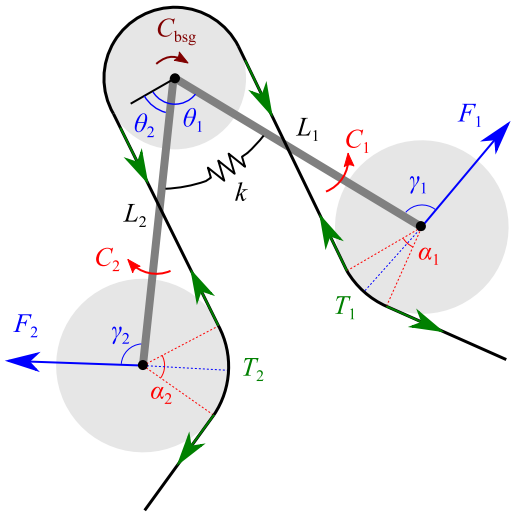

Fig. 5.1 Scheme of the omega twin arm tensioner with variables and parameters of interest: belt tension T_i, arm force F_i, pulley wrap angle α_i, force angle γ_i, arm torque C_i, arm angle θ_i, arm length L_i, tensioner spring stiffness k_t, BSG torque C_{bsg}, where the arm angles θ_i are defined in the reference system given by the bisector of the wrap angle and its perpendicular axis centered on the tensioner pivot.

axis. In an alpha twin arm tensioner the two pulleys rotate together around the BSG axis due to a damping mechanism that is frictionally engaged to the carrier and have an additional relative motion as only one of the two pulleys rotates around a second axis governed by the action of a spring.

A common modelling approach is proposed for both the omega and alpha twin arm tensioners that were investigated in this research activity. The two tensioner pulleys move around the common pivot, i.e. the BSG axis: this motion depends on the resulting hub loads and the spring torque of the tensioner, in the case of the omega tensioner the spring torque will directly influence the movements of both the pulleys while in the case of the alpha tensioner its contribution will affect only one of them. The described system can lead to variations in the absolute position of the arms and their relative aperture. Furthermore, the hub loads on the two tensioner axes depend on the geometry of the system. Specifically, the pulley wrap angles define the arm forces and hence, the torque that arises around the tensioner pivot.

In this section, an analytical representation of the behaviour of the twin arm tensioner is conducted by taking into account static equilibrium and geometry constraints. To this end, the following hypotheses must be adopted:

- The tensioner arms are considered infinitely rigid.

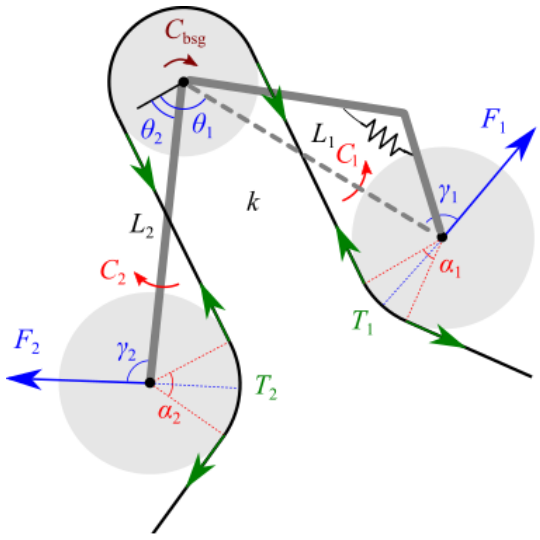

Fig. 5.2 Scheme of the alpha twin arm tensioner with variables and parameters of interest: belt tension T_i, arm force F_i, pulley wrap angle α_i, force angle γ_i, arm torque C_i, arm angle θ_i, arm length L_i, tensioner spring stiffness k_t, BSG torque C_{bsg}. Compared to the omega twin arm tensioner, in this case while the arm L_2 has a constant length, the first arm L_1 will depend both on the length of the two arms a, connecting the BSG axis to the movable tensioner pivot, and b, which is the arm of the movable tensioner, and on the angular displacement ι of the spring that connects them

- The tensioner arms are considered perfectly hinged on their supports, where friction effects are neglected.
- The friction of the bearings of the pulleys is neglected.
- The tensioner spring acts with no friction and perpendicularly to the axis of each tensioner pulley.
- The belt is considered ideal, i.e. without energy dissipation and infinitely rigid.

Figure 5.1 highlights the main variables and parameters to consider for the static analysis of the omega twin arm tensioner. The subsequent analytical description can be provided for both tensioner pulleys using the indexes $i = 1,2$.
Following the initial assumptions, the torques acting on the tensioner pivot balance each other in static equilibrium, i.e.

$$C_1 = C_2, \tag{5.1}$$

and

$$C_i = F_i L_i \sin \gamma_i, \tag{5.2}$$

where F_i is the hub load measured on the pulley axis, L_i is the length of each tensioner arm and γ_i is the angle between the applied force and the corresponding lever arm. Furthermore, the applied force on each arm depends on the tension of the belt span T_i and the wrap angle α_i:

$$F_i = 2T_i \sin\left(\frac{\alpha_i}{2}\right). \tag{5.3}$$

In the case of the omega twin arm tensioner, the established assumptions let the tensioner spring transmit the torque ideally from one arm to the other, and hence C_i is defined by the tensioner stiffness and relative displacement of the two tensioner pulleys:

$$C_i = k_t(\theta_v - \theta_u - \Delta\theta_0), \tag{5.4}$$

where k_t denotes the spring stiffness, $\Delta\theta_0 = \Delta\theta(0)$ is the angular aperture at null torque and θ_u and θ_v denote the angular displacement of the tensioner arms with respect to the reference system given by the bisector of the wrap angle and its perpendicular axis centered on the tensioner pivot. The indexes u and v assume different values according to the operating mode:

- *Motor mode:* the BSG exerts electric traction.

$$\begin{cases} v &= 1 \\ u &= 2 \end{cases}$$

- *Generator mode:* the BSG functions as an alternator.

$$\begin{cases} v &= 2 \\ u &= 1 \end{cases}$$

In the case of an alpha twin arm tensioner, the situation changes as the spring acts only on one of the two tensioner arms as it can be seen in Fig. 5.2. While the arm L_2 has a constant length, the first arm L_1 will depend both on the length of the two arms a, connecting the BSG axis to the movable tensioner pivot, and b, which is the

arm of the movable tensioner, and on the angular displacement ι of the spring that connects them:

$$L_1 = sqrt(a^2 + b^2 - 2ab\cos(\iota)), \tag{5.5}$$

with

$$\iota = \frac{C_t}{k_t} + \iota_0 \tag{5.6}$$

where C_s and k are respectively the tensioner spring torque and stiffness.
Equations 5.1 to 5.4 emphasize the dependence between the angular position of the tensioner arms and the belt tension of both spans. In addition, the difference between the tensions of both belt spans is imposed by the BSG torque

$$C_{\text{bsg}} = R_{\text{bsg}}(T_v - T_u), \tag{5.7}$$

where R_{bsg} is the radius of the BSG pulley. If the BSG is not applying torque on the belt, the tensions T_u and T_v are equal to the pretension of the belt T_0. When the BSG acts on the system, $T_v > T_u$, where the indexes u and v are selected according to the working mode, as previously indicated.
To fully define the static model, the total length of the belt L_{tot} is constrained to its nominal value:

$$L_{\text{tot}} = L_{\text{nom}}. \tag{5.8}$$

The solution of the static model described through Eqs. 5.1 to 5.8 requires the full geometry of the transmission. Hence, the analytical formulation of contact points, wrap angles and belt span lengths is provided in the following.

Layout Geometry

In a serpentine belt drive system, the belt wraps around the pulleys in both forward and backward directions. Therefore, four configurations between the belt and adjacent pulleys are possible: two direct and two crossed (see Fig. 5.3). For each possible

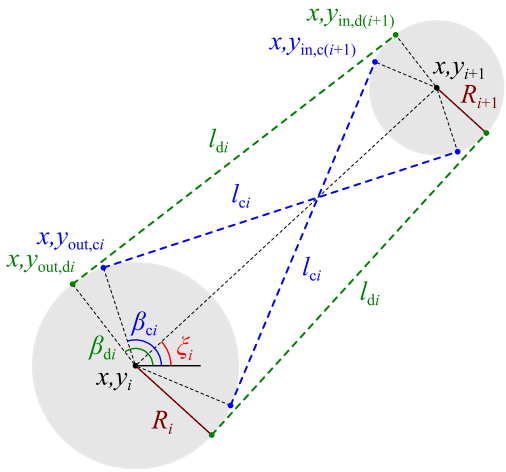

Fig. 5.3 Geometry of the connection between two adjacent pulleys.

configuration, the contact points at the entry or exit of the pulley are described by

$$x_{p,ti} = x_i + R_i \cos(\xi_i \pm \beta_{tj}) \tag{5.9}$$

$$y_{p,ti} = y_i + R_i \sin(\xi_i \pm \beta_{tj}) \tag{5.10}$$

where x_i, y_i are the Cartesian coordinates of the pulley center and R_i is the pulley radius. The angle between the horizontal and the line connecting the centers of the ith and jth pulleys is indicated as ξ_i, while β_{tj} is the angle between the horizontal and the belt span itself. The index p indicates the nature of the contact point, whether it corresponds to the entry ($p = \text{in}$) or the exit ($p = \text{out}$) of the belt on the pulley. The index t indicates the belt span type, whether it is crossed ($t = \text{c}$) or direct ($t = \text{d}$). Note that the position of a generic tensioner pulley with respect to the pivot point is dictated by the arm angle θ_i:

$$\begin{cases} x_i &= x_{\text{bsg}} + L_i \cos\theta_i \\ y_i &= y_{\text{bsg}} + L_i \sin\theta_i \end{cases}, \tag{5.11}$$

where, as previously described, the pivot of the tensioner arms is placed on the center of the BSG pulley $x_{\text{bsg}}, y_{\text{bsg}}$.

The length of the belt span is given by the distance between the exit contact point on the ith pulley and the entry contact point on the jth pulley:

$$l_{ti} = \sqrt{\left(x_{\text{in},tj} - x_{\text{out},ti}\right)^2 + \left(y_{\text{in},tj} - y_{\text{out},ti}\right)^2}. \tag{5.12}$$

Also, the wrap angle of the belt on the pulley can be defined as the angular distance between the entry and exit contact points.

$$\alpha_i = 2\arcsin\left[\frac{\sqrt{\left(x_{\text{out},ti} - x_{\text{in},ti}\right)^2 + \left(y_{\text{out},ti} - y_{\text{in},ti}\right)^2}}{2R_i}\right]. \tag{5.13}$$

For a generic pulley of radius R_i, the wrap length is simply

$$l_{\text{w}i} = R_i\alpha_i, \tag{5.14}$$

and hence, the total length of the belt is calculated as the sum of spans and wraps:

$$l_{\text{tot}} = \sum_i (l_{\text{w}i} + l_{ti}). \tag{5.15}$$

Finally, the angle γ_i between the applied forces F_i and the corresponding lever arms L_i can be expressed as

$$\gamma_i = \pi - \frac{\alpha_i}{2} - \arccos\left(\frac{R_{\text{bsg}} + R_i}{L_i}\right) \tag{5.16}$$

The obtained geometric expressions (Eqs. 5.9 to 5.16) can be substituted into the system of equations of the static model (Eqs. 5.1 to 5.8). For solving purposes, the model is initially set with the standstill positions of the pulleys x_{0i}, y_{0i} and the belt pretension T_0. Subsequently, a known BSG torque C_{bsg} is applied and the solution of the static model yields the tension of the belt spans T_i and the angle of the tensioner arms θ_i associated to the given load.
For practical purposes, the equation set was implemented in MATLAB® and solved using a trust-region dogleg nonlinear method.

5.1.1 Simulation Assessment

The solution of the described system of equations for a given BDS layout is shown in Fig. 5.4. The standstill layout ($C_{\text{bsg}} = 0$) is compared to the one obtained with different BSG torque values: 10 and 30 Nm both in motor and generator modes. The plots show the direction of rotation of the crankshaft and the nature of the BSG

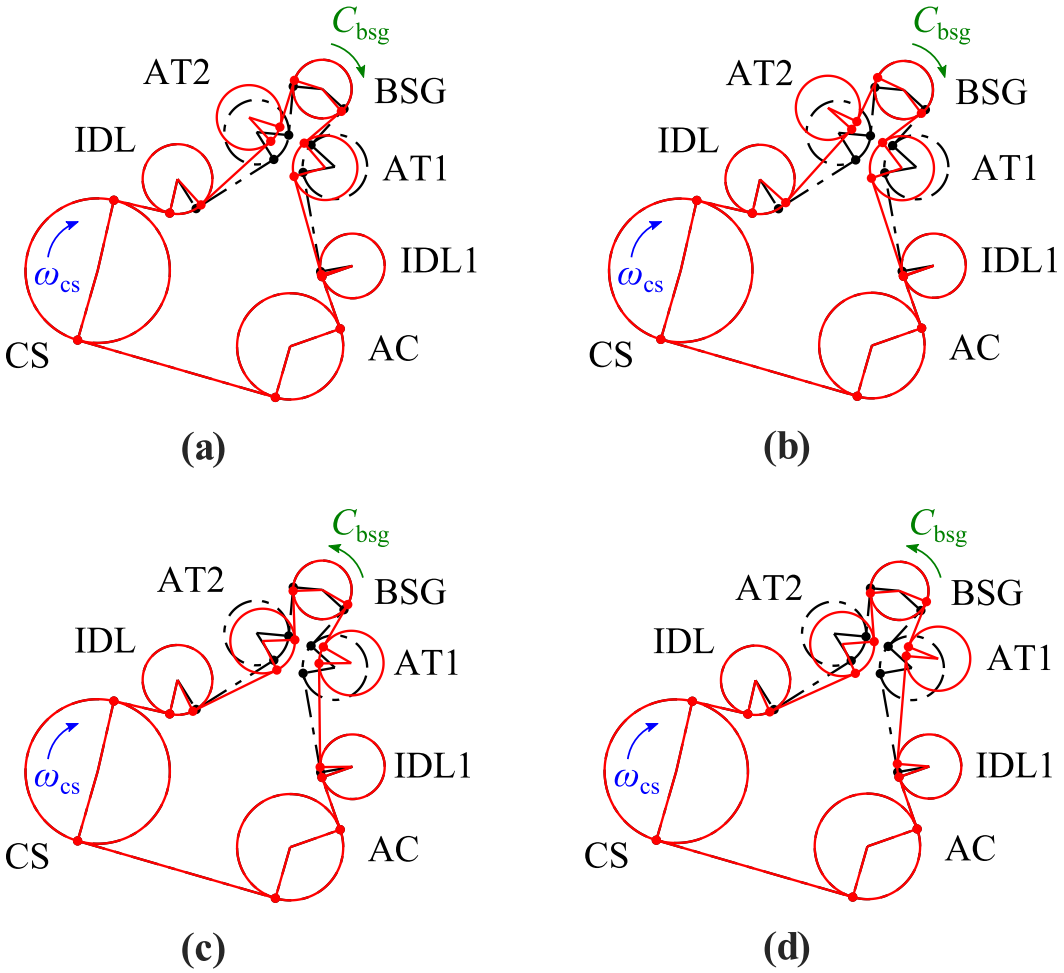

Fig. 5.4 Geometry of a BSG-based BDS equipped with a twin arm tensioner for different operating conditions. Working geometries (solid) are compared with standstill (dashed). The BSG is driven at (a) 10 Nm and (b) 30 Nm in motor mode, and (c) -10 Nm and (b) -30 Nm in generator mode. The layout is constituted by crankshaft (CS), air conditioning compressor (AC), idlers (IDL and IDL1), tensioner pulleys (AT1 and AT2) and BSG. The directions of the crankshaft speed ω_{cs} and the BSG torque C_{bsg} are also indicated.

torque. In motor mode, the BSG torque and the crankshaft speed present the same direction, whereas in generator mode, they are opposite.
Moreover, a variation in C_{bsg} produces a change in the absolute angle of both tensioner arms and the relative aperture among them. Fig. 5.4 also shows the dependence of the tensioner behavior on the geometry of the system. When the tensioner arms move, the wrap angles of the tensioner and the adjacent pulleys change. Consequently, the length and position of the belt spans are also modified.
Table 5.1 lists the performance data corresponding to each condition addressed in

Table 5.1 Simulation results on the performances of a BSG-based BDS system using a twin arm tensioner.

condition	BSG mode	BSG torque [Nm]	tight span tension [N]	slack span tension [N]	BSG sliding arc [%]	BSG wrap angle [deg]
(a)	motor	10	603.5	250.5	19.8	212
(b)	motor	30	1307.6	247.7	38.2	207.6
(c)	generator	−10	600.9	247.7	19.9	212
(d)	generator	−30	1317.7	257.8	37.8	206

Table 5.2 Simulation results on the performances of a BSG-based BDS system using a traditional tensioner.

condition	BSG mode	BSG torque [Nm]	tight span tension [N]	slack span tension [N]	BSG sliding arc [%]	BSG wrap angle [deg]
(a)	motor	10	450.1	49.6	55	191.2
(b)	generator	−10	568.2	247.7	17.7	223.5

Fig. 5.4 for a pretension of $T_0 = 288$ N and a starting position of $\theta_1 = 75.7^\circ$ and $\theta_2 = 141.7^\circ$. The output data are the belt tension on both the tight and the slack spans, the wrap angle and the sliding arc on the BSG pulley. This latter quantity is defined according to Euler's formula

$$\phi_{\text{s}} = \frac{1}{\mu_{\text{r}}} \ln\left(\frac{T_v}{T_u}\right), \tag{5.17}$$

and the equivalent friction coefficient is given by

$$\mu_{\text{r}} = \frac{\mu}{\sin(\nu/2)} = 1.2, \tag{5.18}$$

where μ is the static friction coefficient and ν is the pulley rib angle.
In Table 5.1, the sliding arc is indicated as a percentage of the wrap angle to better

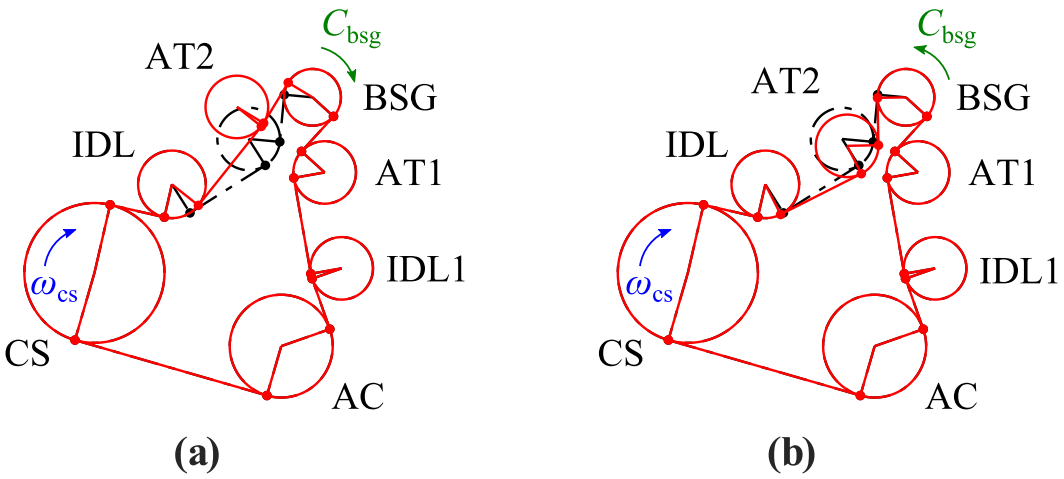

Fig. 5.5 Geometry of a BSG-based BDS equipped with a traditional tensioner for different operating conditions. Working geometries (solid) are compared with standstill (dashed). The BSG is driven at (a) 10 Nm in motor mode and (b) -10 Nm in generator mode. The layout is constituted by crankshaft (CS), air conditioning compressor (AC), idlers (IDL and IDL2), tensioner pulleys (AT1 and AT2) and BSG. The directions of the crankshaft speed ω_{cs} and the BSG torque C_{bsg} are also indicated.

highlight its influence on the performance of the transmission.

Results demonstrate that a twin arm tensioner yields relative sliding arcs below 40% of the wrap angle for the calculated conditions. This means that a total slip situation is never reached, even with very high torque requests from the BSG. In addition, the tension of the slack span is kept at around 85% of the belt pretension; it stays well within a tension gap that guarantees a proper transmission efficiency and avoids excessive belt slip. It is worth mentioning that these outcomes are obtained for both motor and generator working modes.

To highlight the advantages of the twin arm solution over a traditional tensioner, Fig. 5.5 shows the behavior of a BDS equipped with this latter device. A BSG torque of 10 Nm is applied in both motor and generator modes. The corresponding performance data are reported in Table 5.2.

The performance drop in motor mode is evident with the traditional tensioner. The tension of the slack span dramatically decreases and the sliding arc results above 50% of the whole wrap angle. Moreover, it was not possible to obtain feasible results at $C_{bsg} = 30$ Nm, as this case would lead to a total slip condition where the tensioner pulley and the belt lose contact. The obtained results indicate that the traditional tensioner is inadequate to operate in BSG-equipped BDSs, mainly due to its inability to adapt to the exchange between tight and slack spans.

The modelling process when addressing a traditional tensioner was done by fixing the position of one of the two tensioner pulleys of the considered layout: in order to put the one-arm tensioner on its traditional position on the slack span for generator mode, the pulley on the AC compressor side was fixed. Additionally, the belt length constraint (Eq. 5.8) does not hold any more because belt deformation is mandatory to allow the motion of the single-arm tensioner. To overcome this issue, the belt was assumed extensible inside a range of $\pm 0.7\%$ of its nominal length.
The results obtained by such simulation will be compared with experimental results in Chapter 7.

5.2 Discrete Dynamic Model

A modular modelling approach was defined in the present thesis. Using the MATLAB-Simulink® environment, the subsystems of a front end accessory drive were modelled separately in order to obtain a series of modules available to be used to assemble different BDS configurations.
In particular the blocks for the serpentine belt, a driving pulley, a driven pulley characterised by power transfer, an idler pulley and a tensioner pulley were built. The dynamic models of different front end accessory drive layouts were then obtained by properly assembling the available blocks.

5.2.1 Assumptions

The assumptions that were adopted at the base of the modelling of the dynamics of a belt drive system are the same that were enunciated in [50]. The goal of such assumptions is the reduction of the complexity of the dynamic model while trying to preserve the dynamic effects that are affected by the shear deformation whose effects were chosen to be used to represent the dynamics behaviour. They are enunciated in the following for sake of completeness.
The assumptions considered for the belt-pulley interface were already listed in Chapter 2.
For what concerns the free spans, it is assumed that:

- Finite stiffness in the axial direction and negligible bending stiffness.

- Negligible mass per unit length. The effects on the transmission due to the flexural dynamic behaviour of the belt are neglected. The longitudinal dynamic behaviour of the free spans is neglected.
- The dissipation is modelled as viscous damping. The viscous damping coefficient is computed to be equivalent to the complex stiffness at the resonant frequency that mainly involves the axial deformation of the belt [99].

The assumptions concerning the pulleys are the following:

- All the pulleys are modelled in terms of lumped rotational masses, torsional springs and dampers.
- The axis of the motor and of the alternator pulleys are fixed and the radial deformations of the pulleys are negligible.
- All the dissipative effects in the pulleys are modelled in terms of linear viscous dampers. This is an approximation as the damping in a transmission system is mainly given by hysteretic dissipations in the rubber rings included in the pulleys and in the friction about the tensioner pivot. The combination of the elastic forces, geometrical non-linearities and friction forces and torques make the mechanical characteristic of automatic tensioners highly non-linear and affected by a wide hysteresis cycles. Even if such non-linearities cannot be neglected for wide amplitude motions, a linear model is adopted in the present case to obtain a first approximation model.

Additional assumptions were made for the modelling of the belt tensioners. A highlight on these assumptions is provided in the dedicated section and different cases are addressed and described.

5.2.2 Contact Interfaces and Losses

Fig. 5.6 shows the lumped parameters model adopted for the belt. It is the scheme proposed by [50] where a 3 pulleys belt drive system was considered, composed by driving and driven pulley together with a belt tensioner. As highlighted by the assumptions made in the previous sections, the arcs of contact of the V-ribbed pulleys are characterized by the model of the shear deformation that affects the belt ribs. In

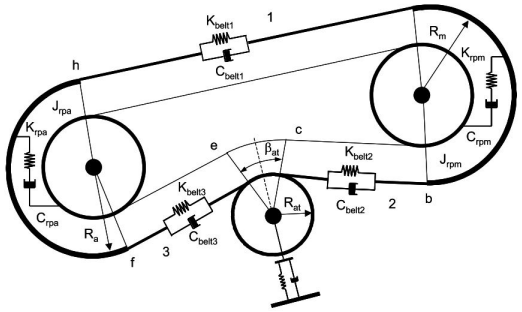

Fig. 5.6 Lumped parameters model of the belt in a 3 pulleys transmission [50].

presence of a shear deformation, a rotational inertia is computed for each V-ribbed pulley, considering the mass of the arc of contact of the belt at the radius R_i of the tension member:

$$J_{bi} = \rho_{lt}\alpha_i R_i^3 \tag{5.19}$$

where ρ_l is the mass per unit length of the belt.
The shear interaction between the belt and the pulleys is modelled as the series of springs of stiffnesses K_{bi} and viscous dampers of coefficients d_{bi}. The presence of the viscous damper d_{bi} affects the torque transmission from one pulley to the other and implies a certain amount of slip, as predicted by Firbank's model.
The derivation of the stiffness and damping coefficients was performed following the procedure proposed by Tonoli et al. in [50]. From the torque expressed in eq. (3.18) three contributions to the torque were identified

$$C(t) = C_d + C_{k1}(t) + C_{k2}(t) \tag{5.20}$$

where

$$C_d = \tfrac{1}{2}G^*\alpha^2 s \tag{5.21}$$

$$C_{k1}(t) = G^*\alpha\frac{\delta\omega_p}{\omega}\sin\omega t \tag{5.22}$$

$$C_{k2}(t) = 2G^*\frac{\omega_{b0}}{\omega}\sin\left(\omega\frac{\alpha}{2\omega_{b0}}\right)\frac{\delta\omega_p}{\omega}\sin\omega\left(t-\frac{\alpha}{2\omega_{b0}}\right) \tag{5.23}$$

where $G^* = R^3 bG/h$.
[50] highlighted that the three contributions obtained can be interpreted as one viscous contribution which reacts against the mean relative speed, for what concerns C_d, where the viscous coefficient corresponds to $d_{rp} = \frac{1}{2}\frac{G^*\alpha^2}{\omega_{b0}}$; and two elastic contributions, $C_{k1}(t)$ and $C_{k2}(t)$, that react against the torsional rotations about the

mean angular speed, being the first synchronous with the rotations and the second delayed by an amount depending on the time needed to the belt to run about the arc of contact.
It was chosen to neglect the time lagged elastic response and to represent the shear effect as a series of a damper, $C_d = d_{rp}(\omega_{p0} - \omega_{b0})$ and a spring, $C_{k1}(t) = K_{rp}\delta\theta_p(t)$, with torsional stiffness equal to $K_{rp} = G^*\alpha$.

5.2.3 Belt

The belt free spans are modelled as massless springs whose stiffness is computed from the stiffness per unit length c and the length l_i of the free spans:

$$K_{belti} = cl_i \tag{5.24}$$

The associated dissipation is modelled in terms of a viscous damping in parallel to the springs. The damping coefficient d_{belti} is computed as the equivalent damping corresponding to the loss factor η (structural damping) of the belt:

$$d_{belti} = \frac{\eta K_{belti}}{\lambda_{belt}} \tag{5.25}$$

λ_{belt} is the first undamped natural frequency of the transmission related to the axial deformation of the belt. This natural frequency is computed from the linearized model of the transmission by taking the mode whose elastic energy is mainly concentrated in the axial deformation of the belt.

5.2.4 Pulleys

Lumped parameters models of the pulleys have been built to be compatible with the input-output relations of the belt subsystem. A brief description of each model is given in the following subsections considering each type of pulley that can be included in a belt drive system: idler pulleys with a smooth surface where no power exchange happens, V-ribbed pulleys for the driving pulley and the accessories' driven pulleys, and tensioner pulleys where also the tensioner arm behaviour is considered. A non linear model was derived starting from the model developed in [50]. For what the dissipations is concerned, in accordance to the general assumptions 3, a viscous

damping has been adopted throughout the model to allow simulations in the time domain.
For each pulley model a lumped-parameter scheme and the corresponding Simulink® block are provided. A colors' code is used to indicate the different domains considered in the models, that's to say:

- In red are indicated the inputs to the blocks.
- In blue are highlighted the parameters related to the shear deformations of the belt on the contact interface and the outputs related to the tangential motion of the belt on the pulleys
- In magenta the parameters and the outputs related to the angular motion of the pulleys around their axis are represented
- In green is highlighted the coupling between the rotational motion of the pulleys and the corresponding shear deformation on the contact interfaces

Idler Pulleys

In Figs. 5.7 and 5.10 the lumped model of an idler pulley and the corresponding Simulink® scheme are shown. The idler pulleys are usually flat pulleys tangent to the belt on its flat side, so no shear effect is to be considered. The model is very simple, taking into account only the pulley inertia J_{pIDL} and a viscous damping d_{pIDL} that takes into account the small power dissipations that occur in the pulley bearing. The rotational behaviour of an idler pulleys is described by the following equation:

$$J_{pIDL}\dot{\omega}_{bIDL} + d_{pIDL}\omega_{bIDL} = \Delta TR_{pIDL} \tag{5.26}$$

Driving Pulleys

The driving pulley in a front end accessory drive is rigidly connected to the engine crankshaft and it is a ribbed pulley where shear stresses take place. It is often composed of two sections, a hub which serves as interface towards the crankshaft, and, on its outer surface, of a ring with the multi-rib profiles machined to replicate

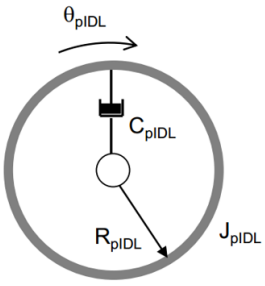

Fig. 5.7 Dynamic model of an idler pulley

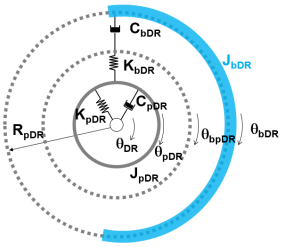

Fig. 5.8 Dynamic model of a ribbed pulley

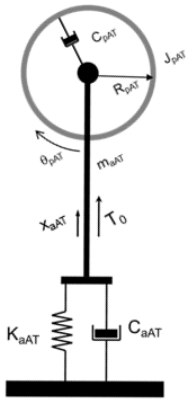

Fig. 5.9 Dynamic model of a tensioner

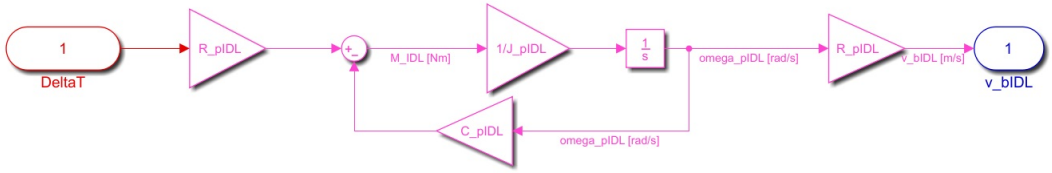

Fig. 5.10 Simulink® model of an idler pulley

the belt geometry. A layer of viscoelastic material assures the torsional connection between them. The inertial, stiffness, and damping parameters of the ring and of the viscoelastic layer are designed so that the pulley operates as a dynamic damper, tuned to the most relevant torsional resonance of the crankshaft. Several configurations have been proposed to dampen and filter out the vibrations coming from the engine compartment via the crankshaft pulley. The lumped parameters model of the crankshaft pulley that was used in this research is represented in Fig. 5.8. Fig. 5.11 shows the corresponding Simulink® model.

The model includes the rotational inertia of the pulley (J_{pdr}) connected to the hub by the parallel of the pulley torsional stiffness K_{pdr} and equivalent viscous damping d_{pdr}. The tangential speed of the belt results from the shear effect present on the pulley-belt interface described by the series of a viscous damping d_{bdr} and the stiffness K_{bdr}. The inputs to the block are the torque applied by the belt given by the tension difference ΔT and the angular speed of the motor shaft ω_{dr} (input of the simulator); the outputs are the tangential speed of the belt, $v_{bdr} = R_{pdr}\omega_{dr}$ and the

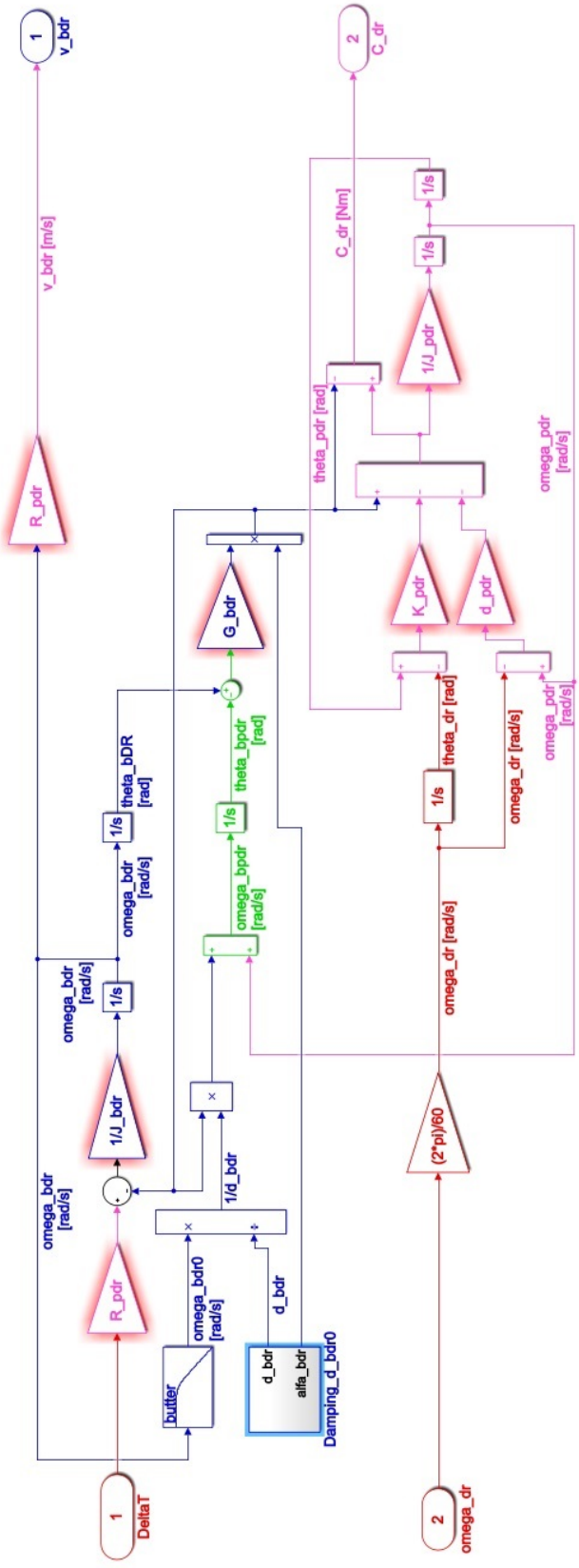

Fig. 5.11 Simulink® model of a driving pulley

resulting torque C_{dr} acting on the crankshaft in response to the given speed.
The equations described in the driving pulley block, as can be clearly seen in the Simulink® model in Fig. 5.11, are the following:

$$J_{bdr}\dot{\omega}_{bdr} + K_{bdr}(\theta_{bdr} - \theta_{bpdr}) = \Delta T R_{pdr} \tag{5.27}$$

$$J_{pdr}\dot{\omega}_{pdr} - d_{bdr}(\omega_{bpdr} - \omega_{pdr}) + K_{pdr}(\theta_p - \theta_{dr}) + d_{pdr}(\omega_{pdr} - \omega_{dr}) = 0 \tag{5.28}$$

$$K_{bdr}(\theta_{bdr} - \theta_{bpdr}) - d_{bdr}(\omega_{bpdr} - \omega_{pdr}) = 0 \tag{5.29}$$

Driven Pulleys with power transfer

The driven pulleys where a power exchange happens are the alternator or BSG pulley and the pulleys attached to the main accessories, such as the AC compressor or the steering wheel. The accessories use V-ribbed pulleys in order to ensure the power transmission and are therefore characterized by a shear deflection. The alternator pulley is usually rigid, it may be either connected to the alternator shaft by means of a rigid shaft or by means of a torsionally compliant element that allows to filter the irregularities coming from the motor. This torsionally compliant element is sometimes called "decoupler", it may include a one way clutch to avoid overloading the tensioner during fast rundowns of the engine.
The lumped parameters model of a driven pulley where a power transfer takes place is the same that was shown for a driving pulley in Figs. 5.8. In this case, the moments of inertia of the accessory and its pulley are J_{DN} and J_{pDN}, respectively. They are connected by a torsional spring with stiffness K_{pDN} and viscous damper with coefficient C_{pDN}. The tangential speed of the belt results is affected by the behaviour of the belt on the pulley-belt interface described by the series of a viscous damping C_{bDN} and the stiffness K_{bDN}.
The inputs in the driven pulley are the torque applied by the belt given by the tension difference ΔT and the torque load defined by the accessory C_{IN}; due to the input given by a torque in this case there is no need to represent in the Simulink® model the pulley stiffness and damping, as it is shown in Fig. 5.12. The corresponding outputs are the tangential speed of the belt v_{bdv} and the resulting torque exerted by the accessory on the system C_{dv}. The equations described in the driven pulley block

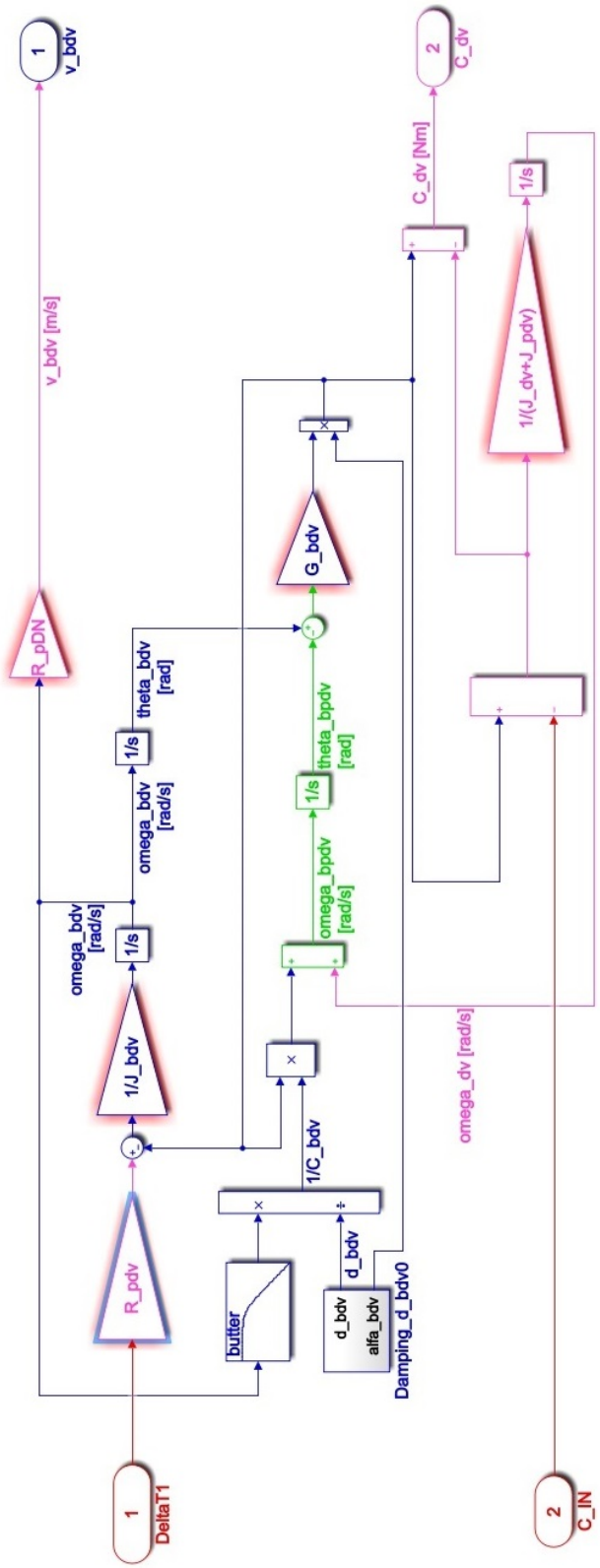

Fig. 5.12 Simulink® model of a driven pulley

slightly differ from those shown in (5.27), (5.28), (5.29) and are the following:

$$J_{bdv}\dot{\omega}_{bdv} + K_{bdv}(\theta_{bdv} - \theta_{bpdv}) = \Delta TR_{pdv} \tag{5.30}$$

$$J_{pdv}\dot{\omega}_{pdv} - d_{bdv}(\omega_{bpdv} - \omega_{pdv}) + C_{IN} = 0 \tag{5.31}$$

$$K_{bdv}(\theta_{bdv} - \theta_{bpdv}) - d_{bdv}(\omega_{bpdv} - \omega_{pdv}) = 0 \tag{5.32}$$

Tensioners

The automatic tensioner (at) of Figs. 5.6 and 5.9 has been modelled under the assumption that its pulley is moving along the bisector of contact arc, indicated as β_{at} in Fig. 5.6, which is assumed to be constant. The nonlinear geometric terms arising from the rotation of the tensioner about its pivot have been therefore neglected. This assumption together with the assumption that the belt has negligible radial compliance allows to decouple the angular motion of the pulley from the linear one. This assumption may be acceptable in the case of an accessory belt drive where the tensioner arm is large compared to the displacement of the pulley during most operating conditions, such as those that occur in steady state far from the idle regime. By converse, the current assumption may not be valid in the case of the very fast transients during engine cold start-up or fast rundowns and at idle when the crankshaft speed irregularities are very large.
The lumped parameters model includes the rotational inertia of the pulley (J_{pt}) and the masses of the arm and of the pulley (m_{at}). They are connected to the ground by the linear spring with stiffness K_{at} and the viscous damper with damping coefficient d_{at}. The very small power dissipations that occur in the bearing of the pulley are accounted for by a viscous damper with coefficient d_{pt}. The inputs in the tensioner are the tensions of the two belt spans adjacent to the tensioner as can be seen in the Simulink® scheme of the block in Fig. 5.13. The pretension of the automatic tensioner arm T_0 is a parameter of the block. The angular speed of the pulley (ω_{pt}) and the linear velocity v_{at} of the spin axis of the automatic tensioner pulley are the outputs of the block.
The resulting equations of the block are the following:

$$J_{pt}\dot{\omega}_{bt} + d_{pt}\omega_{bt} = \Delta TR_{pt} \tag{5.33}$$

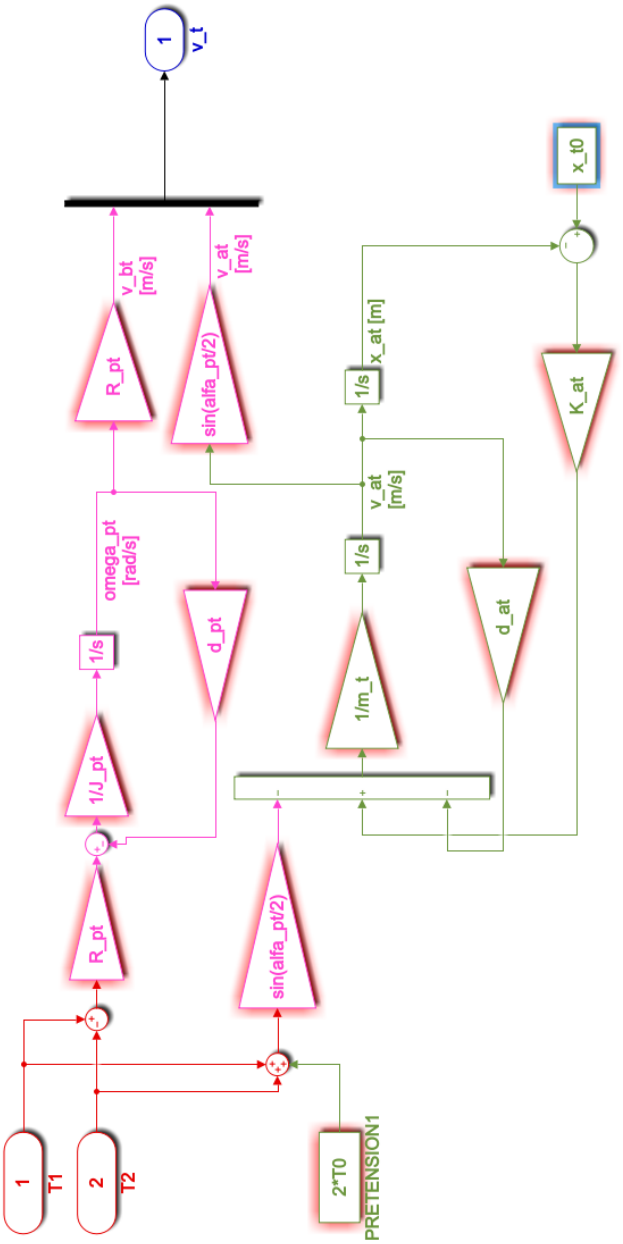

Fig. 5.13 Simulink® model of a traditional automatic tensioner

$$m_{at}\ddot{x}_{at} + d_{at}v_{at} + K_{at}(x_{t0} - x_{at}) = (T_1 + T_2 - 2T_0)\sin\left(\frac{\alpha_{pt}}{2}\right) \tag{5.34}$$

The dynamic analysis performed with this model is intended to be used for steady state conditions, where the variation of the contact arc as function of the displacement of the tensioner can be assumed to be negligible. This assumption allows to neglect the geometry variations for belt spans adjacent to tensioner pulleys consequent to the angular displacements of the tensioner arm.

5.2.5 Simulation Assessment

In [50] the modelling approach presented in this chapter was validated by means of experimental data. A simple drive featuring a driving and a driven pulley and a belt tensioner was modelled, as shown in Fig. 5.6, and compared to the experimental results obtained on a dedicated test rig representing the same layout. In this section a further assessment of the modelling approach is presented and the software SIMDRIVE 3D®, distributed by Contecs GmbH, is used as benchmark by providing a means of comparison. This evaluation was performed in order to show the modelling approach's a priori suitability for a generic drive dynamic behaviour representation. SIMDRIVE 3D® is a general-purpose multibody code with an embedded pre- and post processor which was developed specifically to simulate mechanical systems composed of multiple rigid and flexible components. SIMDRIVE 3D® can be considered nowadays the simulation standard mostly used in the automotive industry to perform a predictive dynamic analysis of the whole power transmission systems in time and frequency domain. It includes different modules, among which: Poly-V drives, timing belt drives, crankshaft vibrations, fly-wheel dynamics.
The Poly-V drives tool allows to compose multi-pulley serpentine drives by setting the characteristics of the different components. Through a Graphic User Interface it is possible to insert the geometric characteristics of the layout, the rheological characteristics of the drive and the belt parameters, including the friction coefficients on each pulley.
Fig. 5.14 shows the simple belt drive model that was used as first simulation mean of comparison between the two modelling approaches. Fig. 5.14 allows to identify the basic elements that were used to build the model and highlights the usability of the graphic interface that allows to build a model with SIMDRIVE 3D® with a simple drag and drop operation.
The model in Fig. 5.14 features a driving pulley, a driven pulley and an idler, con-

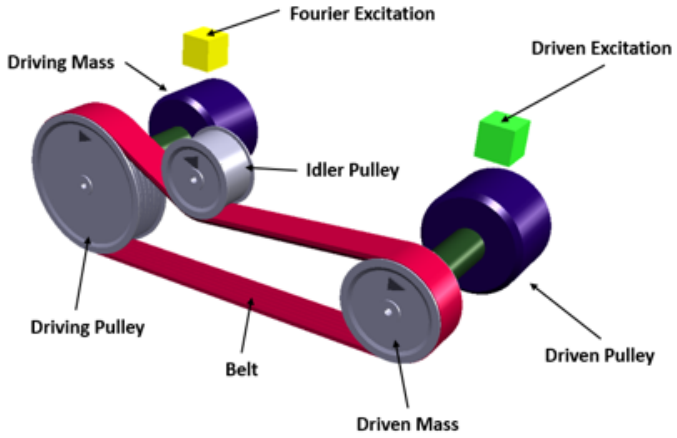

Fig. 5.14 SIMDRIVE 3D® model of the 2 pulleys layout.

nected by means of a V-ribbed belt. In the pulley elements the position, the radius and the rotational inertia of each pulley need to be inserted. The two pulleys that are characterized by a power exchange need to be connected to a mass element through an axial connector. The axial connector has no physical meaning but is only used to realize the connection and in some cases it is also the place where a rheological element can be inserted (stiffness, damping, friction). The masses connected to the pulleys require the setting of the element's rotational inertia. In the case of the CS mass we use hereby a fictitious inertia of $1 kgm^2$ that has no physical meaning. The belt element requires the setting of all the belt characteristics: number of ribs, longitudinal stiffness, radial stiffness, etc. In table 5.3 all the parameters that were set in the model are shown. The forth column of table 5.3 also shows the corresponding parameter of the model of the same drive built in Simulink® environment by following the indications provided in the previous sections of this chapter. The corresponding Simulink® model is shown in Fig. 5.15, where the blocks "IDLER", "DRIVING PULLEY" and "DRIVEN PULLEY" are described by Figs 5.10, 5.11 and 5.12, respectively, and in the block "Belt" are implemented eqs. 5.24 and 5.25. The MATLAB-Simulink® model is composed by the block diagram in 5.15 together with a preprocessing script where the geometry of the layout is assessed using the same formulations described in paragraph 5.1. This script needs to be run previous to the dynamic simulation in order to define the values of geometric parameters such as: length of the belt spans, pulleys wrap angles,tensioner differential angles.

SIMDRIVE 3D® gives the chance of applying the input excitations in different

Table 5.3 Simulation results on the performances of a BSG-based BDS system using a twin arm tensioner.

SIMDRIVE 3D® element	parameter	value	Simulink® parameter
Driving pulley	coordinates	$(0,0)$mm	(x_{pdr}, y_{pdr})
	diameter	80mm	R_{pdr}
	rotational inertia	$2e-4$kgm^2	J_{pdr}
Driven pulley	coordinates	$(200,0)$mm	(x_{pdv}, y_{pdv})
	diameter	50mm	R_{pdv}
	rotational inertia	$1e-4$kgm^2	J_{pdv}
Idler pulley	coordinates	$(80,30)$mm	(x_{pIDL}, y_{pIDL})
	diameter	40mm	R_{pIDL}
	rotational inertia	$1e-4$kgm^2	J_{pIDL}
Driving mass	rotational inertia	1kgm^2	$-$*
Driving mass	rotational inertia	0.001kgm^2	J_{dv}
Belt	longitudinal stiffness	$150000N$	c
	Shear Layer Modulus	$5e7$N/m^2	G
	Radial Stiffness	$5e7$N/m^2	k
	Design Tension	400N	T_0
	mass per rib	0.018kg	$-$**
	number of ribs	6	$-$**
	Total Height	5mm	h

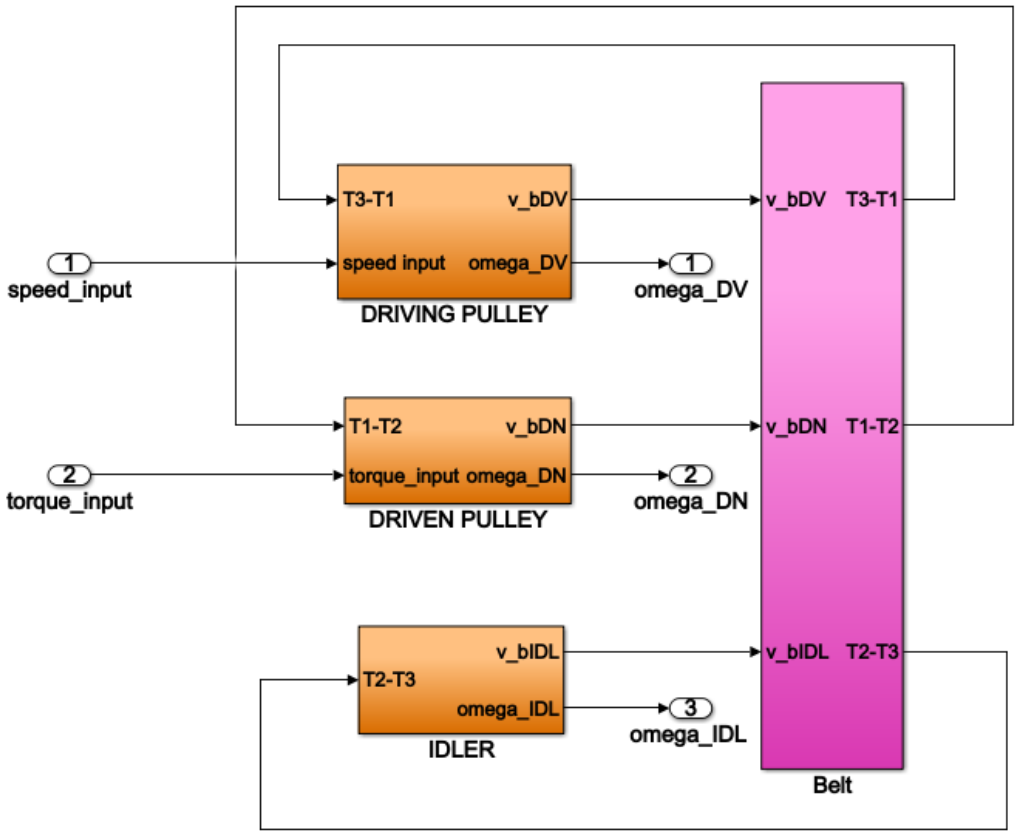

Fig. 5.15 Simulink® model of the 2 pulleys layout.

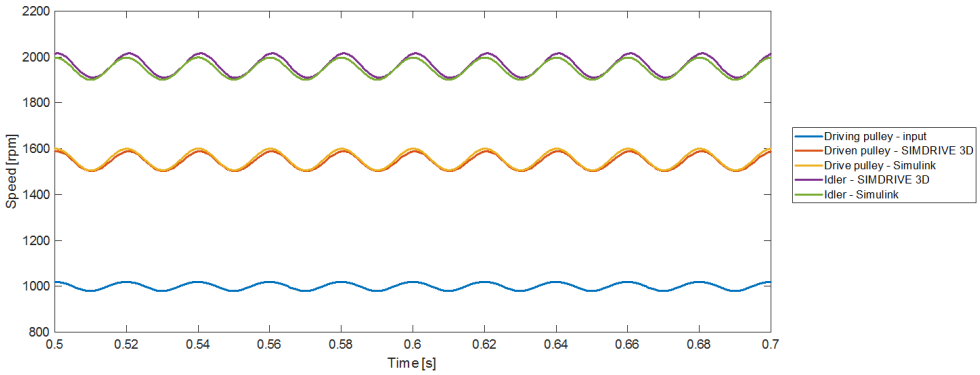

Fig. 5.16 Comparison of the simulation results between the SIMDRIVE 3D® and the Simulink® model of the 2-pulleys simple layout

forms. In this case by means of a Fourier excitation element a constant speed of 1000rpm with a vibration of amplitude 20rpm on the third order was used as input on the driving side. For what concerns the driven side, a characteristic curve was used to represent in a parametric form the characteristic torque consumption of an accessory: the curve provides a resistive torque on the driven mass corresponding to a certain rotary speed. After running the simulation, the two inputs used were registered as time histories and used as inputs for the Simulink® model. The results of the two simulations are shown in Fig. 5.16. A good correspondence can be found between the output speeds on both driven and idler pulleys provided by the two dynamic models.

Complete BDS Layout Model

In a second moment, the two modelling approaches were used to model the traditional automatic tensioner layout that was studied and experimentally investigated during the testing phase of this thesis. Such layout features four pulleys: crankshaft (CS), air conditioning compressor (AC), alternator (ALT) and tensioner (AT) pulley. Figs. 5.17 and 5.18 show the two models in the SIMDRIVE 3D® and MATLAB-Simulink® environments. In this case the CS pulley was modelled with the driving pulley block, while the ALT and the AC pulleys where modelled as driven pulleys. Only on the ALT element was used an excitation torque, so that on the SIMDRIVE 3D® no mass element appears attached to the AC pulley. In addition to the simple 2-pulleys model,

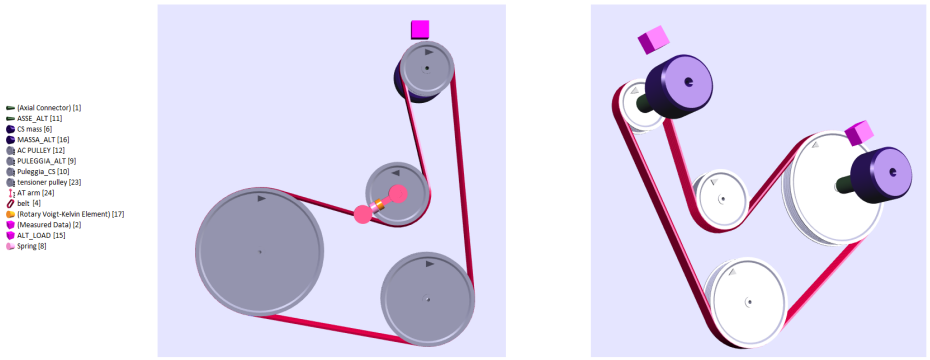

Fig. 5.17 SIMDRIVE 3D® model of the traditional automatic tensioner layout

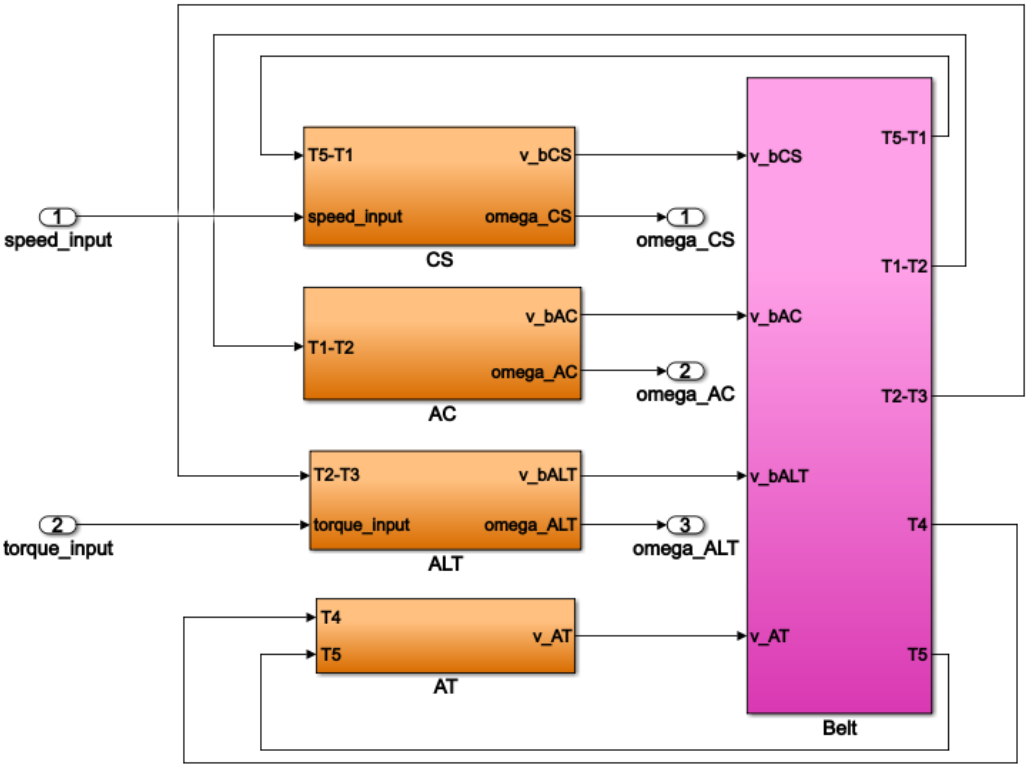

Fig. 5.18 MATLAB-Simulink® model of the traditional automatic tensioner layout

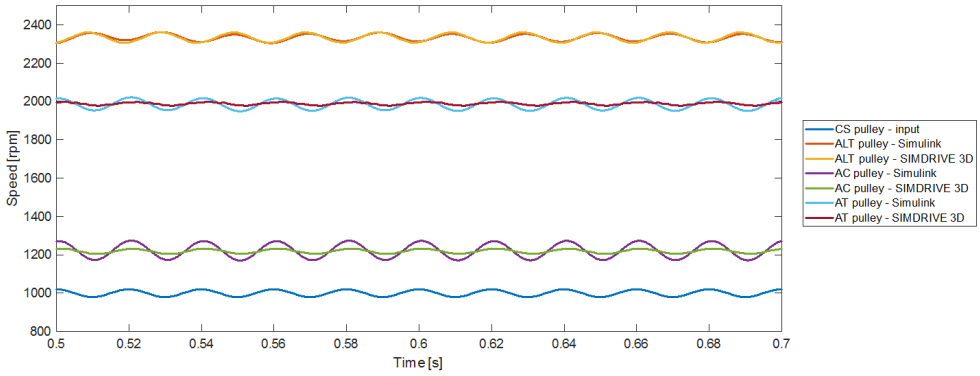

Fig. 5.19 Comparison of the simulation results between the SIMDRIVE 3D® and the Simulink® model of the traditional automatic tensioner layout

this drive has also an automatic tensioner which was built using a tensioner lever element for what concerns the SIMDRIVE 3D®, while it was modelled using the guidelines of this chapter in the MATLAB-Simulink® model, adopting the scheme in Fig. 5.13.
In a preliminary analysis, the two models were compared by means of the same inputs used for the 2-pulleys model seen above and the results are shown in Fig. 5.19. A good agreement can be found between the output speed on the ALT pulley provided by the two models, while for what concerns the output speed on the AC compressor pulley and on the tensioner pulley, the MATLAB-Simulink® appears to dampen the speed oscillation less then what the SIMDRIVE 3D® does.
Fig. 5.20 shows the lumped-parameters model of the drive, as it was represented by following the guidelines provided in the previous paragraphs. The complete lumped-parameters model shows what is expressed by the equations in the blocks of Fig. 5.18.

The last set of simulations was addressed to identify the resonance frequencies of the transmission. These simulations are those that will be compared to experimental measurements in the continuation of this thesis.
The simulations were performed keeping a constant speed on the crankshaft axis and applying an oscillating torque through the ALT motor varying in frequency. The detailed tests performed are the following:

- $\omega_{CS} = 860\text{rpm}$ with $C_{ALT} = -5 + 2\sin(2\pi f t)$, with $f = [0.1 - 40]\text{Hz}$

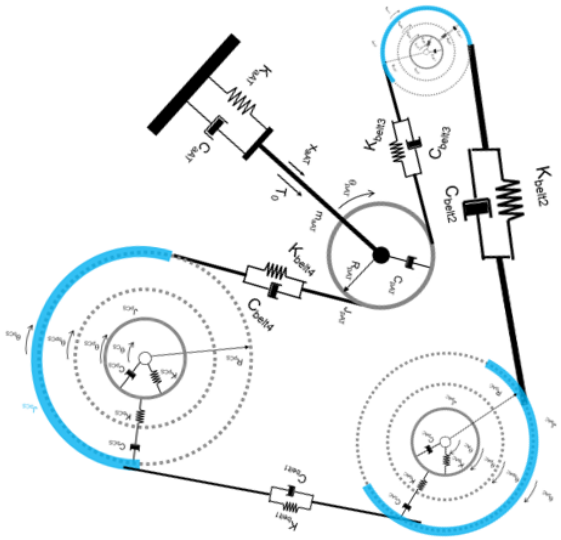

Fig. 5.20 Lumped-parameter model of the traditional automatic tensioner layout

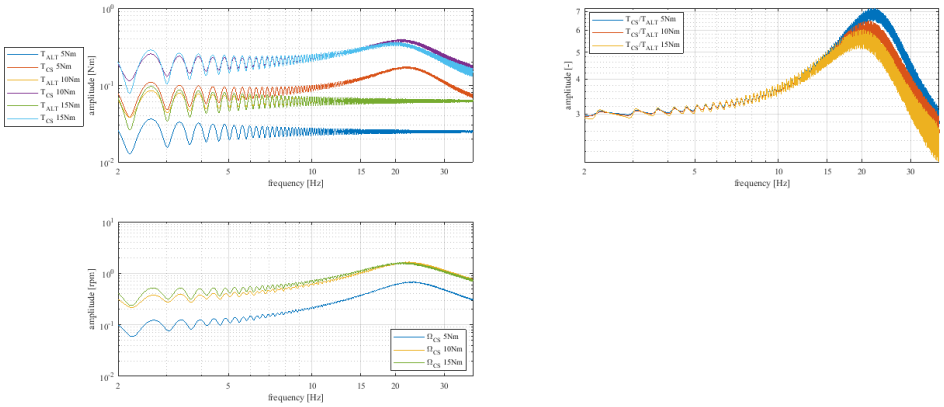

Fig. 5.21 MATLAB-Simulink results in terms of torque and speed values in the frequency domain

- $\omega_{CS} = 860$rpm with $C_{ALT} = -10 + 5\sin(2\pi ft)$, with $f = [0.1 - 40]$Hz
- $\omega_{CS} = 860$rpm with $C_{ALT} = -15 + 5\sin(2\pi ft)$, with $f = [0.1 - 40]$Hz

Figs. 5.21 and 5.22 show the results in the frequency domain of the two models simulations for the three ALT torque loads considered. In these images, it is shown how for different torque loads both the Simulink results identify the same resonance

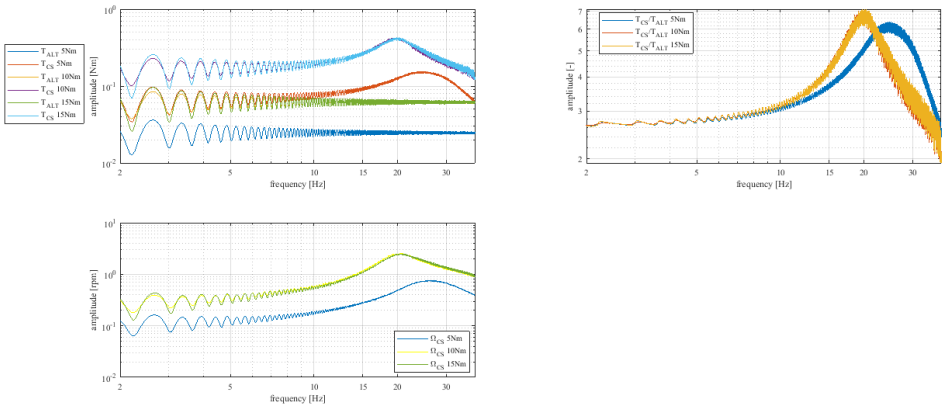

Fig. 5.22 Simdrive results in terms of torque and speed values in the frequency domain

frequency, while the Simdrive model provides a frequency of 20Hz for high torques and a higher frequency in the case of 5Nm, i.e. 25Hz.

5.3 Chapter Conclusions and Remarks

This Chapter provided a thorough description of the modelling activity that was conducted to investigate the performances, static and dynamic behaviour of BDS in micro-hybrid applications. Consistently, a first simulation assessment was provided for both models to verify their a priori suitability to represent the real behaviour of the drives. As underlined in the dedicated sections, both models underlie precise assumptions that identify the range of validity expected for each of them. In the case of the static model, all the friction effects of the system, on the tensioner arms, the bearings, the tensioner spring, were neglected and the belt was considered infinitely rigid. This assumptions limits the validity of the modelling approach to static conditions where no energy dissipation is involved. For what concerns the dynamic model, two main assumptions are the most stringent in defining the operability range of the model. First of all, the shear modelling approach on the contact interface between pulleys and belt, extended the Firbank's model to dynamic conditions, referring to the case where the motion of the pulley, or the belt, or both of them is given by a small amplitude vibration about the mean value. Additionally, the tensioner rotational and linear motions were considered decoupled under the assumption that the bisector of the contact arc, β_{at}, is constant. This can be acceptable

in the case of engine operating conditions where no large speed irregularities are present and no fast transient states take place. These two assumptions lead to a range of validity of the current dynamic model limited to operating conditions that exclude fast transient events that would cause fast and big tensioner movements or high slippage levels on the pulleys.
The experimental activity that will follow in the next Chapters will have the main goal of comparing the experimental results with the simulations and validating the models proposed. Ad-hoc tests will be performed in order to focus on the operating conditions that each model is addressed to.

Chapter 6

Experimental Setup

With the aim of supporting the research activity with experimental evidence, a test rig was designed to investigate in laboratory environment on the dynamic behaviour of belt drive systems and their power loss characteristics in static and dynamic conditions. In this Chapter a description of the dedicated test rig and its design process are presented.

The test rig offers major advantages over the utilization of engine cells that are traditionally used to test the functionality of automotive front end accessory drives (FEAD). Measurements obtained in such testing environments have a high level of uncertainty due to the uncontrollable irregularities that characterize the physical phenomena occurring into the ICE. This test rig was designed with the aim of creating an environment able to reproduce the working conditions with good accuracy and repeatability. This goal motivated the choice of a full-electric configuration with two electric motors that replicate the dynamic behaviour of the crankshaft and BSG pulleys, respectively. An electric drive for the crankshaft pulley allows to eliminate the uncertainties deriving from the ICE irregular vibrations usually affecting the FEAD. Moreover, an all-electric solution dramatically reduces the costs associated to the maintenance of a traditional engine test cell. Also, it offers the possibility of reproducing different layouts by suitably changing the mechanical interface between the electric motors and the accessories.

For measurement purposes, the test rig is able to host different sensors and actuators to monitor and control the overall status of the transmission system during operation. The test rig described in this section represents a complete novelty compared to the literature that was described in the previous chapters. As a matter of fact, the

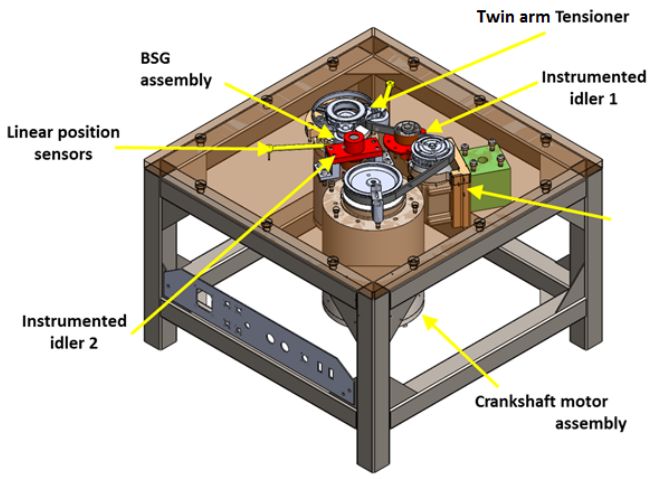

Fig. 6.1 Test rig CAD. The rig structure and the individual components of the BDS layouts were designed and realized ad-hoc for the corresponding application.

experimental campaigns performed in other research activities always involved very simple BDS configurations, mainly 2-pulley transmission that were designed ad-hoc for experimental aims. In this case the test rig is designed to be able to reproduce real automotive engine front end accessory drives and to allow experimental evaluations on the dynamic behaviour and the efficiency characteristics of complicated serpentine belt drive systems.
The description provided in the following refers mainly to the presentation done by the author in [100].

6.1 System Specifications

The design was performed to obtain the maximum versatility and allow the test rig to reproduce different kinds of BDS, both for what the mounting solutions and the characteristic of the components are concerned. The choice of the two electric motors was the central point of the design of the test rig. By analysing the behavior of both crankshaft and BSG pulleys on a real system it was possible to define the speed, bandwidth and torque specifications needed for the two electric motors.

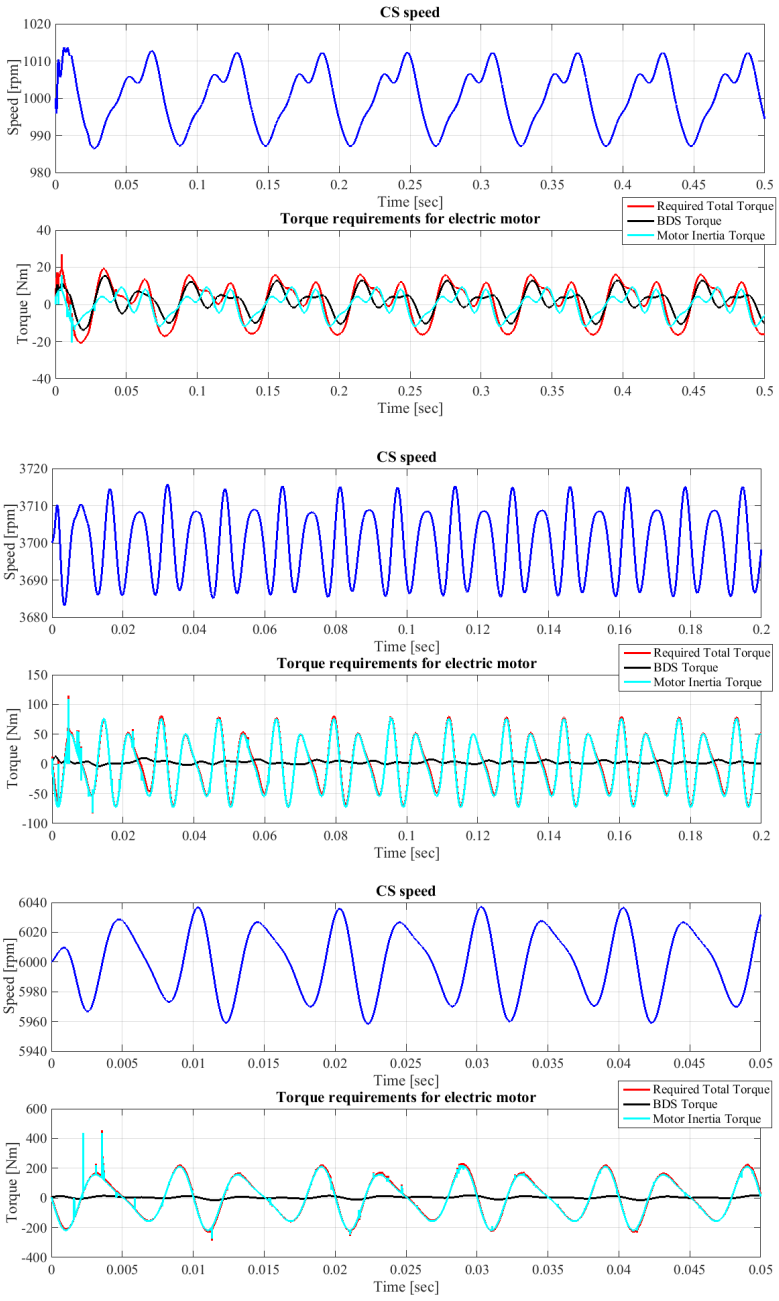

Fig. 6.2 Analysis of torque requirements for CS electric motor: in black, torque needed for operating the BDS; in light blue, torque needed to overcome the electric motor inertia; in red, resulting torque.

6.1.1 Crankshaft Pulley Vibrations Reproduction

The performances of the motor are given by rated and maximum values of speed and torque and by the bandwidths reachable with current and velocity control loops. Consequently it was important to define such specifications, taking into account the desired reference values and dynamics, the layout characteristics and the additional inertia of the electric motor.
The definition of the required specifications took the following steps. Firstly, the required speed was derived by the operating speed values of the real ICE, which arrives to 6000rpm. Secondly, the crankshaft speed imposed by the ICE to the crankshaft pulley was measured on an engine test cell. Amplitude and phase of the main harmonics were identified analitically by implementing a curve fitting procedure, using the formula in (6.1) as suggested by [101].

$$\omega_i = \omega_{mean} + \sum_{n=1}^{4} nA_n cos(\omega_{mean} t + \phi_n) \tag{6.1}$$

The obtained speed references were used as input on a model describing the real layout that provided the measurements. The model was built using the process that was described in Chapter 4. This analysis brings to two relevant results both defining the bandwidth needed for speed and current control loops of the inverter controlling the electric motor and determining the torque needed to reproduce the harmonics amplitudes based onto the inertia of the electric motor. The analysis compared different electric motors available on the market taking into consideration the corresponding inertia values. In Fig. 6.2 is shown the analysis of torque requirements at different speeds for the selected motor which has a low inertia value. In black is indicated the torque component needed for operating the BDS, in light blue the torque needed to overcome the electric motor inertia and in red the resulting torque that the motor will need to finally provide. As clearly highlighted by Fig. 6.2, the main contribution to the overall torque is required to overcome the electric motor inertia. This consideration allows to study the torque requirements taking into account only such contribution and motivated a design of the shafts with minimum inertia properties.
The selected electric motor by BoschRexroth represented the best trade-off between speed, bandwidth and torque requirements. Its rated and maximum speed are respectively 2600rpm and 12000rpm, being therefore able to reach the desired 6000rpm.

The bandwidth of the current loop is equal to 520Hz if its PI controller is calibrated as indicated by the producer's specification for optimized performances. This leads to a maximum reachable bandwidth for the speed control loop of 260Hz. Consequently, the motor allows to reproduce all the harmonic components with their amplitude values up to 4000rpm, after this value 1^{st} and 2^{nd} harmonics will still be completely reproduced while 3^{rd} and 4^{th} will be attenuated but not eliminated provided we do not overcome the peak torque. The rated and maximum torque values are respectively 140Nm and 320Nm. As shown in Fig.6.2 to a speed of 6000rpm corresponds a maximum torque of around 200Nm which can be fully reproduced with a duty cycle of 10% on a period of 10 minutes, which is sufficient for the tests that will be performed. The values of rated and maximum torque define the maximum amplitudes that the electric motor is capable of replicating for each harmonic. Such analysis was analytically performed taking into account only the electric motor inertia and then compared to the results of the simulations that included the BDS effects. Each harmonic component was considered autonomously and its contribution was calculated and simulated neglecting the other components. The analytical calculations provided therefore the envelopes of the allowed amplitude values that are shown in Fig. 6.3. In Fig. 6.3 is also shown the comparison between calculated and simulated values. It is clear how the torque required for operating the BDS represents a small portion of the overall required torque. It is important to notice that at low speeds the torque required for the accessories, and in particular the alternator, become higher and no longer neglegible. This effect is particularly clear for what concerns the first harmonic.

6.1.2 BSG Specifications

The speed requirements of the electric motor used to reproduce the BSG functioning simply derive from the speed specifications of the crankshaft pulley through a transmission ratio. The torque requirements are defined by the functionalities performed by the BSG in motor mode. As it was previously described in this thesis, two different operating modes need to be considered: generator mode or motor mode. The *generator mode* corresponds to the functions of a traditional alternator and of regenerative braking. The *motor mode* is alternatively used to perform an electric boost or a start and stop function, that is to say the cranking of the ICE. The most critical function is the cold cranking, which happens when the start and stop is

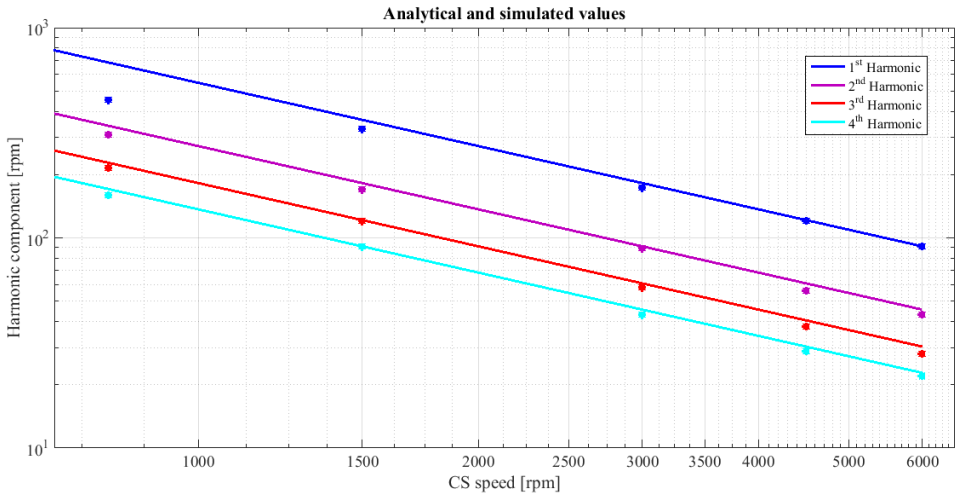

Fig. 6.3 Envelopes of harmonic contributions and comparison with simulation results

realised in cold engine conditions. This mode required the BSG to be able to provide up to 40Nm to the system. The selected motor was again a BoschRexroth brushless motor, model MSS102D-0800. The data of such electric motor can be found in Table 6.1.
In Fig.6.4 can be seen the torque-speed characteristic required for the BSG motor. Such requirement is completely fulfilled by the characteristics of the selected electric motor.
The two selected electric motors were characterised by a frameless configuration and an integrated liquid cooling that facilitated a smooth integration of their assemblies with the rest of the test rig.

Table 6.1 Characteristics of Electric Motors

Function	Rated Speed ω [rpm]	Max Speed ω_{max} [rpm]	Rated Torque C [Nm]	Max Torque C_{max} [Nm]	Rated Power P [kW]	Rated Current I [A]	Max Current I [A]
Crankshaft	2600	12000	140	320	38.1	71	200
BSG	8000	22500	20	45	16.8	24	69

6.2 Control Architecture

The control architecture of the test rig is composed by a high voltage area and a low voltage control section that computes the reference speeds and torques to give as an

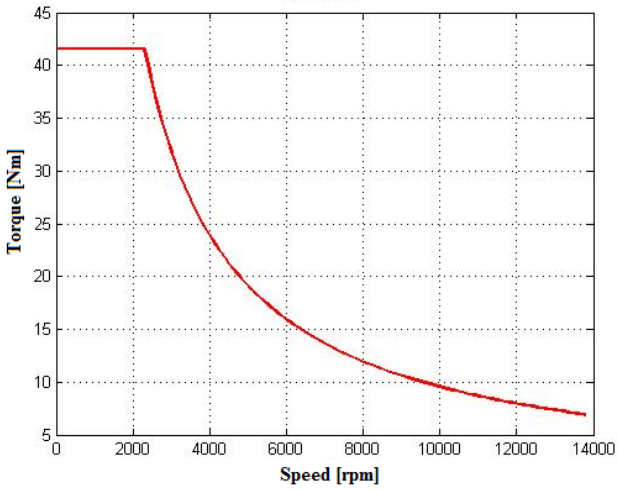

Fig. 6.4 Required BSG characteristic

input to the control loops of the two electric motors and that is in charge of acquiring and analyzing the data read by the sensors mounted on the test rig. In the following the electric motor used to replicate the Crankshaft pulley behaviour will be referred to as Motor 1, while the BSG motor will be called Motor 2.
The power supply (HMV01.1R-W0065-A-07 by BoschRexroth) powers both the inverters that are connected on the same DC BUS. This supply unit is able to regenerate the power, that is to say to give back to the network the power produced by one of the two motors which it is acting as alternator. The modular power section is completed by two BoschRexroth inverters, HMS01.1N-W0210 for Motor 1 and HMS01.1N-W0070 for Motor 2. The control sections (CSH01.1C-CO-ENS-EN2-MEM-L2-S) are the same for both inverters and provide three nested control loops: current, speed and position control. The two inverters allow the users to provide speed or torque references from outside their firmware by means of a dedicated control unit. The control laws implemented on the inverters' firmware consist of a Proportional-Integral (PI) compensator for each control loop. The two control sections allow the utilization of some optional features for analog and digital inputs and outputs, encoders acquisition, serial interface towards commissioning tool on PC, master communication with control interface through CANOpen Protocol.
The control interface that operates on the test rig is realized by means of a dSpace Advanced Control Education Kit MicroLabBox Platform which collects both analog and digital signals from the inverters and the sensors mounted on the test rig and

sends them via an Ethernet Interface to a PC. On the PC a Human Man Interface, realized with the dSpace Control Development Software ControlDesk, processes all the signals and is in charge of providing the reference signals of speed and torque to the two inverters of the electric motors. The communication between the BoschRexroth inverters and the MicroLabBox happens through CANopen protocol. The MicroLabBox Platform is able to read from the inverters all the information of interest about the two electric motors: torque, speed, direct-axis current, quadrature-axis current. Thanks to the characteristics of the test rig and its monitoring system it is possible to add several sensors to monitor any variable considered of interest. As a matter of fact, in parallel to the information retrieved from the inverters, the MicroLabBox has available a number of digital and analogic I/O ports that allow the information collection from the additional sensors mounted on the test rig. The analog signals need to be filtered after the acquisition by the control software.
In the following an in-depth description of the BDS layouts that were used for the experimental activity is provided. Contextually, the sensors used for each configuration are described.

6.3 BDS Layouts

As can be seen in the CAD drawing of the test rig in Fig. 6.1, the test rig was designed with the shape of a table where the BDS layouts can be reproduced in a horizontal place. This choice was done to obtain a uniform distribution of the forces acting on the frame and to avoid possible bending stresses on the bearing structure. Two different BDS layouts were realized for the experimental activity performed during this research:

- A traditional FEAD mounting an automatic tensioner on the slack span, shown in Fig. 6.5.
- A BSG-based BDS layout mounting a twin-arm omega tensioner whose pulleys act on both the spans insisting on the BSG pulley, described in Fig. 6.6.

In both of these layouts, the AC compressor was mounted as a unit to have the possibility to use it as a load or to leave it deactivated and working as an idler pulley. Fig. 6.5 shows the traditional FEAD layout which is the simplest among the three

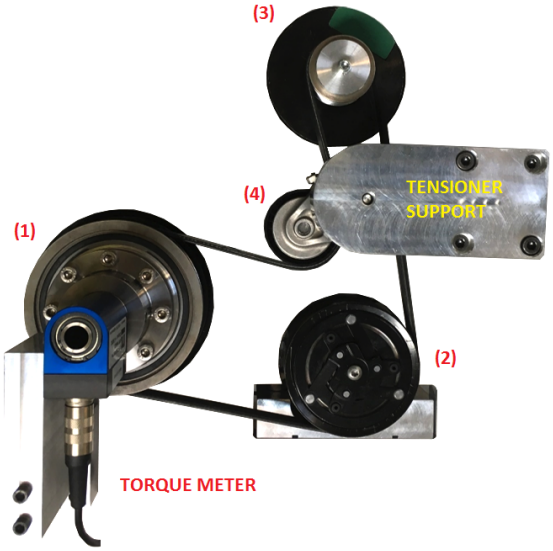

Fig. 6.5 First BDS configuration with traditional automatic tensioner. The layout features 4 pulleys: (1) Crankshaft pulley, (2) air conditioning compressor, (3) alternator pulley and (4) tensioner pulley.

configurations that were studied and mounts only four pulleys: crankshaft, air conditioning compressor, alternator and tensioner pulley. The configuration uses a 5-ribbed belt. In this case no data on the geometric and inertial characteristics of the components can be provided because of industrial property. This layout was used to perform tests investigating about the efficiency of the transmission and its dynamic behaviour: the tests were used to validate the corresponding models.
Fig. 6.6 shows the second layout corresponding to a BSG-based BDS. The configuration consists in seven pulleys: crankshaft, air conditioning compressor, 2 idler pulleys, the two tensioner pulleys and the BSG. The V-ribbed belt in charge of the power transmission is characterised by 6 ribs. Again, no geometric nor inertial data can be provided due to industrial interests.

6.3.1 Sensors

The main measurements performed on the test rig are the speed and the torque values of the two electric motors. The inverters receive a feedback of speed from two equal modular magnetic encoders ERM 2984 by Heidenhain (line count 192, $1V_{pp}$

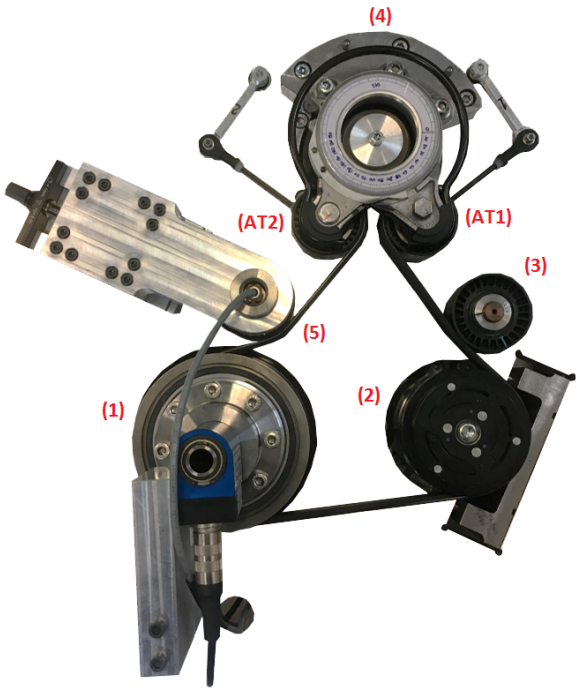

Fig. 6.6 Second BDS configuration with omega twin-arm tensioner. The layout features 7 pulleys: (1) Crankshaft pulley, (2) air conditioning compressor, (3,5) two idler pulleys, (AT1, AT2) two twin arm tensioner pulleys, and (4) BSG pulley.

sinusoidal incremental signals, maximum rotational speed 47000rpm, power supply $5V_{dc}$) which are mounted on the shaft of the two motors. These sensors are present in each of the considered configurations. In the case of the first layout, the angular speeds of the crankshaft and BSG pulleys were additionally monitored by means of two optical tacho sensors. These devices employ a photoelectric sensor (OPB705 by Optek, power supply $5V_{dc}$) that detects the reflection of a line pattern printed onto the pulley surface.

For both the electric motors, it is possible to calculate the torque values from the corresponding current feedbacks in the direct and quadrature axis. In order to obtain a more reliable and direct measurement, a torque meter was introduced for the crankshaft torque measurement.

Two different approaches were followed for the belt tension measurements. In static conditions a CLAVIS tension probe was use to evaluate the belt pretension. For what concerns the tension in dynamic conditions, an indirect measurement was performed by means of idler pulleys whose hub was instrumented with a radial load cell (DB-DA-750-17 by Magtrol, nominal force 750N, power supply $5V_{dc}$). The

outputs of the load cells were amplified by means of an HBM Force Measurement System amplifier which was then connected to an analog port of the MicroLabBox Platform. In the dSpace hardware, the 14-bit analog channels were used to read the load cell amplified signals.
In the case of the two layouts reproducing a BSG-based BDS with twin-arm (alpha or omega) belt tensioner, the angular positions of the two tensioner pulleys were measured by means of two incremental encoders (8.KIS40.1342.2500 by Kubler, 2500 lines of resolution, Push-Pull output circuit, power supply 10V). As it is shown in Fig. 6.6, where the twin arm tensioner pulleys are indicated as (AT1,AT2), each encoder is hinged to its respective tensioner pulley by means of a two-link kinematic arrangement. This mechanism was designed to follow and reproduce the angular displacement of the tensioner arms. In the MicroLabBox device, the tensioner arm encoders are processed by direct capture inputs and sent via Ethernet to the host PC to be recorded and analysed.

6.4 Test Rig Structural Set-up

After defining the characteristics of the electric motors to be used to replicate CS and BSG pulleys behaviour together with the other components of the drives to be replicated, it is important to define a test rig frame with appropriate structural properties and vibrations damping capability to overcome the stresses generated by the torque transmission from the motors to the accessories when the drive system is running.
In order to have a uniform distribution of the forces, due to the weight of the electrical motors and their housings, and a more simple, flexible and compact design, the transmission layouts were chosen to be reproduced horizontally. As a result, the function to keep fixed the motor housing and all the electrical and mechanical accessories is fulfilled by an horizontal plate installed on the top of a steel alloy table, which additionally has the function of supporting the overall weight of the system.
A modal analysis of the designed frame was performed to check for natural frequencies. Resonance during operation must be avoided in order not to compromise the structural integrity of the assembly. Therefore natural frequencies should be placed at values as high as possible, considering constraints in terms of available space and

weight. The vibrations generated when the test rig is running are damped by four damping elements by EluFlex placed at the base of the vertical beams of the frame. These devices are made of aluminum alloy AlMgSi1 with a core of natural rubber and are free standing, i.e. they doesn't need to be fixed to the ground.
The selection of the right dampers depends on the weight of the test rig and on the resonant frequency. The mass of the whole designed structure, including the two electrical motors and their housings was measured to be about 260÷280 kg, considering also the presence of the accessories. So each dampers must be able to bear a quarter of this weight: the EluFlex 60-100 SB damper, that have a maximum bearing mass of 100 kg was chosen for the studied application.

In Figs. 6.7, 6.8, 6.9 some pictures of the test rig are shown. The table-shaped structure supports the plate where different drive layouts can be reproduced. An electric cabin contains all the electric and electronic devices for monitoring and control of the overall system.

6.5 Chapter Conclusions and Remarks

In this Chapter, an accurate description of the experimental setup used in this research was provided. The design characteristics, the control and monitoring architecture were described for the different BDS layouts that were experimentally investigated during the research activity.
The first layout that was considered is a traditional front end accessory drive with an alternator that has no BSG function. This layout was used not only to investigate over the efficiency of the transmission but also to validate the dynamic model that the author built with the guidelines described in Chapter 5. Such experimental investigation is described in Chapter 7.
The second layout represents a BSG-based applications where an omega twin-arm tensioner is employed to face the operating modes of such micro-hybrid application. On this layout tests were performed to evaluate its functionality and efficiency in quasi-static conditions and compare its performances to the traditional automatic tensioner studied before. The results of these experiments is shown in Chapter 7.

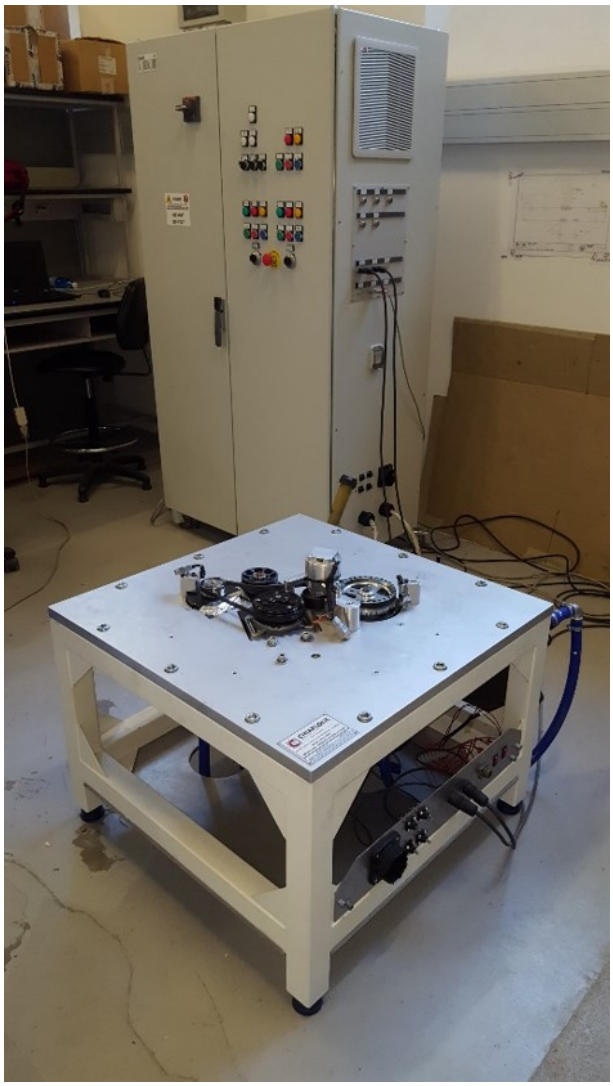

Fig. 6.7 Complete structure of the dedicated test rig that was designed for the experimental activity of this thesis. In the background the electric cabin can be seen, where the high al low voltage electric devices are placed.

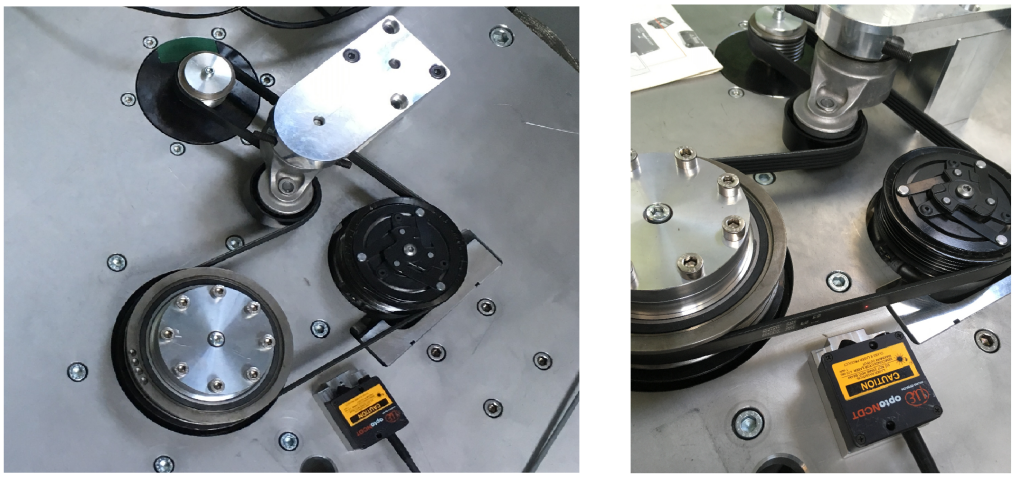

Fig. 6.8 Pictures of the traditional automatic tensioner layout that was replicated on the test rig.

Fig. 6.9 Pictures of the twin arm tensioner layout that was replicated on the test rig.

Chapter 7

Experimental Characterization

In this Chapter the various phases of the research activity object of this thesis are described.
In the first part, the static analysis of the traditional automatic tensioner and the omega twin arm tensioner layouts is carried out. The two drives are studied and compared in terms of overall power losses and transmission efficiency. A modelling approach is proposed to highlight the power losses dependency on belt slip, belt preload and torque loads. Additionally the quasi-static tests are used to validate the static model that was proposed in Chapter 5.
In the second part the dynamic behaviour of the traditional automatic tensioner layout is investigated and compared to the related model, both in the time and frequency domains.

7.1 Static analysis

The main interest of this testing phase was to experimentally evaluate the efficiency of a BDS layout considering a real automotive front end accessory drive. At first, starting from the acquired knowledge on the power losses phenomenology in BDS that emerged from the research described in Chapter 3, the focus was to prove that the general conclusions that are valid for simple 2-pulley transmissions are still applicable for more complex serpentine belt drive systems. In particular it was interesting to investigate:

- the behaviour of slip, torque losses, power losses and efficiency for increasing load demands from the alternator or BSG
- the decomposition of the power losses in their contributions of speed and torque losses
- how the torque losses prevail over speed losses for low loads and are proportional to the bending frequency of the belt
- how torque losses increase with the system speed imposed by the crankshaft resulting into in increase of the overall power losses
- how torque losses are constant over increasing torque demands
- how the speed losses depend mainly on the tension state of the system, which depends mainly on the torque transfer so it results almost constant over the speed and increases with the torque.
- how the speed losses are almost negligible at low loads but dramatically increase above a maximum transmittable torque value taking the upper hand over the torque losses
- the dependency of the torque losses over the slip state of the transmission

With the goal of analysing the described points, a set of tests was conceived and performed. The results obtained on the traditional FEAD layout were used to model and define a modelling procedure for the power losses of automotive BDS that can constitute a useful tool for the evaluation of the transmission performances.
The same set of tests were performed both on the normal production layout and on the omega twin-arm tensioner transmission. As a result it was possible not only to evaluate the efficiency of the twin-arm layout in its two characteristic operating modes, namely motor and alternator modes, but also to compare the transmission performances with the normal production case for what concerns the alternator mode and to define the advantages and disadvantages of the use of such a tensioning mechanism.
A further elaboration of the data obtained on the omega twin-arm tensioner layout allowed to verify its functionality in motor and generator modes. Such experimental behaviours were compared to the outputs of the static model that was built in Chapter 5.

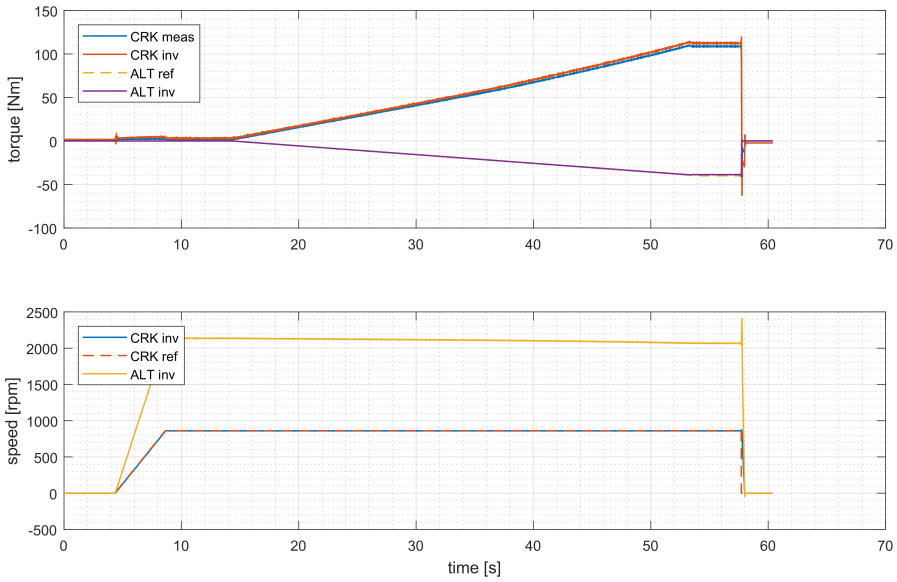

Fig. 7.1 Example of quasi-static test. The inputs in terms of CS speed and ALT torque are plotted together with the corresponding measured feedbacks from the plant. In the upper diagram: *ALT ref* corresponds to the torque input on the alternator; *ALT inv* and *CRK inv* are the torques calculated based on the two electric motors currents measured on the rig and fedback to the two inverters by the current probes; *CRK meas* is the crankshaft torque measured through a torquemeter. In the lower diagram: *CRK ref* is the reference crankshaft speed used as input to the system; *CRK inv* and *ALT inv* are the measured rotary speeds read by the encoders and fedback to the two electric motors inverters.

7.1.1 Procedure

For the evaluation of the static characteristics of the transmission, quasi static tests were carried out to simplify the analysis of the studied devices.
Before the experiments, the belt pretension is set to the desired value. This force is verified with a CLAVIS type 6 belt tension meter. A range between 150N and 400N is considered, with steps of 50N, obtaining 6 different operating conditions.
In each test, the crankshaft speed ω_{cs} is fixed to a constant value. Three speed values are tested to address different engine conditions, 860rpm, 2500rpm, 3200rpm. Then, a torque ramp is applied with the ALT to load the system. The sign of this torque defines whether the BSG operates as a motor $(+)$ or as a generator $(-)$. A sufficiently low slope of ± 1 Nm/s is followed to avoid the introduction of unwanted inertial effects. When the system reaches the maximum belt slip allowed $s_{min} = \frac{\omega_{CS} - \omega_{ALT_{min}}/\tau}{\omega_{CS}}$, fixed at 4%, the system is stopped. The belt slip of the system is calculated based

on the speed measurements provided by the two rotary encoders mounted on the CS and ALT motors axes. Corresponding to the maximum belt slip the maximum transmittable torque is identified for each pretension condition. In this study, the CS and ALT speeds and torques are measured during the torque ramp of the ALT. An example of the inputs and outputs monitored during quasi-static tests is shown in Fig. 7.1. For what concerns the inputs and outputs of torque, in Fig. 7.1 it is possible to identify: *ALT ref* which corresponds to the torque input on the alternator; *ALT inv* and *CRK inv* are the torques calculated based on the two electric motors currents measured on the rig and fedback to the two inverters by the current probes; *CRK meas* is the crankshaft torque measured through a torquemeter. In the case of the rotary speed inputs and outputs, Fig. 7.1 shows: *CRK ref* which is the reference crankshaft speed used as input to the system; *CRK inv* and *ALT inv* are the measured rotary speeds read by the encoders and fedback to the two electric motors inverters.

7.1.2 Results

Traditional Automatic Tensioner Layout

Figs. 7.2, 7.3 and 7.4 show the layout behaviour for the testing conditions that were taken into account. From the measurements of torque and speed on the CS and ALT pulley the following quantities are calculated and plotted to evaluate the system behaviour:

- Belt slip on the ALT pulley:

$$s_{\%} = \frac{\omega_{CS} - \omega_{ALT}/\tau}{\omega_{CS}} \text{x}100 \tag{7.1}$$

- Power loss

$$P_{loss} = C_{CS}\omega_{CS} + C_{ALT}\omega_{ALT} \tag{7.2}$$

- Efficiency

$$\eta = \left(1 - \frac{P_{ALT}}{P_{CS}}\right) \text{x}100 \tag{7.3}$$

The same measurements were performed for different initial belt preloads, in the range $[150-400]$N, with a step of 50N. The measurements show how the belt

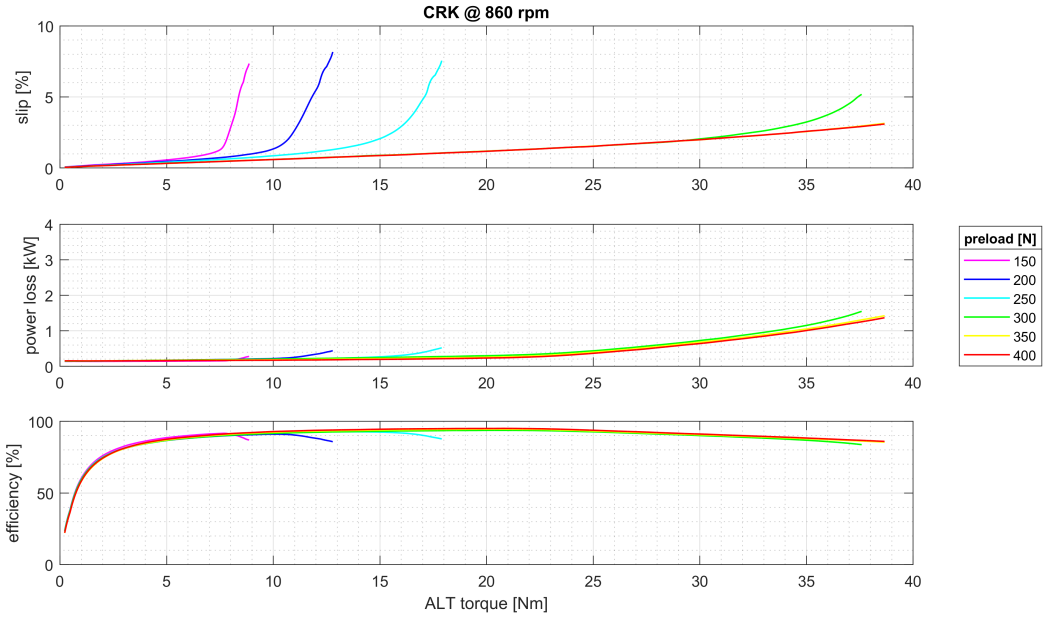

Fig. 7.2 Quasi-static test on the normal production layout for constant CS speed at $\omega_{CS} = 860rpm$. Different initial belt preloads, in the range $[150-400]$N, with a step of 50N. Belt slip on the BSG pulley ($s_{\%} = \frac{\omega_{CS}-\omega_{ALT}/\tau}{\omega_{CS}}$x100), power loss ($P_{loss} = C_{CS}\omega_{CS} + C_{ALT}\omega_{ALT}$) and efficiency($\eta = \left(1 - \frac{P_{ALT}}{P_{CS}}\right)$x100) are measured for different initial belt preloads.

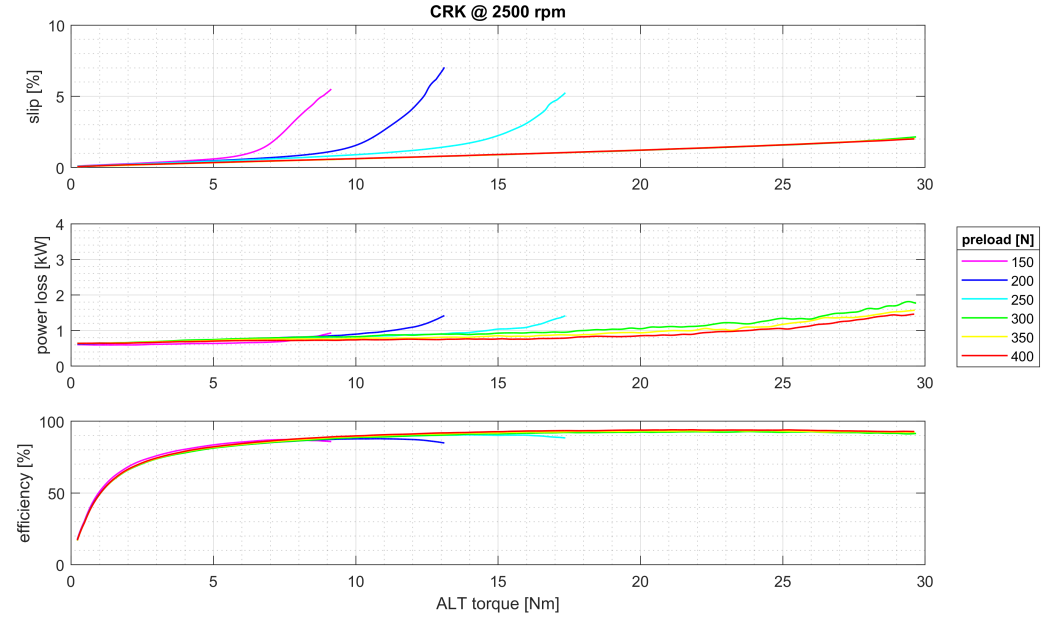

Fig. 7.3 Quasi-static test on the normal production layout for constant CS speed at $\omega_{CS} = 2500rpm$. Different initial belt preloads, in the range $[150-400]$N, with a step of 50N. Belt slip on the BSG pulley ($s_{\%} = \frac{\omega_{CS}-\omega_{ALT}/\tau}{\omega_{CS}}$x100), power loss ($P_{loss} = C_{CS}\omega_{CS} + C_{ALT}\omega_{ALT}$) and efficiency($\eta = \left(1 - \frac{P_{ALT}}{P_{CS}}\right)$x100) are measured for different initial belt preloads.

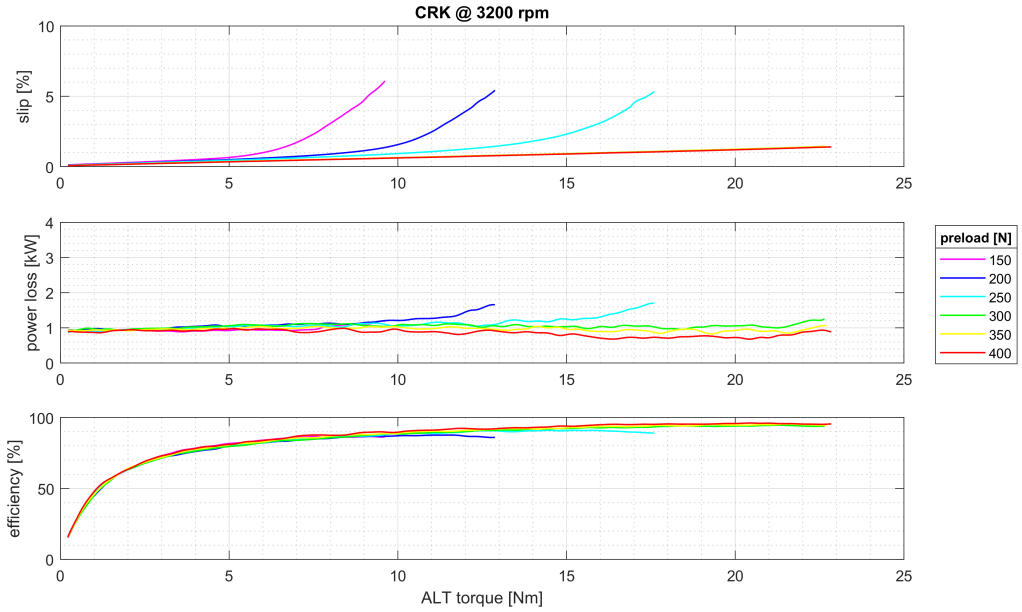

Fig. 7.4 Quasi-static test on the normal production layout for constant CS speed at $\omega_{CS} = 3200rpm$. Different initial belt preloads, in the range $[150-400]$N, with a step of 50N. Belt slip on the BSG pulley ($s_{\%} = \frac{\omega_{CS}-\omega_{ALT}/\tau}{\omega_{CS}}$x100), power loss ($P_{loss} = C_{CS}\omega_{CS} + C_{ALT}\omega_{ALT}$) and efficiency($\eta = \left(1 - \frac{P_{ALT}}{P_{CS}}\right)$x100) are measured for different initial belt preloads.

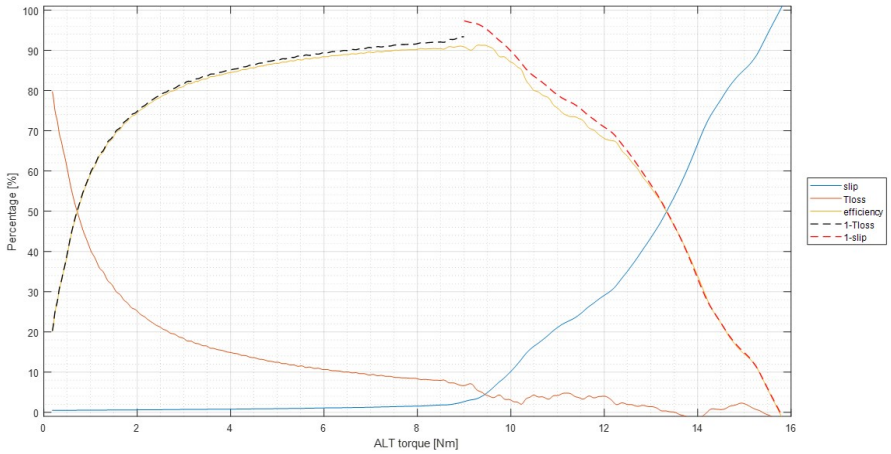

Fig. 7.5 Quasi-static test on the normal production layout for constant CS speed at $\omega_{CS} = 860rpm$. Initial belt pretension set to $T_0 = 150$N. Comparison between the behaviour of the belt slip, the torque loss and the efficiency over increasing load torques requested by the alternator. The efficiency results to be inversely proportional to the torque loss up to the maximum transmittable torque, and inversely proportional to the belt slip for higher torque demands.

preload defines the transmission limits and its maximum transmittable torque. The same behaviour is observed for the different operational speeds that were taken into account. It results that power losses are directly proportional to the speed and are higher for lower belt preloads.
Fig. 7.5 shows a more extensive analysis conducted for the case of constant crankshaft speed of $\omega_{CS} = 860$rpm. Together with the percentage of sleep loss (belt slip) and power loss (efficiency), also the system torque loss is plotted. The torque loss is defined as:

$$C_{loss_{\%}} = \left(1 - \frac{C_{ALT}}{C_{CS}}\right) \text{x} 100 \tag{7.4}$$

In this case, the measurement was performed reaching higher alternator torque values over the $s_{\%} = 4\%$ limit previously respected. The plot shows how the efficiency of the transmission is higher for lower percentage torque losses, which corresponds to higher alternator torque requests. Additionally it highlights the system behaviour for high slippage conditions where the efficiency decreases dramatically in a manner that is inversely proportional to the slip. As a results, the efficiency is shown to be inversely proportional to the torque loss up to the maximum transmittable torque, and inversely proportional to the belt slip for higher torque demands.

Omega Tensioner Layout

Figs. 7.6, 7.7 and 7.8 show the layout behaviour for the testing conditions that were taken into account. From the measurements of torque and speed on the CS and BSG pulleys belt slip, system power loss and efficiency, were calculated as defined in the previous section, in Eqs. 7.1, 7.2 and 7.3, and plotted to evaluate the system behaviour. The same measurements were performed for different initial belt preloads, in the range $[200 - 400]$N, with a step of 50N. The generator and motor modes are represented together and correspond to negative and positive BSG torques respectively. The results highlight the omega tensioner capability of performing equally in both operating modes up to high torque values. The slip keeps very low over the whole torque request range and no maximum transmittable torque was found in neither the operating modes. The omega tensioner results to be a very

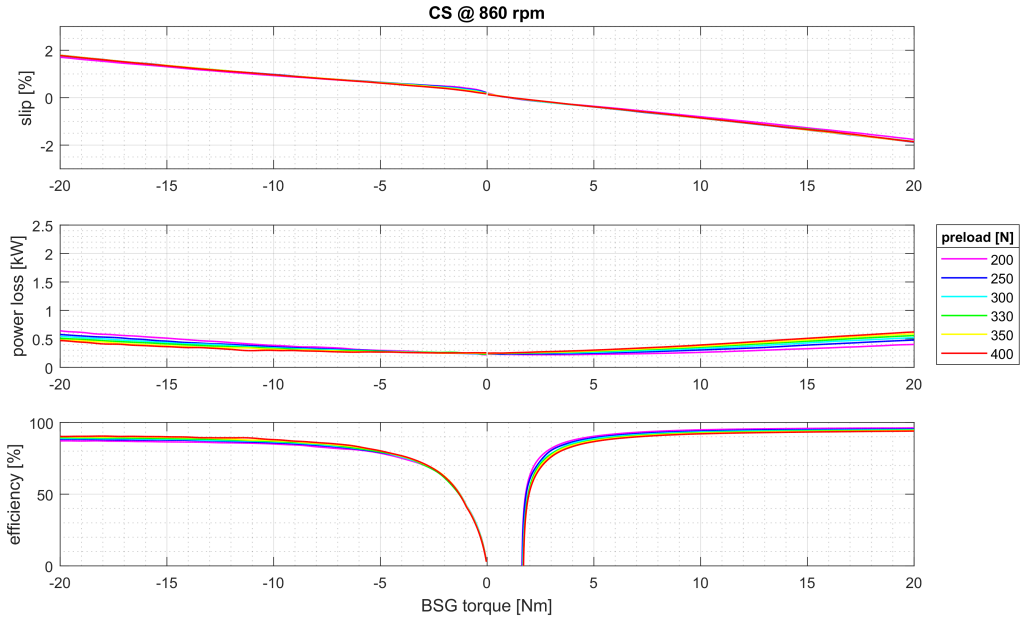

Fig. 7.6 Quasi-static test on the twin arm tensioner layout for constant CS speed at $\omega_{CS} = 860rpm$. Different initial belt preloads, in the range $[200-400]$N, with a step of 50N. Belt slip on the BSG pulley ($s_{\%} = \frac{\omega_{CS}-\omega_{ALT}/\tau}{\omega_{CS}}$x100), power loss ($P_{loss} = C_{CS}\omega_{CS} + C_{ALT}\omega_{ALT}$) and efficiency($\eta = \left(1 - \frac{P_{ALT}}{P_{CS}}\right)$x100) are measured for different initial belt preloads.

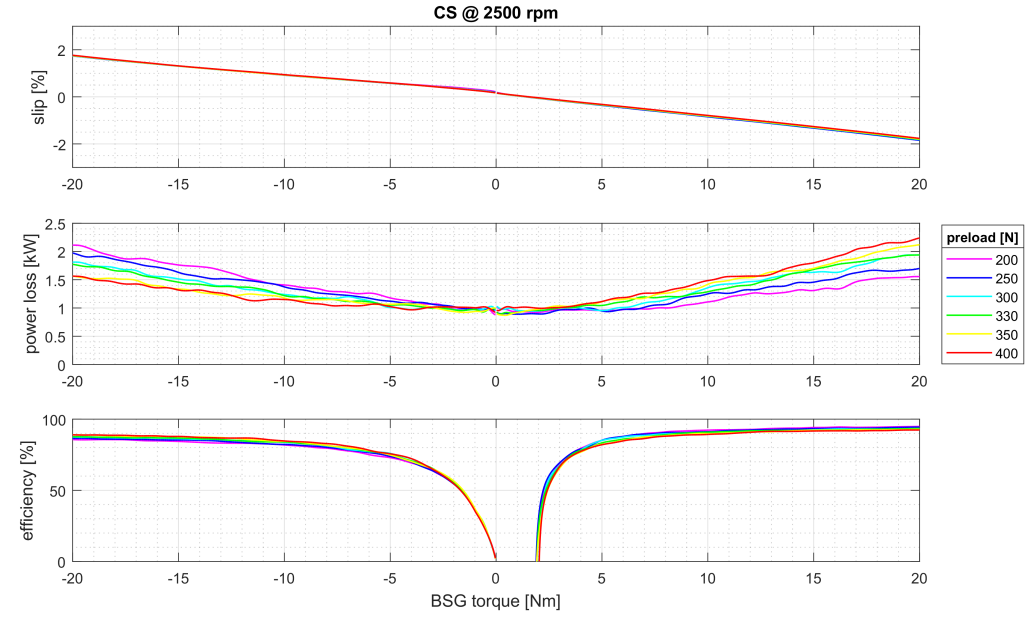

Fig. 7.7 Quasi-static test on the twin arm tensioner layout for constant CS speed at $\omega_{CS} = 2500rpm$. Different initial belt preloads, in the range $[200-400]$N, with a step of 50N. Belt slip on the BSG pulley ($s_{\%} = \frac{\omega_{CS}-\omega_{ALT}/\tau}{\omega_{CS}}$x100), power loss ($P_{loss} = C_{CS}\omega_{CS} + C_{ALT}\omega_{ALT}$) and efficiency($\eta = \left(1 - \frac{P_{ALT}}{P_{CS}}\right)$x100) are measured for different initial belt preloads.

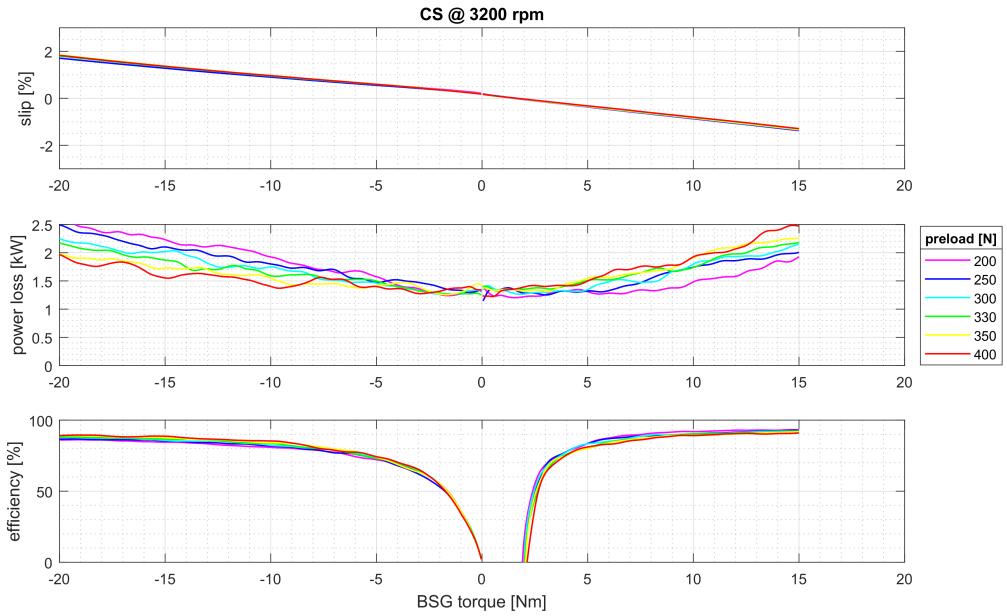

Fig. 7.8 Quasi-static test on the twin arm tensioner layout for constant CS speed at $\omega_{CS} = 3200 rpm$. Different initial belt preloads, in the range $[200-400]$N, with a step of 50N. Belt slip on the BSG pulley ($s_{\%} = \frac{\omega_{CS}-\omega_{ALT}/\tau}{\omega_{CS}}$x100), power loss ($P_{loss} = C_{CS}\omega_{CS} + C_{ALT}\omega_{ALT}$) and efficiency($\eta = \left(1 - \frac{P_{ALT}}{P_{CS}}\right)$x100) are measured for different initial belt preloads.

symmetric device not only in terms of geometry but also for what the performances of the system are concerned.

7.1.3 Layouts' Comparison and Performances Modelling

Figs. 7.9 and 7.10 compare the two measured layouts in generator mode for two different belt pretensions, that's to say $T_0 = 250$N and $T_0 = 300$N, and different CS speeds, again $\omega_{CS} = 860$rpm, $\omega_{CS} = 2500$rpm, and $\omega_{CS} = 3200$rpm. These images help to highlight the influence of belt pretension, torque load and belt speed on the layout performances. Additionally, the change from one layout to the other, with the two different tensioning devices and an additional idler pulley are highlighted. From the automatic tensioner layout to the twin arm tensioner layout, two additional small-diameter pulleys can be found in the transmission and therefore higher torque losses, especially bending losses, are to be expected.
For both layouts the power losses increase proportionally with the torque request and the speed. The increase of speed leads to a higher power losses increase compared to the one obtained with higher torque demands. It is shown how the omega twin arm tensioner layout leads to higher losses of around $60-80\%$ for any speed and torque operating condition, highlighting therefore the important contribution that bending losses represent for a belt drive system. Higher belt preloads seem not to have a big impact on the power losses increase but mainly contribute in defining the maximum torque loads that can be reached in the power transmission: the maximum transmittable torque defines the loads that can be handled by the drive with admissible levels of belt slip, i.e. lower the 4%.

Efficiency and Power losses Modelling

The measurements on the automatic tensioner layouts were used to establish a modelling procedure for power losses on BDS inspired by the techniques used for tire modelling. Additional tests were performed in no load conditions to verify the robustness of the transmission ratio definition and the deriving belt slip. Fig. 7.11 shows the no-load tests where CS speed ramps from zero to 5000rpm were applied to the transmission system with no braking torque. The CS and alternator speeds and torques were measured during the speed ramp of the CS for different belt preloads.

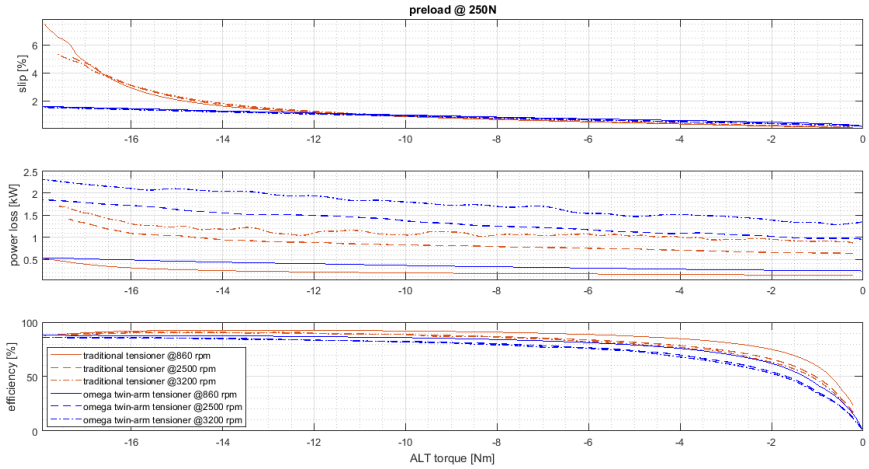

Fig. 7.9 Comparison between quasi-static tests on the traditional automatic tensioner and the twin arm tensioner layouts at a belt preload of $T_0 = 250$N. The cases of constant CS speed at $\omega_{CS} = 860rpm$ (solid line), $\omega_{CS} = 2500rpm$ (dashed line) and $\omega_{CS} = 3200rpm$ (dot-dashed line) are taken into account. The influence of the different layout configuration and speed are highlighted.

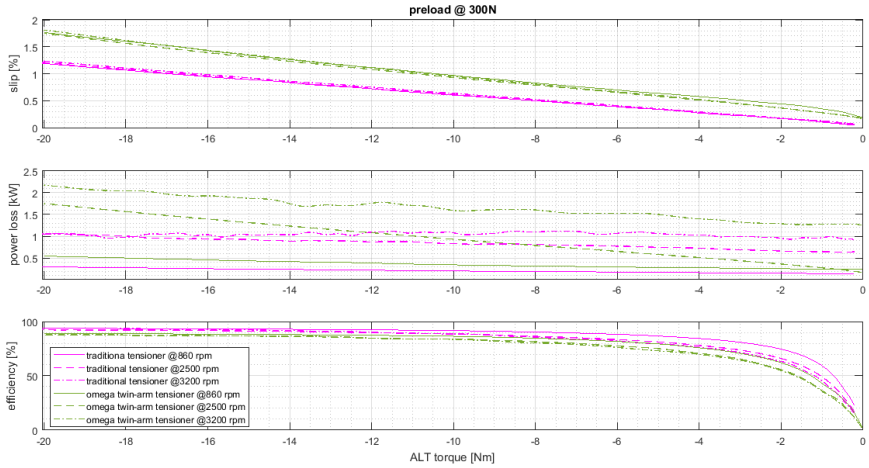

Fig. 7.10 Comparison between quasi-static tests on the traditional automatic tensioner and the twin arm tensioner layouts at a belt preload of $T_0 = 300$N. The case of constant CS speed at $\omega_{CS} = 860rpm$ (solid line), $\omega_{CS} = 2500rpm$ (dashed line) and $\omega_{CS} = 3200rpm$ (dot-dashed line) are taken into account. The influence of the different layout configuration and speed are highlighted.

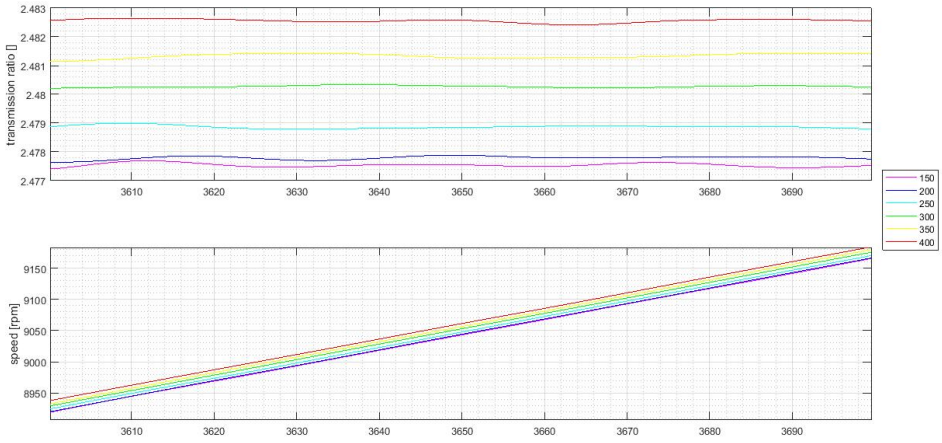

Fig. 7.11 Variation of the transmission ratio for increasing belt preloads. The variation of the transmission ratio highlights the necessity of an empirical definition of the no load BSG speed. For each pretension and each operating speed the transmission ratio is defined as $\tau_\Omega = \Omega_{0ALT}/\Omega_{CS}$.

From the experimental results emerged a dependency of the transmission ratio on the preload conditions of the system and a slip offset between the different preload values. As a result, the geometric formulation of the transmission ratio based on the diameters of the pulleys resulted inadequate for experimental data analysis and the real belt slip definition. A different reference speed Ω_{0ALT} can be defined for each belt pretension as the speed at which the ALT/BSG operates without torque from the crankshaft. Such speed defines an operating point that ideally corresponds to the zero-slip condition of the system. Consequently it is possible to formulate a speed dependant transmission ratio as $\tau_\Omega = \Omega_{0ALT}/\Omega_{CS}$. Moreover, it is possible to estimate the slip value when the alternator speed differs from the reference speed ω_0 as:

$$\sigma_\Omega = 1 - \frac{\Omega_{ALT}}{\Omega_{0ALT}} \tag{7.5}$$

The adoption of this definition corresponds to define the belt slippage locally in correspondence of the specific pulley and not globally with respect to the sole crankshaft pulley. This formulation is the same as the one used for the tire longitudinal slip in vehicle dynamics which is usually defined as the difference between the wheel rim (Ω_0) and the wheel tread (Ω) rotational speeds. It is expressed as a damping element with characteristic $\sigma = \frac{\Omega-\Omega_0}{\Omega_0}$ and it defines the longitudinal tire force $F_x = \psi F_z \sigma$, where ψ is the longitudinal tire characteristic slope in the linear range and F_z is the

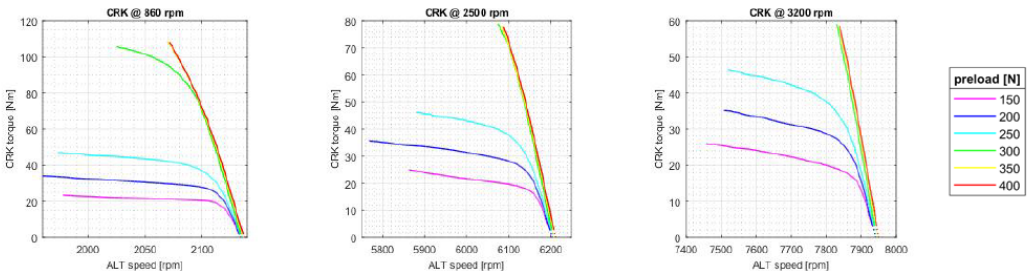

(a) (b) (c)

Fig. 7.12 The crankshaft transmitted torque is represented over the alternator speed for different belt preloads at a crankshaft speed of: (a) $860rpm$; (b) $2500rpm$; (c) $3200rpm$. The alternator speed corresponding to zero torque transmission represents the reference alternator speed Ω_{0ALT} that needs to be used to define the speed dependant transmission ratio as $\tau_\Omega = \Omega_{0ALT}/\Omega_{CS}$ and the local belt slip $\sigma_\Omega = 1 - \frac{\Omega_{ALT}}{\Omega_{0ALT}}$.

vertical tire force.

Fig. 7.12 shows the crankshaft torque transmitted during quasi-static tests on the traditional automatic tensioner layout. In the graphs, the alternator speed corresponding to zero torque transmission represents the reference alternator speed Ω_{0ALT} that needs to be used to define the belt slip. The images show how a different reference alternator speed results from different belt preloads.

Using τ_Ω and σ_Ω it is eventually possible to discriminate the power losses linked to a speed loss contribution and those caused by a torque loss. This formulation derives from expressing the power losses as the algebraic sum between the power provided by the CS and ALT pulleys

$$P_{loss} = C_{CS}\Omega_{CS} + C_{ALT}\Omega_{ALT} \tag{7.6}$$

and assuming the torque losses as constant

$$C_{ALT} = \frac{C_{CS} - C_{CS0}}{\tau_\Omega} \tag{7.7}$$

This assumption corresponds to considering bending and shear losses as more relevant compared to the other contributions. As a result the overall power loss can be expressed as:

$$P_{loss} = C_{CS}\Omega_{CS} + \frac{C_{CS} - C_{CS0}}{\tau_\Omega}\Omega_{ALT} \tag{7.8}$$

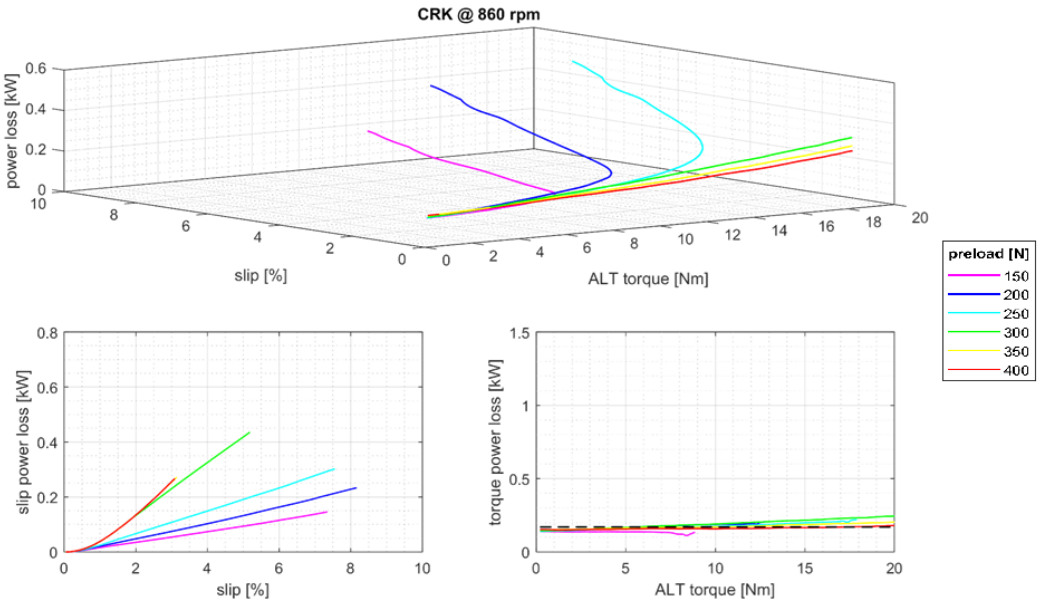

Fig. 7.13 Automatic tensioner layout measurements. Power losses with respect to the local slip σ_Ω and the torque loads applied by the alternator at constant CS speed $\omega_{CS} = 860$rpm. The power loss P_{σ_Ω} increase for increasing slip values. The power losses P_{τ_Ω} due to the transmitted torque are quasi-constant for increasing load values.

$$P_{loss} = \frac{C_{CS0}\Omega_{ALT}}{\tau_\Omega} + \sigma_\Omega C_{CS}\Omega_{CS} = P_{\tau_\Omega} + P_{\sigma_\Omega} \tag{7.9}$$

Figs. 7.13, 7.14 and 7.15 highlight the dependency of the power losses of the system over increasing slip conditions and transmitted torque. The images confirm the assumptions over the power losses behaviour that were done before as the power losses P_{σ_Ω} increase for increasing slip values while the power losses P_{τ_Ω} due to the transmitted torque appear to be quasi-constant for increasing load values.

Using this belt slip definition provided above, it was possible to proceed with a further analysis over the alternator load torque variation. In particular it was studied the ALT load torque dependency over the belt slip with respect to the belt on the contact arc. Similarly to what done to fit the tire forces as function of their longitudinal and side slip, it was possible to describe analytically such mechanism by means of a hyperbolic trigonometric fitting function depending on the slip and the belt preload.

$$C_{BSG} = f_a(T_0)\arctan[f_b(T_0)(\sigma - \sigma_0)] \tag{7.10}$$

where

$$f_a(T_0) = a_3 \sinh[a_2(T_0 + a_1)] + a_0 \tag{7.11}$$

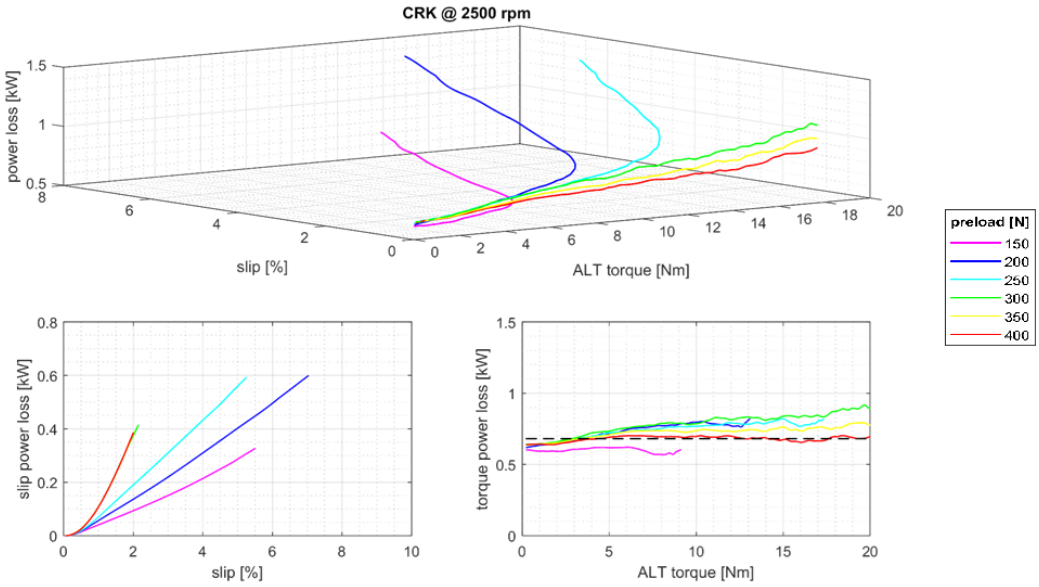

Fig. 7.14 Automatic tensioner layout measurements. Power losses with respect to the local slip σ_Ω and the torque loads applied by the alternator at constant CS speed $\omega_{CS} = 2500$rpm. The power loss P_{σ_Ω} increase for increasing slip values. The power losses P_{τ_Ω} due to the transmitted torque are quasi-constant for increasing load values.

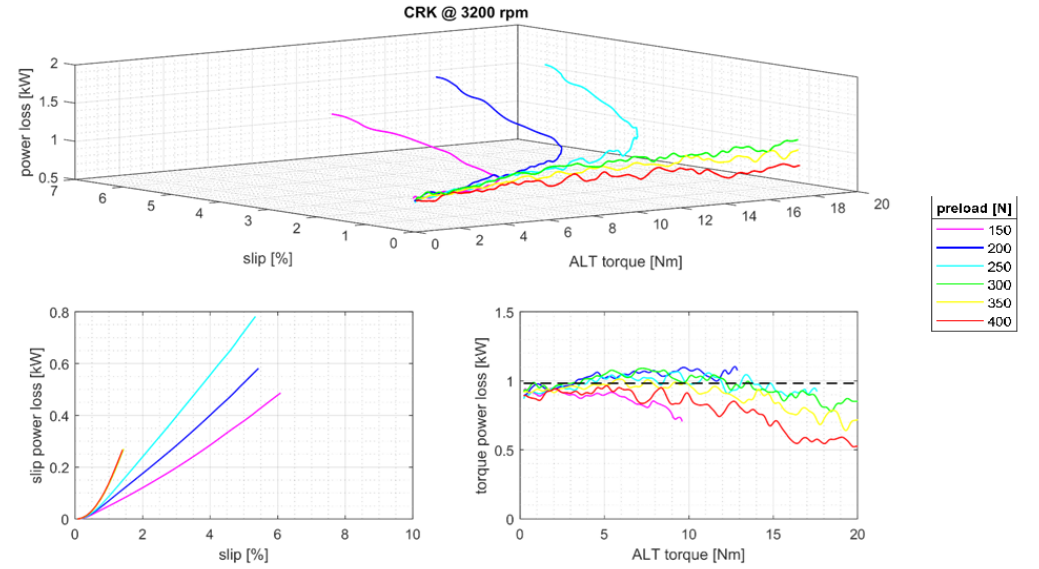

Fig. 7.15 Automatic tensioner layout measurements. Power losses with respect to the local slip σ_Ω and the torque loads applied by the alternator at constant CS speed $\omega_{CS} = 3200$rpm. The power loss P_{σ_Ω} increase for increasing slip values. The power losses P_{τ_Ω} due to the transmitted torque are quasi-constant for increasing load values.

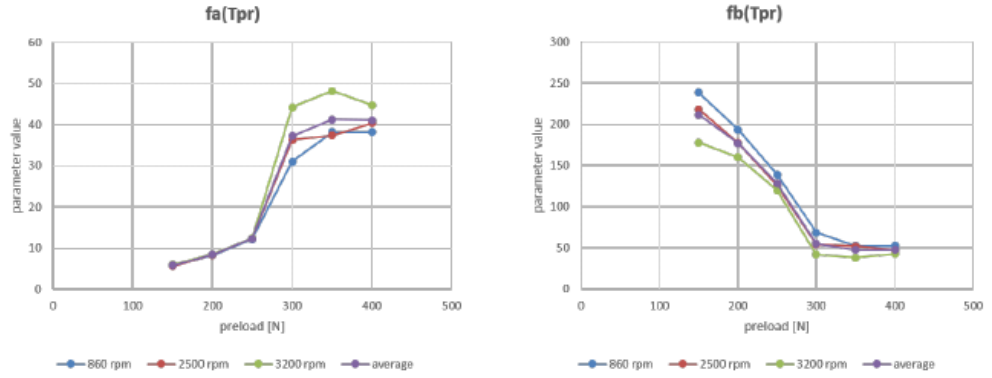

(a) (b)

Fig. 7.16 Fitting of the coefficients (a) f_a and (b) f_b from the average behaviour of the system over the operating conditions considered.

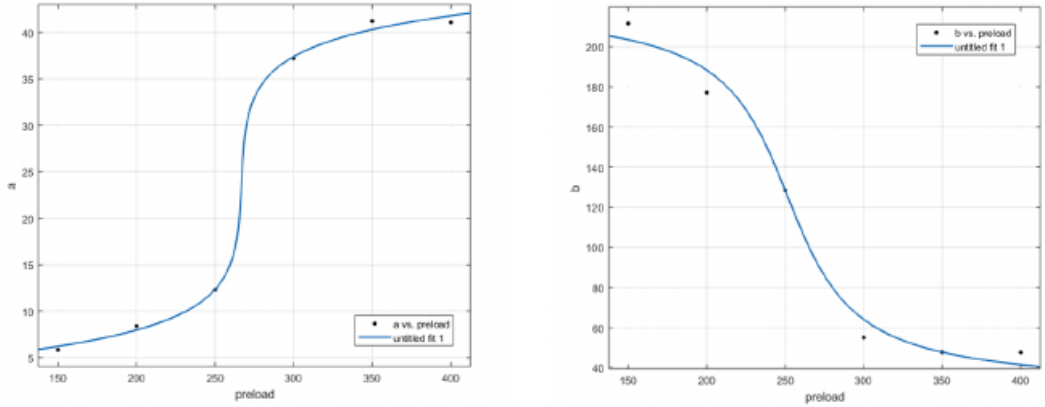

(a) (b)

Fig. 7.17 Fitting of the coefficients (a) f_a and (b) f_b refined by means of a constrained active-set minimization algorithm applied to the H2 norm of the error between the fit and all the masured data points

$$f_b(T_0) = b_3 \sinh[b_2(T_0 + b_1)] + b_0 \tag{7.12}$$

In 7.10 the coefficients f_a and f_b depend on the belt preload T_0. Figs. 7.16 and 7.17 shows the fitting procedure of the coefficients f_a and f_b defined in equations 7.11 and 7.12. After an initial function fit from the average behaviour of the system over the operating conditions considered, a refinement was performed by applying a constrained active-set minimization algorithm to the H2 norm of the error between the fit and all the measured data points.

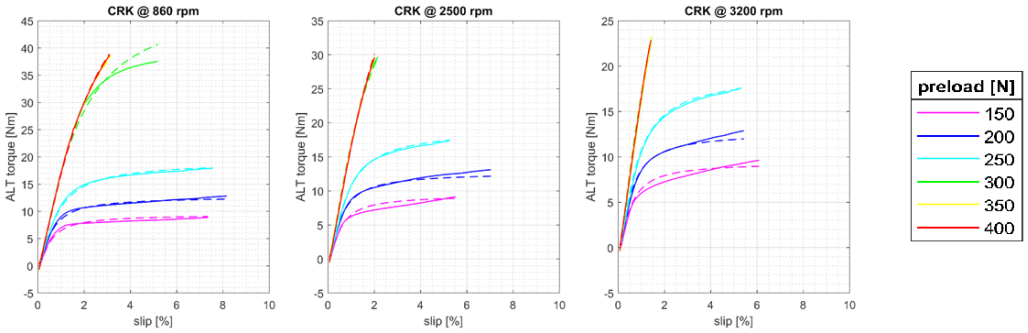

Fig. 7.18 Comparison between the numeric results obtained by the fitted function and the experimental results.

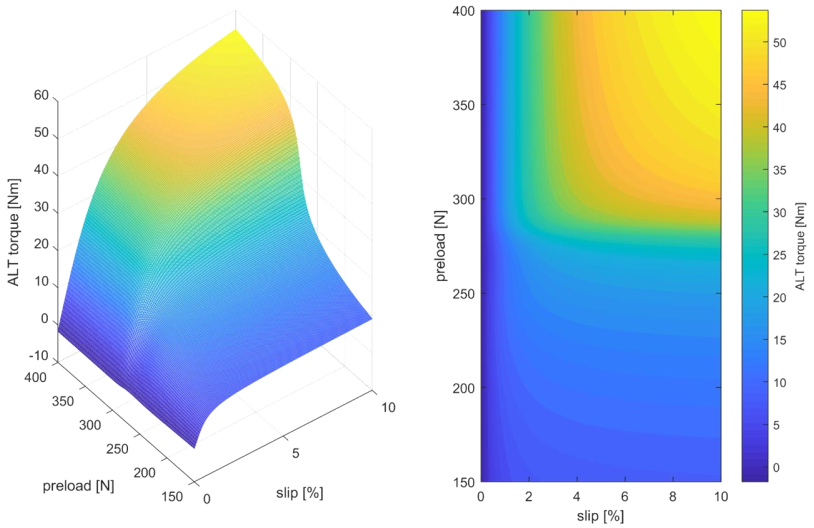

Fig. 7.19 3D representation of the maximum transmittable torque over increasing belt pretension and belt slip according to the fitting function.

In conclusion, Fig. 7.18 depicts a comparison between the numerical results obtained by the fitted function and the experimental results. It emerges how this behaviour is speed independent and it is therefore the same in all the three speed operating conditions analysed. A good agreement can be found. In Fig. 7.19 the final general 3D representation is depicted. This representation highlights the existence

of an acceptance boundary for what concerns the belt preloads: below the value of $T_0 = 300$N the maximum transmittable torque is equal or lower then 10Nm; when this boundary is overcome the maximum transmittable torque reaches values higher then 30Nm. In other words, $T_0 = 300$N is the minimum tension that allows the system to function.
The described procedure was proven for the case of the traditional automatic tensioner layout and is generally applicable to any tensioning drive system.

Functionality of the Omega Twin-Arm Tensioner

The tests that were performed on the omega twin arm tensioner layout were additionally used to evaluate the static functionality of the tensioning device. With this goal the measurements of the angular displacements of the tensioner arms and the belt tension on the tight and slack spans were recorded and analysed. The following set of tests was considered in order to fully represent the drive operating conditions:

1. $\hat{C}_{\text{bsg}} = +30$ Nm, $\omega_{\text{cs}} = 860$ rpm, motor mode
2. $\hat{C}_{\text{bsg}} = +30$ Nm, $\omega_{\text{cs}} = 2500$ rpm, motor mode
3. $\hat{C}_{\text{bsg}} = -30$ Nm, $\omega_{\text{cs}} = 2500$ rpm, generator mode
4. $\hat{C}_{\text{bsg}} = -17$ Nm, $\omega_{\text{cs}} = 3800$ rpm, generator mode

In the first two conditions, the BSG boosts the BDS. In a vehicle, this boost feature is attractive at low engine regimes to deliver a short but fast acceleration. By converse, in the last two conditions, the BSG behaves as a generator that brakes the transmission. At high engine speeds, regenerative braking is desirable to recover part of the mechanical power in the front end accessory drive. Due to power limitations of the BSG machine, the test at 3800 rpm reaches a lower peak torque of -17 Nm.
Considering tests that were executed at different speeds is important to prove the validity of the static model, where the speed component and the friction effects associated to it are neglected.
Furthermore, the tests at mid speed (2500 rpm) span torque values in motor and generator modes. They are useful to highlight the dual behaviour provided by the tensioner. Figure 7.20 shows the experimental results collected in the four chosen

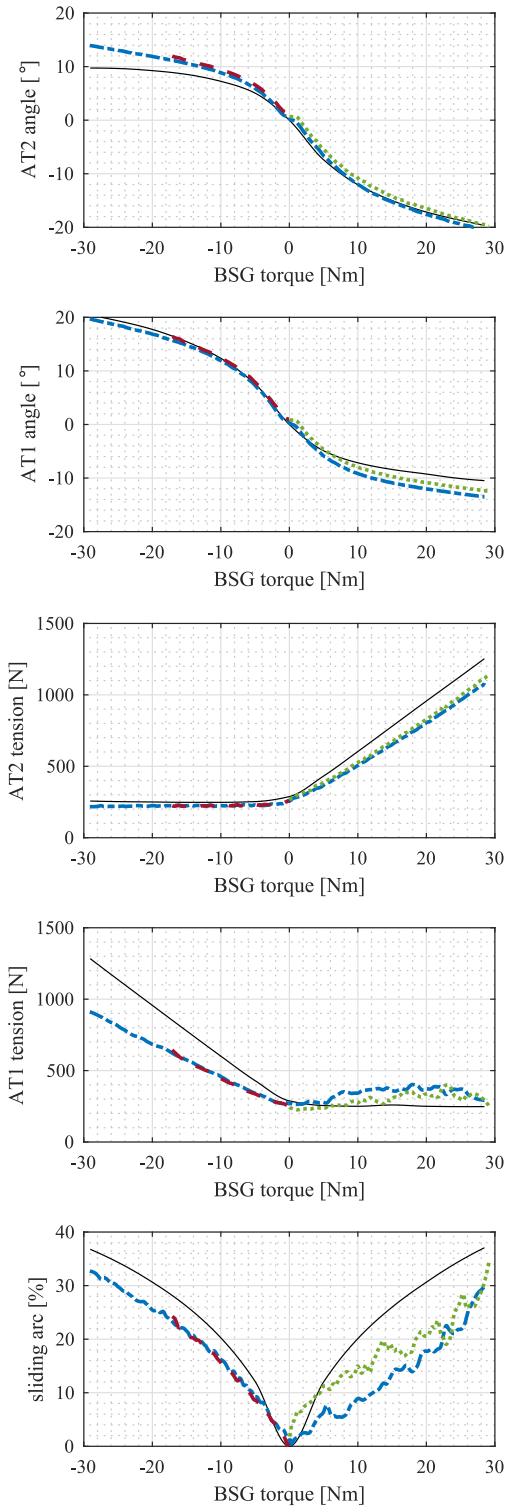

Fig. 7.20 Results of a twin arm tensioning device working on a BSG-based BDS in motor and generator modes. The considered variables are the angular displacement of the tensioner pulleys, the belt span tensions and the sliding arc on the BSG pulley. Numerical results (solid) are compared to experimental data obtained at 860 rpm (dot), 2500 rpm (dash-dot) and 3800 rpm (dash).

testing conditions. It exhibits the two tensioner arm angular displacements relative to their position at rest, the span tensions and the BSG sliding arc relative to its wrap angle. Furthermore, the data from the static model that was introduced in Chapter 5 are also presented. These numerical results are obtained by solving the model with BSG torque values ranging from -30 to 30 Nm. The sliding arc on the BSG pulley is calculated for both numerical and experimental cases according to Eq. 5.17.
Numerical and experimental results highlight the behaviour of the twin arm tensioner, which is capable to obtain comparable performances in both generator and motor modes.
In motor mode, the belt span on the pulley AT2 exhibits a tension directly proportional to the BSG torque. As this torque increases, it is seen that both arm angles tend to rotate in a negative (clockwise) direction. The arm with the pulley AT2 follows a larger displacement, thus yielding the aperture of the tensioner and a deflection of its spring. Additionally, the tension of the belt span facing the pulley AT2 has a linear increase with respect to the motor torque. In contrast the tension of the AT1 side stays within 80% of the pretension value.
In generator mode, a similar behaviour occurs, but the roles of AT1 and AT2 are inverted. Both arms rotate counter-clockwise and the aperture of the tensioner increases as the braking torque increases.
As expected from Euler's formula (Eq. 5.17), the sliding arc is symmetric with respect to the ordinate axis. The maximum observed sliding arc assumes a value of 40.5%. Hence, the system works in a stable slip-safe condition.
The experimental results at different speeds practically overlap with each other in both modes. This is an important aspect that allows to neglect speed losses for the representation of the tensioner behaviour in quasi-static conditions.
Some considerations must be made to better understand the existing differences between numerical and experimental results. The measurement of the belt tensions is indirect, as it goes through the measurement of the hub loads exerted by the belt on the shafts of the two idler pulleys. The belt tension is then calculated by the inverse of Eq 5.3. Therefore, the belt tension is inversely proportional to the sine of half the idler wrap angle: small angles will inevitably lead to large measurement errors. This situation is particularly observed for the belt tension acting on AT1. Focusing on the layout drawn in Figs. 5.4 and 6.6 and the results provided in Fig. 7.20, it is clear how the small wrap angle insisting on the idler IDL1 has a detrimental effect on the evaluation of the tension of its belt span. This negative effect becomes more evident

in motor mode, where it also affects the evaluation of the BSG sliding arc.
Besides these observations, numerical and experimental results show an acceptable agreement that confirms the functionality of the twin arm tensioner.

7.2 Dynamic Analysis

Dynamic tests were performed on both the BDS layouts considered. For what concerns the traditional automatic tensioner layout, the focus was to identify the resonance frequencies of the transmission and comparing the experimental results with the performed simulations. The experimental measurements were compared both with the Simulink model that was built following the guidelines of Chapter 5 and with a Simdrive model replicating the same layout. The choice of focusing on the traditional automatic tensioner layout was done to simplify the analysis of the tensioner dynamics.
For what concerns the omega twin-arm tensioner layout, the goal was to further highlight the symmetric behaviour of the omega twin-arm tensioner and to test the system stability when facing high impulsive torque loads. In this phase, the focus was the transient response of the tensioner to the application of high values of BSG torque, positive or negative. The evaluation of the time delay and the overshoot of the tensioner response in terms of tensioner arms displacements was therefore performed.

7.2.1 Traditional Automatic Tensioner Layout

Tests are performed keeping a constant speed on the crankshaft axis and applying an oscillating torque through the ALT motor varying in frequency. The detailed tests performed are the following:

- $\omega_{CS} = 860$rpm with $C_{ALT} = -5 + 2\sin(2\pi ft)$, with $f = [0.1 - 40]$Hz
- $\omega_{CS} = 860$rpm with $C_{ALT} = -10 + 5\sin(2\pi ft)$, with $f = [0.1 - 40]$Hz
- $\omega_{CS} = 860$rpm with $C_{ALT} = -15 + 5\sin(2\pi ft)$, with $f = [0.1 - 40]$Hz

Both speed and torque values are measured on CS and ALT pulleys.

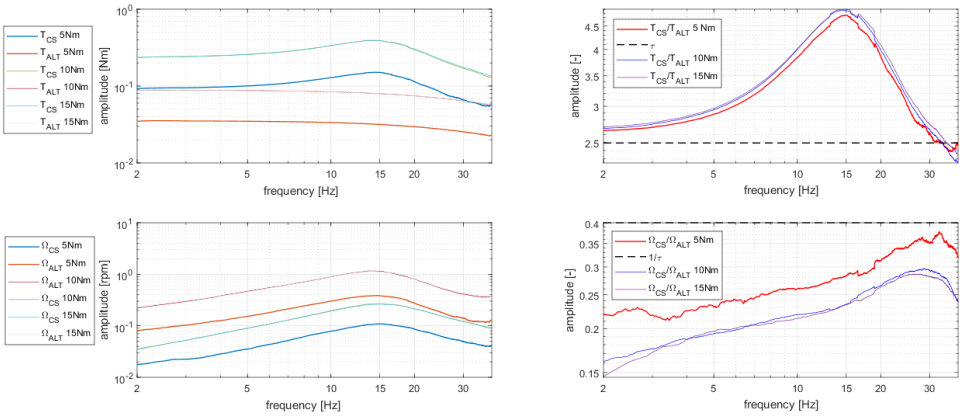

Fig. 7.21 Experimental results in terms of torque and speed values in the frequency domain

Results

Fig. 7.21 shows the results in the frequency domain of the experimental measurements for the three ALT torque loads considered. These need to be compared to Figs. 5.21 and 5.22 in Chapter 5. The real system features the resonance at a frequency of around 15Hz, which is slightly lower then the one predicted by the Simulink model, placed at 20Hz. For different torque loads both the experimental and Simulink results identify the same resonance frequency,while the Simdrive model provides a frequency of 20Hz for high torques and a higher frequency in the case of 5Nm, i.e. 25Hz. Fig. 7.22 shows speed and torque values of the CS and ALT pulleys in the time domain for the experimental system. It is possible to notice how the reference speed on the crankshaft that was intended to be constant and equal to $\omega_{CS} = 860$rpm in the case of the real system features an oscillation. Such oscillation is in phase with the one provided to the system by the ALT torque and is due to a filtering issue on the speed-controller of the CS electric motor that was not able to keep the constant reference value. This fact results in an oscillation absorption from the CS point of view that attenuates the resonant behaviour of the transmission and tends do move the resonance frequency at a lower value. An additional discrepancy can be found between both the models and the experimental test in terms of amplitude values of speed and torque values. To further investigate on the differences between measurements and simulations it is useful to consider the plots in the time domain: Fig. 7.22 depicts the speed and torque inputs and outputs of the system for what the experimental tests are concerned in the case of $C_{ALT} = 15 + 5\sin(2\pi ft)$ with

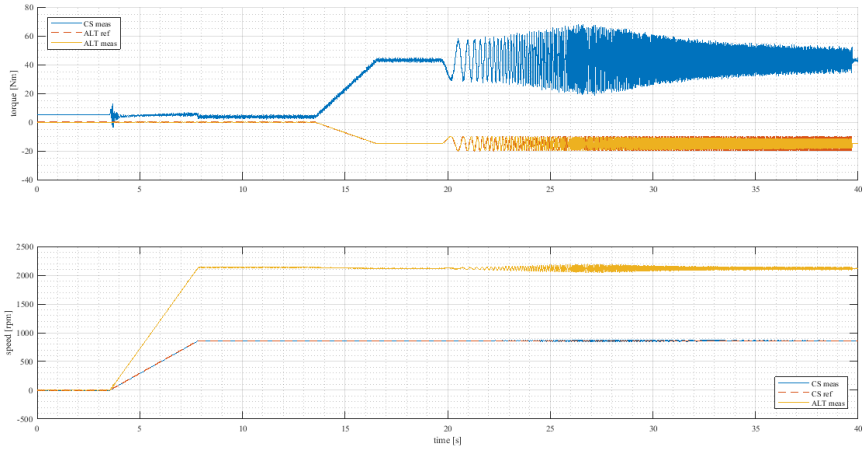

Fig. 7.22 Dynamic behaviour of the real system in the time domain

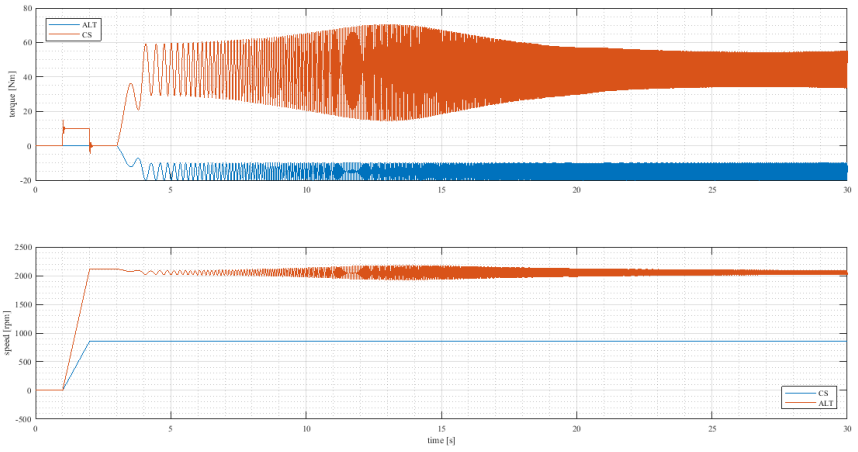

Fig. 7.23 Dynamic results of the Simulink model in the time domain

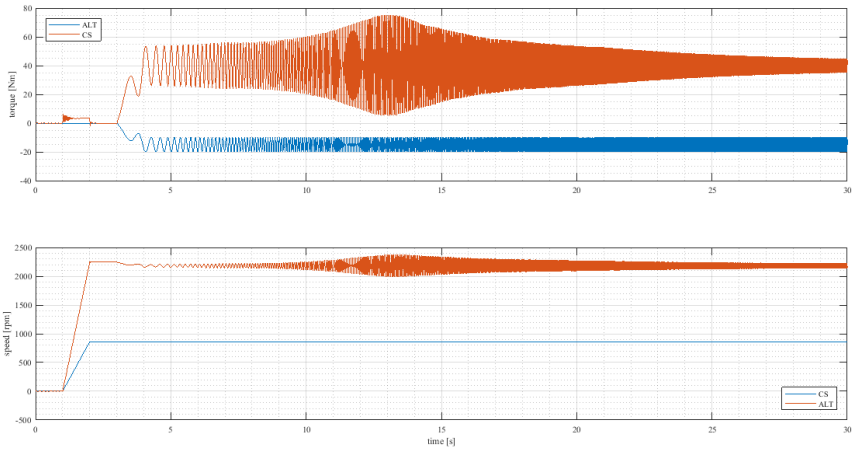

Fig. 7.24 Dynamic results of the Simdrive model in the time domain

$f = [0.1 - 40]$Hz; Fig. 7.23 and 7.24 show the same values for the two models. The amplitude difference between experimental results and simulations can be attributed to two contributions. In the first place, regarding at the results in terms of both torques and speeds, it can be noticed an offset between the experimental measurements and the two simulation results. This offset is present also in no-load conditions, that are represented by the two models as zero torque zones for both the models whereas the experimental measurements highlight an offset of $C_{CS} = 5$Nm. This torque loss is due to the bending losses contribution that was highlighted in the previous section and to the friction effects in the bearings that were neglected in the modelling process. This discrepancy between the model environment and the real system is clear also in the analysis in the frequency domain where the torques ratio is taken into account. In a second place, as it resulted from the static analysis previously performed, the transmission ratio of the drive is load-dependant as the belt tension of installation and the torque load on the specific pulley define the position of the power transmission cord of the belt in the pulley ribs. This phenomenon is due to two main contributions to the speed losses of the system which are strictly related one to the other, on one side the rubber compliance effect and on the other side the losses due to the shear deflections in the rubber layer: the position of the transmission cord determines the quantity of belt material affected by shear and affects the position of the resonance frequency of the system. As it was demonstrated in [50], the shear deformation of the belt is dominant in the definition of the first torsional mode of the transmission.

7.2.2 Omega Twin-Arm Tensioner Layout

A constant speed is applied by the crankshaft motor and the BSG motor requests steps of torque.
Before the experiments, the belt pretension is set to the desired value. This force is verified with a CLAVIS type 6 belt tension meter. In each test, the crankshaft speed ω_{cs} is fixed to a constant value. Then, a torque step is applied with the BSG to load the system. The sign of this torque defines whether the BSG operates as a motor $(+)$ or as a generator $(-)$. The tensioner arm angles and the belt slip on the BSG pulley are measured for each testing condition.
The following conditions were tested:

1. $\hat{C}_{\text{bsg}} = +25$ Nm, $\omega_{\text{cs}} = 2500$ rpm, $T_0 = 294$N motor mode
2. $\hat{C}_{\text{bsg}} = +25$ Nm, $\omega_{\text{cs}} = 2500$ rpm, $T_0 = 234$Nmotor mode
3. $\hat{C}_{\text{bsg}} = -25$ Nm, $\omega_{\text{cs}} = 2500$ rpm, $T_0 = 294$N generator mode
4. $\hat{C}_{\text{bsg}} = -25$ Nm, $\omega_{\text{cs}} = 2500$ rpm, $T_0 = 234$N generator mode

Results

Figs. 7.25 and 7.26 represent the experimental results obtained for both alternator and motor modes.
The two images show the movement of the two tensioner arms for a corresponding BSG torque applied for different tensioning conditions. With different belt pretensions, the system features the same dynamic characteristics, showing the same time rise $t_r = 0.08s$ and overshoots $s_{\%} = 20\%$ on the right pulley and $s_{\%} = 43.75\%$ on the left pulley for negative torques, and time rise $t_r = 0.04s$ and overshoot $s_{\%} = 22.2\%$ on the right pulley and $s_{\%} = 45\%$ for positive torques. These values show higher movements for the tensioner pulley placed on the tight span in alternator mode. A higher belt pretension leads to a smaller aperture of the two tensioner arms in both alternator and motor modes.

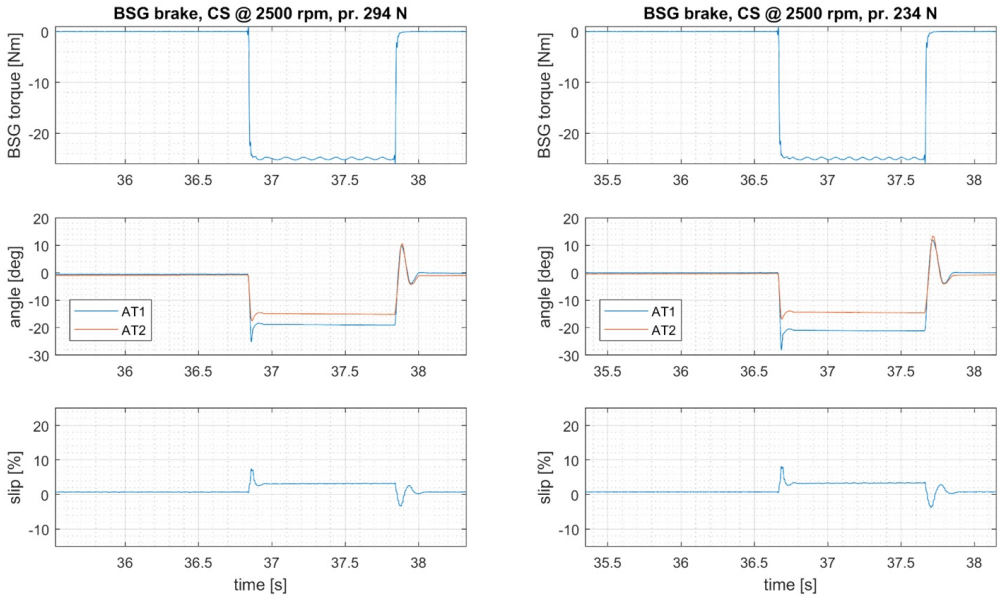

Fig. 7.25 Dynamic behaviour of a twin arm tensioner in alternator mode. The BSG torque, the angular displacements of the two tensioner arms and the corresponding belt slip calculated on the BSG pulleys are depicted.

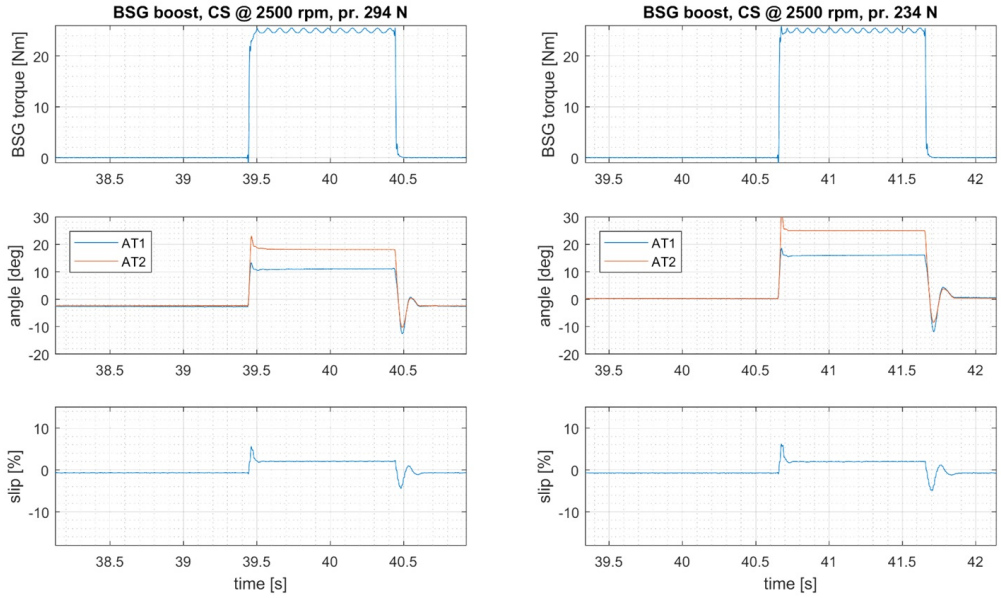

Fig. 7.26 Dynamic behaviour of a twin arm tensioner in motor mode. The BSG torque, the angular displacements of the two tensioner arms and the corresponding belt slip calculated on the BSG pulleys are depicted.

7.3 Chapter Conclusions and Remarks

This Chapter included all the experimental activity that was conducted in the context of this thesis. The overall goal was to provide a thorough understanding of the efficiency and dynamic mechanisms that affect an automotive front end accessory drive. A quasi-static analysis of both a traditional automatic tensioner layout and a BSG-based BDS layout for micro-hybrid applications featuring an omega twin arm tensioner allowed to highlight the consequences on the system performances when adopting the two solutions. A data fitting process was shown for the characterization and prediction of the system power losses behaviour for varying belt tensions and BSG loads. The twin-arm tensioner was further investigated to highlight its symmetric characteristics and the experimental results allowed to validate the analytical static model that was proposed in Chapter 5. Eventually a lumped-parameters dynamic model of the traditional automatic tensioner layout was compared with both the experimental measurements on the real layout and a multi-body model built using a commercial software. A good accordance between experiments and models was found. The model that was proposed in [50] was therefore extended to the case of a real front end accessory drive and validated.

Chapter 8

Conclusions

The research activity that was described in this thesis investigated the power losses mechanisms in BDS and the behaviour of BDS in micro-hybrid applications.
The analysis of the state of the art allowed to identify the main contribution of power losses that are of highest importance in static and dynamic conditions in the case of an automotive front end accessory drive. On one hand the literature review concluded that the torque losses are expected to have the highest influence on the power transmission efficiency. On the other hand speed losses need to be considered when dealing with the dynamic behaviour of the drive.
Following these guidelines the research focused on the modelling and experimental investigation of both the static and dynamic behaviour of FEAD and got deeper into the consideration of a BSG-based BDS equipped with an omega twin-arm tensioner. In order to support the investigation with a proper and reliable testing facility a process of concept, design, production and functional set-up of a dedicated test rig for the reproduction of different BDS layouts was carried out.
The experimental activity carried out to investigate the transmission efficiency in quasi-static conditions focused on two BDS layouts, one equipped with a traditional automatic tensioner and one featuring an omega twin-arm tensioner. The comparison of the two layouts in the so-called alternator mode led to the following main conclusions:

1 The traditional automatic tensioner studied is capable of facing high torque demands and can be optimized with BSG applications focused on the alternator mode

2 By converse, the adoption of an omega twin-arm tensioner leads to higher power losses at any speed or preload tension and to a lower transmission efficiency for any torque load applied by the alternator. As a result, there is no effective advantage in adopting an omega twin-arm tensioner in this operating condition. This is due to the higher torque losses affecting the system that result from the increased complexity of the serpentine drive

Based on the analysis of the experimental measurements obtained on the traditional automatic tensioner layout a modelling procedure of the belt-pulley contact inspired on the techniques used for tire modelling was defined to represent the power losses phenomena affecting the power transmission based on the following observations:

3 The transmission ratio of the drive is load-dependant as the belt tension of installation and the torque load on the specific pulley define the position of the power transmission cord of the belt in the pulley ribs. This phenomenon is to be conducted to the so-called rubber compliance speed loss contribution and leads to the need for the definition of a pulley specific reference speed and a corresponding pulley specific slip

4 The maximum transmittable alternator torque can be described by means of a hyperbolic trigonometric function depending on the belt slip and preload. This representation allows to identify the minimum acceptable preload for a proper transmission functioning

5 Representing the system power losses as function of the belt slip and the torque loads, the experimental measurements showed how the increase of power losses mainly depends on the belt slip increase and is almost independent from increasing torque loads. Considering different belt preloads, it is additionally observed that low preloads correspond to a loss behaviour dominated by speed-related power losses P_{σ_Ω}. By converse, high preloads present a predominant portion of torque-related power losses P_{τ_Ω}.

The further analysis of the omega twin-arm tensioner in a BSG-based BDS led to the following main findings:

6 The symmetry of this tensioning device when combined with a symmetric lay-out geometry allows to face both positive and negative high torque loads from

the BSG side. The corresponding performances result therefore symmetric for what concerns the alternator and motor modes of a BSG-based BDS

7 The layout geometry affects the drive behaviour for different belt preloads. The layout that was experimentally investigated in this research activity had a slight asymmetry that resulted is an unbalanced distribution of the power losses wrt BSG torque loads. Low preloads correspond to the highest power losses in alternator mode and to the lowest in motor mode. By converse high belt preloads lead to lower power losses in alternator mode and higher in motor mode. In the case of asymmetric layout, the set of the belt preload needs therefore to be optimized considering the desired operating strategy of the drive

8 The analytical model of the static behaviour of the omega twin-arm tensioner that was proposed in Chapter 5 was proved to be valid and can be a useful and meaningful design tool for the performances prediction of such system

The dynamic analysis focused on the identification of the resonance frequency of the traditional BDS layout and on the validation of the corresponding analytical model. The resulting main outcomes were the following:

9 A good accordance was found between experimental measurements and simulation results. The model proposed in [50] was extended and validated for the case of a real front end accessory drive and the influence of the shear deformations on the identification of the first modes of rotational vibrations was shown.

Eventually, a last set of tests was performed with the goal of investigating the omega twin-arm tensioner stability to the application of high impulsive torque loads. These experiments showed that:

10 The omega twin-arm tensioner shows a good stability when facing high impulsive loads and the same transient behaviour is obtained for positive and negative torques and for different belt preloads.

11 The influence of the belt preload on the transient behaviour of the omega twin-arm tensioner can be observed on the relative motion of the two tensioner

arms. A higher preload leads to smaller relative movements between the two tensioner arms.

All in all, it is possible to conclude that the performed research activity led to the definition of relevant testing and modelling methodologies for the analysis and optimization of BSG-based BDS. The design of a dedicated test rig allowed to characterize the behaviour of different BDS in controlled laboratory environment and compare their measurement results with the corresponding models.

References

[1] Radu Bojoi, Andrea Cavagnino, Marco Cossale, and Alberto Tenconi. Multiphase starter generator for a 48-v mini-hybrid powertrain: Design and testing. *IEEE Transactions on Industry Applications*, 52(2):1750–1758, 2016.

[2] James E Walters, Ronald J Krefta, Gabriel Gallegos-Lopez, and Gerald T Fattic. Technology considerations for belt alternator starter systems. Technical report, SAE Technical Paper, 2004.

[3] Manfred Arnold and Mohamad El-Mahmoud. A belt-driven starter-generator concept for a 4-cylinder gasoline engine. *AutoTechnology*, 3(3):64–67, 2003.

[4] Wen-Bin Shangguan and Xiao Feng. Design of isolation pulley in front of crankshaft to reduce vibrations of front end accessory drive system. Technical report, SAE Technical Paper, 2015.

[5] Lionel Manin, Régis Dufour, and Sébastien Schultz. Pulley torsional vibration damper characterization. *Mechanics & Industry*, 14(2):151–155, 2013.

[6] J Xu and J Antchak. New technology to improve the performance of front end accessory drive system. Technical report, SAE Technical Paper, 2004.

[7] Xiang-kun Zeng and Wen-Bin Shangguan. Modelling and optimisation dynamic performances for an engine front end accessory drive system with overrunning alternator decoupler. *International Journal of Vehicle Noise and Vibration*, 8(3):261–274, 2012.

[8] Adebukola O Olatunde. *DESIGN & ANALYSIS OF A TENSIONER FOR A BELT-DRIVEN INTEGRATED STARTER-GENERATOR SYSTEM OF MICRO-HYBRID VEHICLES*. PhD thesis, University of Toronto, 2008.

[9] Adebukola Olatunde and JW Zu. Optimization of twin tensioner performance in a belt-driven integrated starter-generator system for micro-hybrids. In *Proceedings of the ASME 2009 International Design Engineering Technical Conferences & Computers and Information in Engineering Conference*, volume 8, pages 951–957, 2009.

[10] G. Cariccia, F.D. Licata, and E. Noe. Actuated tensioner for an accessory drive, 2013. WO Patent App. PCT/IB2013/055,123.

[11] B. Pitaud. System de mise sous tension d'une courroie, September 2010. FR Patent Publ. No. 2 956 889.

[12] A. Serkh. Dual linear belt tensioner, September 2008. US Patent App. No. 09/969,341.

[13] A. Imtiaz, L. Keming, and H. Dave. Accessory and motor/generator belt drive tensioner, April 2002. US Patent App. No. 09/969,205.

[14] T. Di Giacomo and H. Lemberger. Two-arm belt tensioner, 2004. Patent No. EP 1 464 871 A1.

[15] A.L. Bartos and L.O. Hewko. Automatic belt tensioner for vehicle combined starter-generator, 1988. Patent No. 4,758,208.

[16] J. Harvey, O. Stegelmann, A. Martinez, J Dilthey, and C. Haenbeukers. Orbital tensioner, 2015. US 2015/0308545 A1.

[17] W Ingo. Orbital tensioner assembly, 2015.

[18] J Antchak, G Ryeland, and R Farewell. Endless drive arrangement for hybrid vehicle using two-armed tensioner with non-orbiting arms, 2016.

[19] J. Jud and M. Jung. Riemenspannvorrichtung für starter-generator-anwendung, August 2011. EP Patent Appl. No. 09006897.4.

[20] J Jud and M Jung. Belt tensioning device for being used with a starter generator, 2014.

[21] S. Mack, A. Reichert, C. Hauck, B. Hartmann, and H. Bauer. Tensioning device for a traction mechanism drive of an internal combustion engine, 2015. US 9,182,015 B2.

[22] TF Chen, DW Lee, and Cheng-Kuo Sung. An experimental study on transmission efficiency of a rubber v-belt cvt. *Mechanism and machine theory*, 33(4):351–363, 1998.

[23] László Kátai and István Szabó. Identification of v-belt power losses with temperature measurement. *Journal of Mechanical Science and Technology*, 29(8):3195–3203, 2015.

[24] SE Bechtel, S Vohra, KI Jacob, and CD Carlson. The stretching and slipping of belts and fibers on pulleys. *Journal of Applied mechanics*, 67(1):197–206, 2000.

[25] B Göran Gerbert. Some notes on v-belt drives. *ASME J. Mech. Des*, 103(1):8–18, 1981.

[26] BG Gerbert. Power loss and optimum tensioning of v-belt drives. *Journal of Engineering for Industry*, 96(3):877–885, 1974.

[27] GG Gerbert. Paper xii (i) on flat belt slip. *Tribology Series*, 18:333–340, 1991.

[28] G Gerbert. Belt slip–a unified approach. *Journal of Mechanical Design*, 118(3):432–438, 1996.

[29] T Childs and D Cowburn. Power transmission losses in v-belt drive part 1: Mismatched belt and pulley groove wedge angle effects. In *Proceedings of International Mechanical Engineers*, volume 201, pages 33–40, 1987.

[30] T Childs and D Cowburn. Power transmission losses in v-belt drives part 2: effects of small pulley radii. *Proceedings of the Institution of Mechanical Engineers, Part D: Transport Engineering*, 201(1):41–53, 1987.

[31] KI Gervas and BA Pronin. Calculation of power losses in belt drives. *RUSSIAN ENGINEERING JOURNAL-USSR*, 47(3):26, 1967.

[32] Lionel Manin, Guilhem Michon, Didier Remond, and Régis Dufour. From transmission error measurement to pulley–belt slip determination in serpentine belt drives: Influence of tensioner and belt characteristics. *Mechanism and Machine Theory*, 44(4):813–821, 2009.

[33] Berna Balta, Fazil O Sonmez, and Abdulkadir Cengiz. Speed losses in v-ribbed belt drives. *Mechanism and Machine Theory*, 86:1–14, 2015.

[34] Berna Balta, Fazil O Sonmez, and Abdulkadir Cengiz. Experimental identification of the torque losses in v-ribbed belt drives using the response surface method. *Proceedings of the Institution of Mechanical Engineers, Part D: Journal of Automobile Engineering*, 229(8):1070–1082, 2015.

[35] L Bertini, L Carmignani, and F Frendo. Analytical model for the power losses in rubber v-belt continuously variable transmission (cvt). *Mechanism and Machine Theory*, 78:289–306, 2014.

[36] M Leonard Euler. Remarques sur l'effect du frottement dans l'equilibre. *Mem. Acad. Sci*, 18:265–278, 1762.

[37] DG Alciatore and AE Traver. Multipulley belt drive mechanics: creep theory vs shear theory. 1995.

[38] O Reynolds. Creep theory of belt drive mechanics. *The Engineer*, 38(396), 1847.

[39] Franz Grashof. *Theoretische maschinenlehre*, volume 3. L. Voss, 1890.

[40] MB Rubin. An exact solution for steady motion of an extensible belt in multipulley belt drive systems. *Journal of Mechanical Design*, 122(3):311–316, 2000.

[41] HW Swift. Power transmission by belts: An investigation of fundamentals. *Proceedings of the Institution of Mechanical Engineers*, 115(1):659–743, 1928.

[42] TC Firbank. Mechanics of the belt drive. *International Journal of Mechanical Sciences*, 12(12):1053–1063, 1970.

[43] H Belofsky. On the theory of power transmission by a flat, elastic belt. *Wear*, 25(1):73–84, 1973.

[44] H Kim, K Marshek, and M Naji. Forces between an abrasive belt and pulley. *Mechanism and machine theory*, 22(1):97–103, 1987.

[45] MJ Leamy and TM Wasfy. Analysis of belt-driven mechanics using a creep-rate-dependent friction law. *TRANSACTIONS-AMERICAN SOCIETY OF MECHANICAL ENGINEERS JOURNAL OF APPLIED MECHANICS*, 69(6):763–771, 2002.

[46] Lelio Della Pietra and Francesco Timpone. Tension in a flat belt transmission: experimental investigation. *Mechanism and Machine Theory*, 70:129–156, 2013.

[47] Lelio Della Pietra and Francesco Timpone. Grashof o firbank?–indagine sperimentale su una trasmissione a cinghia piana. In *AIMETA National Congress, Bologna 12th–15th Sept. 2011*, 2011.

[48] Vlado A Lubarda. The mechanics of belt friction revisited. *International Journal of Mechanical Engineering Education*, 42(2):97–112, 2014.

[49] Vlado A Lubarda. Determination of the belt force before the gross slip. *Mechanism and Machine Theory*, 83:31–37, 2015.

[50] Andrea Tonoli, Nicola Amati, and Enrico Zenerino. Dynamic modeling of belt drive systems: effects of the shear deformations. *Journal of vibration and acoustics*, 128(5):555–567, 2006.

[51] Lionel Manin, Cédric Lorenzon, and Xiaokai Liang. Power losses prediction in poly-v belt transmissions: application to front engine accessory drives. In *International Gear Conference 2014*, volume 2, pages pp–1162. Woodhead publishing, 2014.

[52] CAF Silva, L Manin, E Besnier, D Remond, MA Andrianoely, and RG Rinaldi. Modelling of power losses in poly-v belt transmissions: Influence of design parameters. In *Power Transmissions: Proceedings of the International Conference on Power Transmissions 2016 (ICPT 2016), Chongqing, PR China, 27-30 October 2016*, page 373. CRC Press, 2016.

[53] Carlos AF Silva, Lionel Manin, Renaud G Rinaldi, Didier Remond, Etienne Besnier, and Marie-Ange Andrianoely. Modeling of power losses in poly-v belt transmissions: Hysteresis phenomena (enhanced analysis). *Mechanism and Machine Theory*, 121:373–397, 2018.

[54] KJ Gervas. Determining the power losses in v-belt drives during flexure. *Soviet Rubber Technology*, 28(2):42, 1969.

[55] JD Micklem, DK Longmore, and CR Burrows. Belt torque loss in a steel v-belt continuously variable transmission. *Proceedings of the Institution of Mechanical Engineers, Part D: Journal of Automobile Engineering*, 208(2):91–97, 1994.

[56] H Hansson. Geometry conditions for good power capacity in a v-ribbed belt drive. *Journal of Mechanical Design*, 112(3):437–441, 1990.

[57] B Göran Gerbert. Pressure distribution and belt deformation in v-belt drives. *Journal of Engineering for Industry*, 97(3):976–982, 1975.

[58] D Yu, THC Childs, and KW Dalgarno. V-ribbed belt design, wear and traction capacity. *Proceedings of the Institution of Mechanical Engineers, Part D: Journal of Automobile Engineering*, 212(4):333–344, 1998.

[59] Lionel MANIN, Cédric LORENZON, and Houssem SAAD. Efficiency of a two pulleys poly-v belt transmission, influence of belt characteristics: Friction coefficient, longitudinal stiffness. In *The Proceedings of the JSME international conference on motion and power transmissions 2017*, pages 11–03, 2017.

[60] Lixin Zhang and JW Zu. Modal analysis of serpentine belt drive systems. *Journal of Sound and Vibration*, 222(2):259–279, 1999.

[61] Serge Abrate. Vibrations of belts and belt drives. *Mechanism and machine theory*, 27(6):645–659, 1992.

[62] Lixin Zhang. *Dynamic analysis of viscoelastic serpentine belt drive systems*. PhD thesis, National Library of Canada= Bibliothèque nationale du Canada, 2000.

[63] RGS Gasper and LE Hawker. Resonance frequency prediction of automotive serpentine belt drive systems by computer modeling. In *Proc. ASME Conf. Mechanical Vibration and Noise*, pages 18–2, 1989.

[64] Larry Edward Hawker. *A vibration analysis of automotive serpentine accessory drive systems.* PhD thesis, 1991.

[65] Clark R Barker, Larry R Oliver, and William F Breig. Dynamic analysis of belt drive tension forces during rapid engine acceleration. Technical report, SAE Technical Paper, 1991.

[66] RS Beikmann, NC Perkins, and AG Ulsoy. Equilibrium analysis of automotive serpentine belt drive systems under steady operating conditions. In *Proceedings of the ASME Midwestern Mechanics Conference*, pages 6–8, 1991.

[67] S-J Hwang, NC Perkins, AG Ulsoy, and RJ Meckstroth. Rotational response and slip prediction of serpentine belt drive systems. *Journal of Vibration and Acoustics*, 116(1):71–78, 1994.

[68] MJ Leamy and NC Perkins. Nonlinear periodic response of engine accessory drives with dry friction tensioners. *Journal of Vibration and Acoustics*, 120(4):909–916, 1998.

[69] AG Ulsoy, JE Whitesell, and MD Hooven. Design of belt-tensioner systems for dynamic stability. *Journal of vibration, acoustics, stress, and reliability in design*, 107(3):282–290, 1985.

[70] Wen-Bin Shangguan and Xiang-Kun Zeng. Modeling and validation of rotational vibration responses for accessory drive system. part ii: Simulations and analyses. *Journal of Vibration and Acoustics*, 135(3):031003, 2013.

[71] Xiao Feng, Wen-Bin Shangguan, Jianxiang Deng, Xingjian Jing, and Waizuddin Ahmed. Modelling of the rotational vibrations of the engine front end accessory drive system: a generic method. *Proceedings of the Institution of Mechanical Engineers, Part D: Journal of Automobile Engineering*, page 0954407016685966, 2017.

[72] R Skutch. Uber die bewegungeines gespannten fadens (on the motion of a tensioned string). *Ann. Phys. Chem*, 61:190–195, 1897.

[73] FR Archibald and AG Emslie. The vibration of a string having a uniform motion along its length. *ASME Journal of Applied Mechanics*, 25(3):347–348, 1958.

[74] RA Sack. Transverse oscillations in travelling strings. *British Journal of Applied Physics*, 5(6):224, 1954.

[75] JA Wicker and CD Mote Jr. Current research on the vibration and stability of axially-moving materials. *The Shock and Vibration Digest*, 20(5):3–13, 1988.

[76] JA Wickert and CD Mote Jr. On the energetics of axially moving continua. *The Journal of the Acoustical Society of America*, 85(3):1365–1368, 1989.

[77] JA Wickert and CD Mote Jr. Classical vibration analysis of axially moving continua. *ASME J. Appl. Mech*, 57(3):738–744, 1990.

[78] RS Beikmann, NC Perkins, and AG Ulsoy. Free vibration of serpentine belt drive systems. *Journal of Vibration and Acoustics*, 118(3):406–413, 1996.

[79] RS Beikmann, Noel C Perkins, and AG Ulsoy. Nonlinear coupled vibration response of serpentine belt drive systems. *Journal of Vibration and Acoustics*, 118(4):567–574, 1996.

[80] Lixin Zhang, Jean W Zu, and Zhichao Hou. Complex modal analysis of non-self-adjoint hybrid serpentine belt drive systems. *Journal of Vibration and Acoustics*, 123(2):150–156, 2001.

[81] CD Mote. On the nonlinear oscillation of an axially moving string. *Journal of Applied Mechanics*, 33(2):463–464, 1966.

[82] CD Mote. Parametric excitation of an axially moving string. *J. Appl. Mech*, 35(1):171–172, 1968.

[83] JA Wickert and CD Mote Jr. Linear transverse vibration of an axially moving string–particle system. *The Journal of the Acoustical Society of America*, 84(3):963–969, 1988.

[84] JA Wickert and CD Mote. Response and discretization methods for axially moving materials. *Appl. Mech. Rev*, 44(11):279–284, 1991.

[85] JA Wickert and CD Mote. Travelling load response of an axially moving string. *Journal of Sound and Vibration*, 149(2):267–284, 1991.

[86] L Kong and R Gt Parker. Equilibrium and belt-pulley vibration coupling in serpentine belt drives. *Journal of Applied Mechanics*, 70(5):739–750, 2003.

[87] Lingyuan Kong and Robert G Parker. Coupled belt-pulley vibration in serpentine drives with belt bending stiffness. In *ASME 2003 International Design Engineering Technical Conferences and Computers and Information in Engineering Conference*, pages 373–383. American Society of Mechanical Engineers, 2003.

[88] Lingyuan Kong and Robert G Parker. Steady mechanics of belt-pulley systems. *Transactions of the ASME-E-Journal of Applied Mechanics*, 72(1):25–34, 2005.

[89] Lingyuan Kong and Robert G Parker. Mechanics of serpentine belt drives with tensioner assemblies and belt bending stiffness. *Journal of Mechanical Design*, 127(5):957–966, 2005.

[90] Michael J Leamy and Tamer M Wasfy. Transient and steady-state dynamic finite element modeling of belt-drives. *Journal of Dynamic Systems, Measurement, and Control*, 124(4):575–581, 2002.

[91] Michael Leamy. Dynamics analysis of the time-varying operation of belt-drives. In *ASME 2003 International Design Engineering Technical Conferences and Computers and Information in Engineering Conference*, pages 399–408. American Society of Mechanical Engineers, 2003.

[92] Yoshio Hashimoto. Finite element vibration analysis of axially moving belt. *Nippon Kikai Gakkai Ronbunshu C Hen(Transactions of the Japan Society of Mechanical Engineers Part C)(Japan)*, 19(3):655–660, 2007.

[93] Nicola Amati, Andrea Tonoli, and E Zenerino. Dinamica flessionale di sistemi continui traslanti: modellazione agli elementi finiti. *XXXIV Convegno Nazionale AIAS, Milano Settembre*, pages 14–17, 2005.

[94] Y Lin, T DePauw, and Y Jiang. Analysis of the dynamic effects of an elastic belt in a general mechanical system. In *Proceedings of the 12th European ADAMS User's Conference, Marburg, Germany, November*, pages 18–19, 1997.

[95] Gregor Čepon and Miha Boltežar. Dynamics of a belt-drive system using a linear complementarity problem for the belt–pulley contact description. *Journal of Sound and Vibration*, 319(3-5):1019–1035, 2009.

[96] Gregor Čepon, Lionel Manin, and Miha Boltežar. Introduction of damping into the flexible multibody belt-drive model: A numerical and experimental investigation. *Journal of Sound and Vibration*, 324(1-2):283–296, 2009.

[97] Gregor Čepon, Lionel Manin, and Miha Boltežar. Experimental identification of the contact parameters between a v-ribbed belt and a pulley. *Mechanism and Machine Theory*, 45(10):1424–1433, 2010.

[98] Gregor Cepon, Lionel Manin, and Miha Boltezar. Validation of a flexible multibody belt-drive model. *Strojni\v ski vestnik-Journal of Mechanical Engineering*, 57:539–546, 2011.

[99] Giancarlo Genta. *Vibration of structures and machines: practical aspects*. Springer Science & Business Media, 2012.

[100] Maria di Napoli, Manuel Strähle, Sanjarbek Ruzimov, LD Suarez Cabrera, Nicola Amati, and Andrea Tonoli. Intelligent belt drive systems in hybrid powertrains: a multipurpose test rig. *IFAC-PapersOnLine*, 49(21):47–53, 2016.

[101] G Genta and L Morello. The automotive chassis: Volume 2: System design (mechanical engineering series). 2009.

Appendix A

Test Rig Structural Analysis

Modal Analysis

By means of the software Solidworks Simulation, that uses the displacement formulation of the finite element method, the modal analysis is performed and the vibrational behaviour of the frame was evaluated according to the following steps:

- Modal analysis of the sole frame, comparing three different layouts in order to select the best one.
- Modal analysis of the selected frame together with the loads applied by the electric motors.

Table A.1 Natural frequencies of the first frame, characterized by diagonal beams.Different dimensions of the shell elements

element size $[mm]$	15	25	40
f1 $[Hz]$	48	55	80
f2 $[Hz]$	117	122	131
f3 $[Hz]$	306	308	310
f4 $[Hz]$	422	430	454

The proposed structural solutions were all in Fe420 stainless steel, which has medium tensile strength, good ductility and relatively low cost. The difference between the three frames stands on the intermediate elements between the vertical and

Table A.2 Natural frequencies of the second frame, characterized by side diagonal beams and reinforcing triangular ribs on the corners of adjacent horizontal beams, top and bottom planes. Different dimensions of the shell elements

element size $[mm]$	15	25	40
f1 $[Hz]$	128	135	151
f2 $[Hz]$	149	154	165
f3 $[Hz]$	308	310	311
f4 $[Hz]$	426	435	454

Table A.3 Natural frequencies of the third frame, characterized by reinforcing triangular ribs on the corners of adjacent horizontal beams, top and bottom planes and on the side planes, at the intersection of the horizontal beams with the vertical beams. Different dimensions of the shell elements

element size $[mm]$	15	25	40
f1 $[Hz]$	139	144	155
f2 $[Hz]$	146	151	166
f3 $[Hz]$	295	307	324
f4 $[Hz]$	295	307	326

the horizontal beams. The first frame has side diagonal beams. The second one has also side diagonal beams and reinforcing triangular ribs on the corners of adjacent horizontal beams, top and bottom planes. The third solution features reinforcing triangular ribs on the corners of adjacent horizontal beams, top and bottom planes but also on the side planes, at the intersection of the horizontal beams with the vertical beams. A modal analysis was performed in order to evaluate the proposed frame stiffness. Different dimensions of the shell elements were considered in order to evaluate the influence of the mesh size on the FEM analysis. Tables A.1, A.2, A.3 provide the results obtained for the three frames and show a comparison between the calculations performed considering different shell element sizes. Fig. A.1 shows the results of the calculation for the third frame that resulted as the stiffest one and was therefore chosen for the test rig design. The second step of the modal analysis consisted in taking into account the vibrational behaviour of the chosen frame when the electric motor loads are applied. An horizontal plate was designed and mounted on the frame where the two electrical motors housings and the other drive accessories can be fixed. The plate thus has a squared shape of the same dimensions of the frame. A second thinner plate is mounted on the lower crossbeams of the frame. This plate

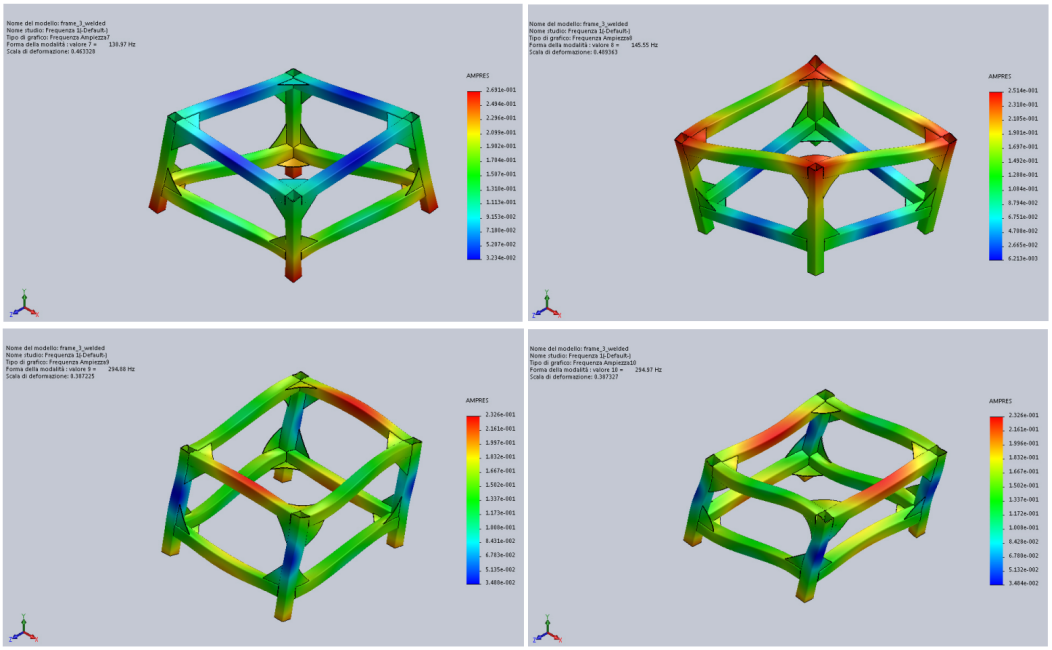

Fig. A.1 Modal analysis of the chosen test rig frame. The frame features reinforcing triangular ribs on the corners of adjacent horizontal beams, top and bottom planes and on the side planes, at the intersection of the horizontal beams with the vertical beams.

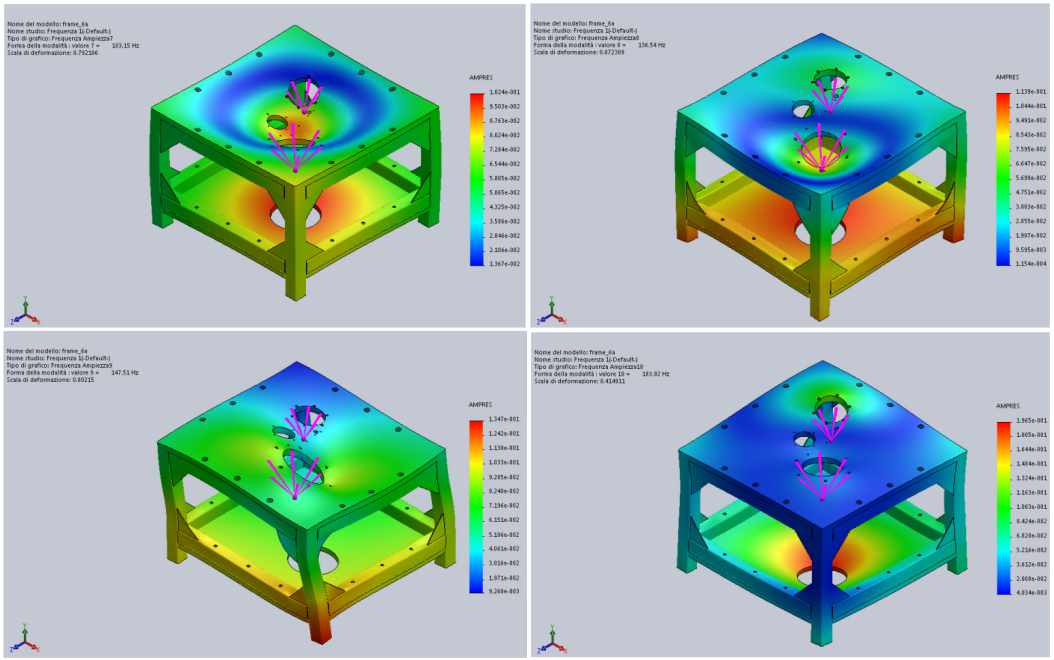

Fig. A.2 Modal analysis of the test rig frame with upper and lower plates and the electric motor loads applied to the relative centre of mass

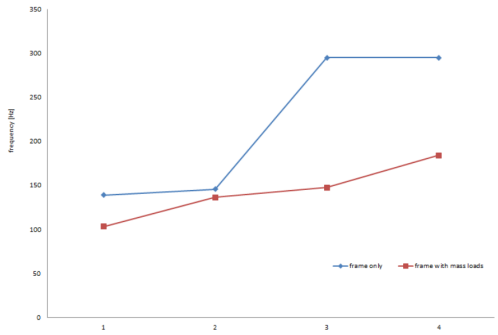

Fig. A.3 Comparison beween the natural frequencies of the chosen frame with and without the electric motos mass loads and upper and lower plates.

Table A.4 Natural frequencies of the chosen test rig frame with the applied loads

f1 $[Hz]$	103
f2 $[Hz]$	136
f3 $[Hz]$	147
f4 $[Hz]$	184

is aimed at increasing the stiffness of the overall structure and at providing, at the same time, a support base for the cooling system accessories. The plate has also two holes allowing the passage of the electrical cables and cooling pipes of the two electrical machines. Both the plates are made of aluminum alloy.

The load values corresponding to the two electric motors were applied to the relative centre of mass, simulating the weight of the electrical motor subsystems and an additional modal analysis was performed. The results for the four natural frequencies are listed in Table A.4 and are shown in Fig. A.2.

In Fig. A.3 the natural frequencies of the frame with the mass loads are compared with the natural frequencies of the only frame, without the two plates and the weight of the electrical machines and their housings. It is reasonable that due to the increasing of the overall mass the expected values of the natural frequencies are lower. In fact, from the mathematical analysis:

$$\omega_0 = \sqrt{\frac{k}{m}} \tag{A.1}$$

where ω_0- natural frequency, k- stiffness, m- mass.